Next-generation active telescope for space astronomy

Stefan Martin,[a] Charles Lawrence,[a,*] David Redding,[a] Bertrand Mennesson,[a] Michael Rodgers,[b] Kevin Hurd,[a] Rhonda Morgan,[a] Renyu Hu,[a] John Steeves,[a] Jeffrey Jewell,[a] Charles Phillips,[a] Claudia Pineda,[a] Ned Ferraro,[a] and Thibault Flinois[a]

[a]Jet Propulsion Laboratory, California Institute of Technology, Pasadena, California, United States

[b]Synopsys, Inc., Pasadena, California, United States

Abstract We present a design for an active telescope for space astronomy. The telescope is capable of both exoplanet work and general astronomy over wavelengths from ~100 nm up to 5 μm. The primary mirror is 6 m in diameter, formed by 16 mirror segments that are precisely phased and supported on rigid body actuators and with segment optical surface figures fine-tuned using surface figure actuators. The active primary forms a large deformable mirror (DM) with wavefront error (WFE) correction at the entrance pupil. Thus the largest source of WFE can be removed at the source and is corrected over the entire field of view. This enables diffraction-limited performance at 400 nm and a more efficient optical system over a broader wavelength range than could be achieved by a small DM at a downstream relayed pupil. The telescope is passively cooled to below 100 K at Sun–Earth L2, enabling astronomical-background-limited observations out to 5 μm. Launched on a SpaceX Starship or alternatively National Aeronautics and Space Administration's Space Launch System, the telescope requires minimal deployments. A 72-m-diameter starshade provides a contrast ratio better than 10^{-10} for exoplanet science. Near the visible region, with a 108% working bandwidth from 300 to 1000 nm, a working distance of 120 Mm provides a 51-mas inner working angle (IWA). This band can be moved to shorter or longer wavelengths by adjusting the starshade range from the telescope. Our first-ever thermal analysis of such a starshade shows that a temperature below 100 K can be achieved over a broad range of observing directions, permitting the possibility of working into the infrared. We model the yield in exoplanets that can be observed. A starshade and associated spectrograph offer significant advantages for exoplanet characterization. They enable a much broader instantaneous spectral bandwidth (here 108%) than current coronagraphs (~10% to 20% bandwidth), allow both polarizations to be observed simultaneously, and have higher throughput. The IWA is twice as small as can be achieved with a coronagraph and there is no outer working angle. These differences are particularly pronounced in the UV, where coronagraph performance would be strongly affected by throughput losses, wavefront aberrations, Fresnel polarization effects at surfaces, and thermal instability. [DOI: 10.1117/1.JATIS.8.4.044005]

Keywords: telescopes; exoplanets; starshades; coronagraphs; Habitable Exoplanet Observatory; Large UV Optical Infrared Surveyor; Origins.

Paper 22006G received Jan. 19, 2022; accepted for publication Oct. 7, 2022; published online Dec. 8, 2022.

1 Introduction

Breakthroughs in our knowledge of the Universe often depend on technological advances. Observations across the electromagnetic spectrum, enabled by access to space along with new telescopes and detectors, make the Universe of today much richer and more interesting than the Universe of 1950. We learn different things from different parts of the spectrum and from non-electromagnetic sources as well.

*Address all correspondence to Charles Lawrence, charles.lawrence@jpl.nasa.gov

At present, we know of life on only one planet, Earth. More than 4000 exoplanets have been identified,[1] with many more on the way, and much work is devoted to figuring out how to determine if life exists on any of them. Spectroscopic observations of starlight reflected from, thermally emitted from, or transmitted through their atmospheres are the only means we have. What wavelengths should we observe? What hardware is required for those difficult observations?

In this paper, we describe a concept design for a mission, the active telescope for space astronomy (ATSA), whose primary goal is spectroscopy of exoplanets, with particular emphasis on Earth-like planets and the possible detection of signatures of life. It has a 6-m, segmented, 100-K telescope with a starshade that could launch on rockets now being built and could take direct spectra of exoplanets, including Earth-like ones, from 0.2 to 5 μm. Section 2 discusses the science drivers for the flight system. Section 3 describes the flight system in detail. Section 4 describes the starshade, including its thermal performance. Section 5 describes the telescope. Section 6 describes the instruments. Section 7 describes technology developments necessary for ATSA. Section 8 models the yield of Earth-like and other exoplanets expected from the mission. Section 9 summarizes the characteristics of the flight system and mission. Section 10 gives conclusions.

2 Science Drivers

The key science and architecture driver for ATSA is the spectral characterization of true Earth analogs—defined as Earth-size exoplanets orbiting in the habitable zone (HZ) of Sun-like (FGK) stars—over a broad enough wavelength range that the planet habitability and potential for hosting life can be assessed. The large ground-based observatories under construction (the European Extremely Large Telescope and the Giant Magellan Telescope) or planned (the Thirty Meter Telescope) will have great light-collecting power and powerful new instruments, but the Earth's atmosphere, even with adaptive optics, will limit their ability to suppress starlight to well below the 10 orders of magnitude necessary to observe an Earth-like planet around a Sun-like star in reflected light. These ground-based giants will have an important role in the study of exoplanets, but only from space will it be possible to take UV/visible/IR spectra of Earth-like planets around Sun-like stars, as proposed in the recent Habitable Exoplanet Observatory (HabEx)[2] and Large UV Optical Infrared Surveyor (LUVOIR)[3] mission concept studies and as recommended by the Astro2020 decadal survey.[4]

Although exoplanet science is driving the ATSA architecture and is the reason for its most demanding requirements, the telescope will be spectacularly well-equipped for general astrophysics (GA), as was thoroughly discussed in the HabEx and LUVOIR reports cited above. These reports discuss a large range of key GA science, and the program for ATSA would be along the same lines. The great scientific importance and richness of the 1.5- to 5-μm region of the spectrum is now on full display with images, spectra, and hundreds of papers from NIRCam, NIRSpec, and NIRISS on the James Webb Space Telescope after only a few months of observations.

In the HabEx and LUVOIR concepts, exoplanet characterization is essentially based on direct high-contrast imaging and spectroscopy. Both mission concepts aim to achieve 10^{-10} contrast ratios (contrast ratio is the ratio of starlight irradiance in an arbitrary resolution element of the focal plane to the irradiance that would be seen in that same resolution element were the star to be centered there) with internal coronagraphs; HabEx achieves that contrast ratio with an external starshade as well. HabEx examined an off-axis, 4-m monolithic primary and several variants, whereas LUVOIR examined 15- and 8-m segmented primaries (120 or 55 segments). The direct imaging and spectroscopy instruments covered similar spectral bands for the two mission concepts: from 200 nm (diffraction-limited at 400 nm) to 1.8 μm. This wavelength range was chosen to cover key molecular absorption features indicative of habitability and potentially life: the O_3 cut-off short of 330 nm, the O_2 A band centered around 760 nm, and multiple water bands centered at 720, 820, 940, 1130, and 1410 nm. The 1.8-μm upper limit is set by the telescope operating temperature of ~270 K. Indeed, for direct spectroscopy of exoplanets, including and especially exo-Earths, bright starlight is suppressed by more than 10 orders of magnitude by a

starshade or a coronagraph and the thermal background from a ~270-K telescope (see Fig. 5) becomes prohibitive above 1.8 μm.

Access to wavelengths between 1.8 and 5 μm would greatly enhance the characterization of super-Earths or true exo-Earths in multiple ways. When searching for habitability indicators and assessing potential biosignatures in the atmosphere of a rocky planet, the most important gases to look for are O_2, O_3, CH_4, H_2O, CO_2, and N_2O. Figure 1 indicates the molecular opacities of these six gases from 0.3 to 20 μm and clearly illustrates the wealth of spectral information available when extending observations from the near UV/visible domain considered in HabEx and LUVOIR further into the infrared, where broader and stronger spectral features can be seen.

More specifically, improving the detectability of CH_4 in the atmosphere of exo-Earths in which oxygen is also detected is critical, as the simultaneous detection of oxygen and a reduced gas, such as CH_4, can be considered as a signature of biological activity. Both oxygen and methane are important in searching for life and confirming the biotic origin of any key features detected.[7] Notably, the CH_4 features at 2.3 and 3.3 μm are far easier to detect in the Earth's atmosphere than the 1.6-μm methane feature.

Likewise, measuring the abundance of CO_2—a signpost of a bona fide rocky planet—via its strong features at 2.3, 2.7, and 4.3 μm in the atmosphere of Earth-sized exoplanets is important in establishing the context for interpreting biosignature gas detections. For example, for planets with detected oxygen, it would allow one to identify or rule out the abiotic production of oxygen via photochemical dissociation of CO_2. Such mechanisms have been invoked for rocky planets orbiting M stars and would produce CO_2 concentrations orders of magnitude greater than modern-day Earth.[8,9]

Even in the case of an Archean-like biosphere driven by methane-producing chemosynthesizers, any atmospheric CH_4 detected must be distinguished from nonbiological CH_4, such as seen on Titan. The ability to detect low CO_2 concentrations is again key, because high Archean-like CH_4 concentrations are not sustainable in CO_2-rich atmospheres unless there are massive amounts of CH_4 consistent with biological production.[10,11]

The relative feature depths at different wavelengths for Earth-like CO_2 and CH_4 concentrations promise a significant improvement in column density detection limits with observations longward of 1.8 μm. This is clearly seen in the simulated 0.3- to 5-μm spectrum of an exo-Earth

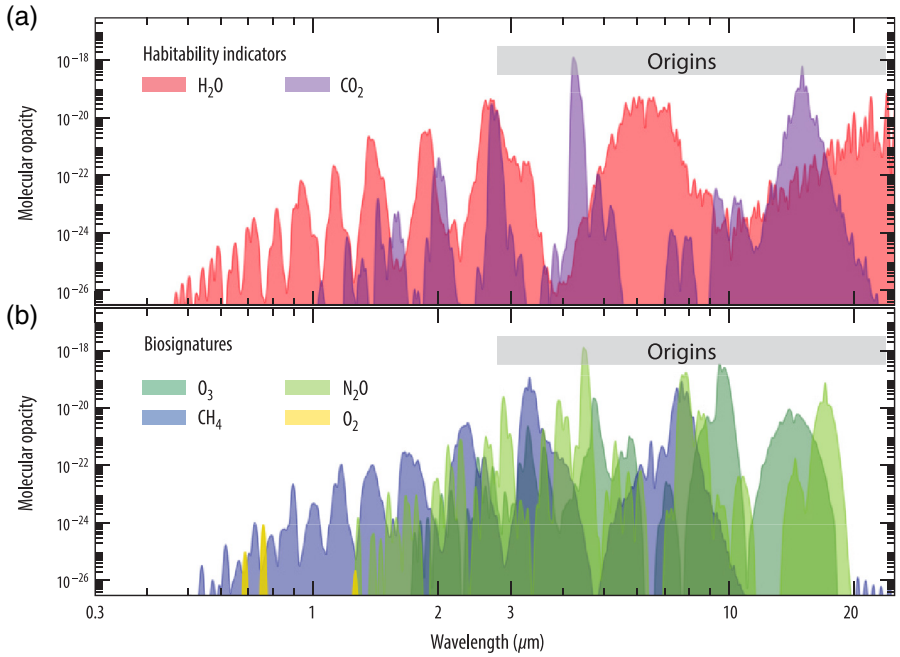

Fig. 1 Molecular opacities of relevant habitability (a) indicator and (b) biosignature gases in the MIR. Origins is sensitive to multiple bands for each molecular species, which is critical in breaking degeneracies between overlapping spectral signatures (adopted with permission from Ref. 6).

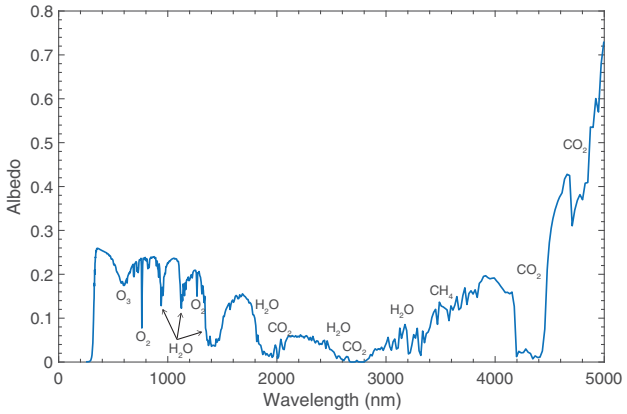

Fig. 2 Model spectrum of a terrestrial exoplanet 1 AU from a Sun-like star, with an Earth-like atmospheric composition. The spectrum was simulated by a general-purpose atmospheric radiative-transfer model[12] and is a combination of the surface patches without clouds and with low and high clouds (required to fit Earth's spectrum in the visible and near-infrared[13]). The spectrum is normalized to the "apparent albedo," i.e., to a fully reflective planet with no thermal emission at the orbital phase of zero. The simulation adopts the orbital phase of $\pi/3$. The main spectral features are labeled. The brightness of the planet is mainly subdued by the broad absorption bands of H_2O at 2 to 4 μm, but additional absorption from CO_2 and CH_4 can be seen. CO_2 features are prominent at 4 to 5 μm where thermal emission boosts the apparent albedo.

twin (Fig. 2), revealing the presence of CO_2 and CH_4 at longer infrared wavelengths and showing a sharp increase in apparent albedo above 4 μm due to thermal emission.

In addition, many proposed biosignature gases beyond O_2 and CH_4 have spectral features in the 1.8- to 5-μm range, e.g., CH_3Cl at 3.3 μm, $(CH_3)_2S$ (dimethyl sulphide or "DMS") at 3.1 to 3.6 μm, N_2O at 4.5 μm, NH_3 at 3.0 μm and PH_3 at 2.7 to 3.6 μm.[14–17]

As noted by other authors (e.g., Ref. 18) extending the wavelength range up to 5 μm is also very beneficial for spectroscopic studies of transiting exoplanets, especially for exo-Earth observations, where essential information about the chemical content of the atmosphere is contained in the spectrum longward of $\sim$1.5 μm. As an example, Fig. 3 shows a model transit spectrum of GJ1132b (a super Earth orbiting a nearby M star) based on Hubble data, showing water, methane, and ammonia features, plus two model curves showing the effect of hazes and aerosols. In the case of transit spectroscopy, primary transits measure the variable transmission of the planet upper atmosphere versus wavelength, whereas secondary transits directly detect the exoplanet emission spectrum. Because the probability for a planet to transit is inversely proportional to its distance from the star and because the transit signal amplitude increases as the ratio of the planet to star radii squared, transit spectroscopy is particularly sensitive to short-orbit planets transiting M stars.

We show in subsequent sections how ATSA satisfies the science requirement for direct and transit spectroscopy of exoplanets, especially exo-Earths, over a broad range of wavelengths from the near ultraviolet to 5 μm, strongly improving the detectability of biosignature gases in the atmosphere over what can be achieved with narrower spectral coverage. Section 8 describes our design reference mission (DRM) and science yield simulations in detail. Figure 4 summarizes the main results. ATSA enables the characterization of many exoplanets, including exo-Earths, over a broader range of wavelengths than those accessible to the HabEx and LUVOIR mission concepts. In the case of perfect prior knowledge of all exo-Earths around nearby stars of spectral types F, G, and K and their orbital parameters, we estimate that over the course of a 5-year mission, 32 exo-Earths can be spectrally characterized over the full 0.3- to 1-μm range [Fig. 4(a)] and seven can be characterized all the way to 2.4 μm [Fig. 4(b)]. This increased spectral range provides access to a stronger CH_4 absorption feature at 2.32 μm and, more importantly, to CO_2 features at 2.03 and 2.29 μm. Three of these exo-Earths can even be spectrally characterized all the way to 3.4 μm, giving access to a deeper and broader CH_4 feature at 3.3 μm and one more CO_2 feature at 2.7 μm.

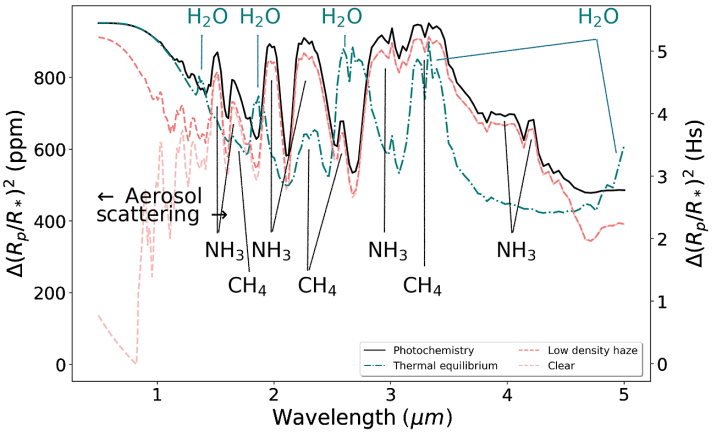

Fig. 3 Transit spectrum (black) of super Earth GJ1132b from 0.3 to 5 μm, based on modeling data taken with Hubble (Roudier, private communication). The two dashed curves show models of how the spectrum would change if there were low-density haze (red curve) or no haze at all in the atmosphere (pink curve). The effects of hazes are most pronounced at wavelengths shorter than $\sim$1.5 μm). The green dashed-dot spectrum shows the effect that changing gas content without changing cloud and aerosol structure would have on the spectrum. Gas is now dominated by water vapor as in an atmosphere in pure thermal equilibrium. This effect is most prominent at the long wavelengths: essential information about the chemical content of the atmosphere is contained in the spectrum longward of $\sim$1.5 μm.

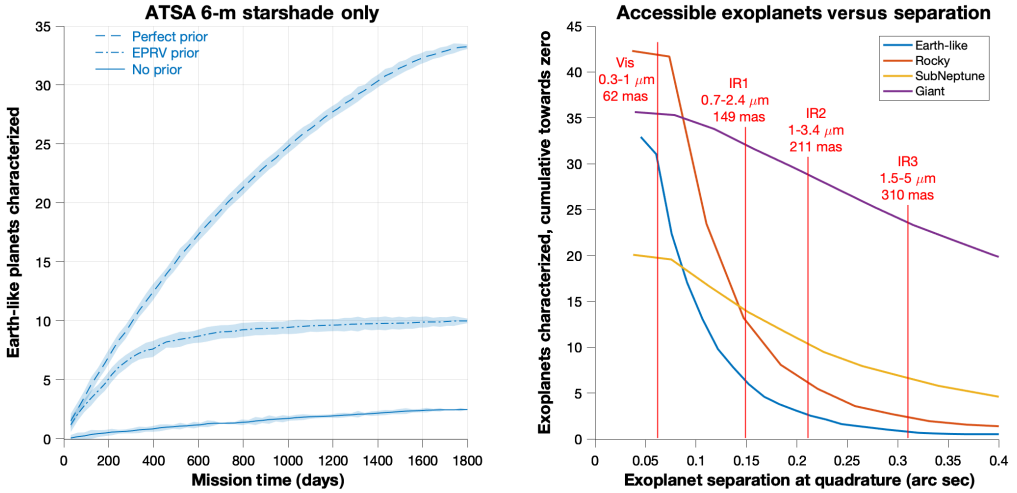

Fig. 4 (a) Cumulative number of exo-Earths spectrally characterized over the 5-year mission time by the ATSA telescope and starshade between 0.3 and 1 μm. Cumulative yield versus time is plotted for three assumed levels of precursor knowledge: no prior knowledge, requiring a blind-search survey (bottom curve); partial prior knowledge via ground-based, 3 cm s^{-1} EPRV (middle curve); and perfect prior knowledge (top curve), which shows an upper bound due to starshade transition scheduling and exhaustion of available targets. The shaded regions indicate the 1σ standard deviation. (b) Cumulative number of spectrally characterized exoplanets (assuming perfect prior knowledge of exo-Earths and observed concurrently with exo-Earths) having an apparent separation at quadrature (orbit semimajor axis) larger than a given separation (x axis). Planet yields are indicated for four planet types: Earth-like planets (blue curve), which form a subset of all rocky planets characterized (red curve), sub-Neptunes (yellow curve), and giant planets, i.e, with radii greater than 3.5$\times$ Earth radius (purple curve). Vertical lines indicate the starshade IWAs accessible for different wavelength ranges, including three infrared bands IR1, IR2, and IR3. For instance, of 33 exo-Earths that are spectrally characterized between 0.3 and 1 μm, around six can be characterized up to 2.4 μm (the intersection of IR1 line and blue curve).

In the case of perfect prior knowledge, there are about as many gas giant planets as exo-Earths spectrally characterized from 0.3 to 1 μm during exo-Earth observations. More than 20 of the more distant giant planets can be measured spectroscopically all the way to 5 μm.

3 ATSA: Active Telescope for Space Astrophysics

As discussed above, extending wavelength coverage to 5 μm would have clear scientific advantages for exoplanet spectral characterization, as well as providing background-limited GA capabilities through the mid-infrared (MIR). It also has two important consequences for the flight system: (i) the telescope must be maintained at a low enough temperature to keep its own thermal background radiation well below the astronomical background. (ii) The starlight suppression system must provide a small enough inner working angle (IWA) (the smallest separation accessible at high contrast) that exoplanets can still be detected directly in the infrared, which calls for a starshade system. Moreover, a starshade system is absolutely preferred for high-contrast observations at UV wavelengths, where increased polarization-induced aberrations, surface figure errors (SFEs), thermal instability, and low throughput issues strongly disfavor coronagraphs. These performance advantages strongly favor starshades over coronagraphs. Coronagraphs, on the other hand, have operational advantages over starshades. In terms of complexity, a coronagraph does not require a second spacecraft to carry the occulter. In terms of agility, a coronagraph is more nimble. Nevertheless, settling times of 50 h or more[2] are needed to achieve thermal stability sufficient for coronagraphy—a significant retargeting overhead. Obviously, to gain both kinds of advantage, a large exoplanet mission should have both a starshade and a coronagraph. In this study for an active telescope for space astrophysics or ATSA, we include only a starshade, for three reasons. First, considerable work on coronagraphs is already in progress by other groups (see Sec. 6.6) and does not need to be duplicated here. Second, implementing a coronagraph on a segmented, on-axis aperture is difficult, as outlined in that section. Third, the thermal aspects of starshades have received no prior attention, yet are critically important for a cold telescope covering out to 5 μm. This is worth exploring; we take that up in Sec. 4.

The sky from space is dark, with observational limits set by the astronomical background. To reach those limits, thermal emission from the telescope optics must be kept below the level of the astronomical background. At short wavelengths, this is easily achieved at room temperature. At longer wavelengths, however, telescopes must be cooled, as shown in Fig. 5. At 290 K, thermal emission from telescope optics starts to dominate the background at about 1.5 μm. The exact wavelength depends on the emissivity of the telescope, but weakly, since telescope thermal emission is from the Wien side of the blackbody curve, increasing exponentially with temperature, completely dominating the linear change with emissivity. Figure 5 shows that in order to be astronomical-background-limited at 5 μm, a telescope must be cooled to $\leq$100 K.

Cooling to $\leq$100 K has been done many times. Herschel, the largest astronomical telescope yet flown for wavelengths shorter than 1 cm, was passively cooled at L_2 to below 100 K, but because it observed at wavelengths from 60 to 625 μm, it was far from astronomical background limited. James Webb Space Telescope (JWST) is cooled passively—at the time of writing it is at 42 K—and is background-limited out to 12 μm or so. However, for characterizing exo-Earths, spectra extending from the near-ultraviolet to the MIR are needed and the shorter wavelengths require an order of magnitude lower wavefront error (WFE) than JWST will achieve. Building JWST was a challenge. Building it the same way to achieve an order of magnitude smaller WFEs would be a much bigger challenge.

The solution that we advocate is to build a fully active telescope. In a fully active telescope, the surface of the primary mirror (PM) is controlled. Measurements of the wavefront allow corrections to be determined and applied. Actuators correct and control the shape of the PM from mechanical levels ($\lesssim$1 mm, in the case of a segmented primary) to optical levels ($\lesssim$10 nm). In effect, all the components of the telescope are assembled on the ground, but the operating optical system is finally configured and maintained in space, in 0 g, at temperature.

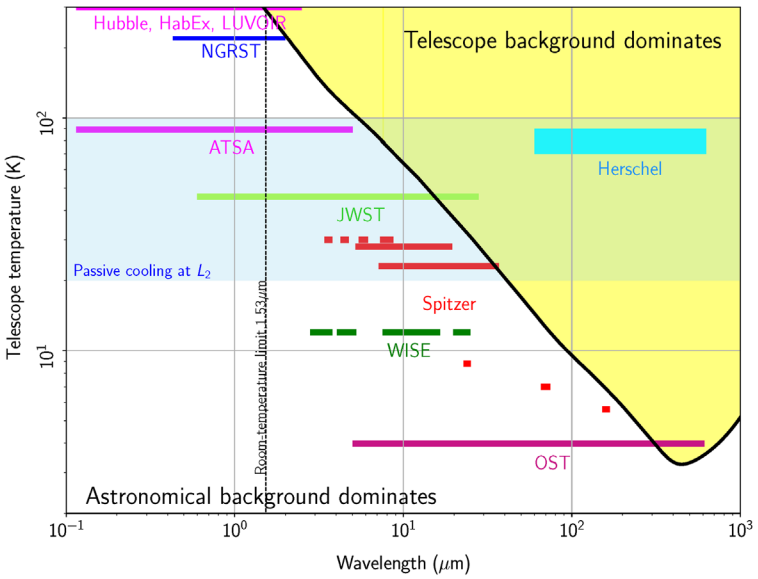

Fig. 5 Telescope temperature required as a function of wavelength to keep thermal emission from the telescope itself to less than 10% of the astronomical background. Average values of total telescope emissivity are assumed. The colored bars show the wavelength ranges observed by a number of telescopes, past, present, and future. Although a major advance for its time, Herschel was completely dominated by telescope background. Background data adopted with permission from Ref. 5 and Bradford (private communication).

This study, ATSA, builds upon the HabEx, LUVOIR, and Origins Space Telescope (OST) studies but with some important differences. First, background-limited wavelength coverage to 5 μm is enabled by letting the telescope cool passively to 100 K, significantly cooler than LUVOIR and HabEx but warmer than OST. Second, the telescope is fully active, meaning that the PM surface and total wavefront can be measured and adjusted over a sufficient range to correct for distortions caused by ground → space changes in effective gravity and temperature, providing greater allowable tolerances in fabrication and other external factors.

Although we anticipate substantially increased science return and possible cost benefits to this approach, a fuller analysis than was possible for this study should be performed. In this paper, we show how these two major differences can be implemented and answer the following questions raised by the departure from conventional warm, static, or semiactive telescope designs.

(1) What are the advantages of an active PM?
(2) What aperture can be fit without deployment into existing or planned launch vehicle shrouds?
(3) How can one observatory provide background-limited observing capability from UV to MIR?
(4) What exoplanet science would be enabled by high-contrast imaging across the spectrum from the near-UV to the mid-IR?
(5) What instrumentation could be provided?
(6) What technology developments are needed?

Figure 6 compares the collecting area and spectral coverage of LUVOIR A and B, HabEx 4.0, and ATSA. The HabEx study considered nine different architectures (three configurations—starshade only, coronagraph only, and both together—each in three aperture sizes), included apertures down to 2.4 m and also a segmented architecture. After the baseline HabEx 4.0H design, the most-studied was an on-axis 3.2-m telescope (HabEx 3.2S) with six pie-slice segments. A scaled-up version of HabEx 3.2S can form the basis of a 6-m segmented telescope. (The HabEx study considered a 6-m monolith for space to be infeasible at that time.)

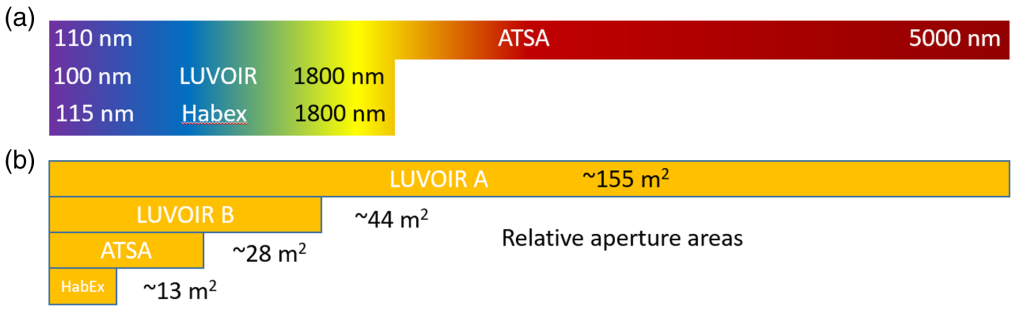

Fig. 6 (a) Regions of the spectrum covered at the astronomical background limit by ATSA, HabEx, and LUVOIR. (Note that both HabEx and LUVOIR can observe brighter objects beyond 1800 nm.) (b) Relative aperture areas: OST has a similar aperture size to ATSA.

Furthermore, segmented designs undoubtedly point the way forward for the largest space apertures and, coupled with in-orbit assembly, will rival the apertures currently being built on the ground.[19,20]

A front view of the ATSA telescope is shown in Fig. 7. Like the OST,[6] it is an on-axis telescope of 6-m aperture, with a segmented (but not deployed) PM (M1) comprising an outer ring of 12 segments and an inner ring of six segments, with the secondary mirror (SM, M2) supported by three struts aligned with segment gaps. In contrast to OST, it uses a smaller sunshield that is more conformal to the scarfed cylindrical outer barrel. Its thermal control system (TCS) is completely passive. The angled scarf provides a field of regard (FOR) ranging more than 280 deg, from anti-Sun to within 40 deg of the Sun. Solar panels cover the spine of the barrel and also the base.

The advantages of off-axis telescopes are clear, namely higher throughput, lower diffraction losses and, for coronagraphs, lack of obstructions that place large gradients on the wavefront. There are disadvantages also, as the width of the telescope structure must be wider than the aperture by at least the diameter of the secondary mirror. These factors increase overall size and weight and reduce stiffness for the same aperture diameter and, if constrained by the interior diameter of the rocket shroud, will reduce the feasible aperture. The ATSA design that we present in this paper (advanced from Ref. 21) is on-axis. An off-axis version with the same PM size will be presented in a future paper.

(a)

Sunshade wing and spine design

Root hinges and wings

- Minimize thermal conduction:
  - Detached thermal load-path at roots and wing tips
  - Stowed hinge interfaces convert upon deployment into point or line contacts
  - Launch locks are non-conductive after deployment
  - Wing tips tensioned for station keeping stability

Technical requirements:

• Quantity of wings and spine:	5 layers
• Sun angle, roll:	0°±0.5°
• Sun angle from telescope optical axis:	40° to 180°
• Root hinge, deployed gap:	85-mm ±5-mm (80mm min.)
• Wing, deployed angle, minimum:	3.5° ±.5° (3.0° min)

(b)

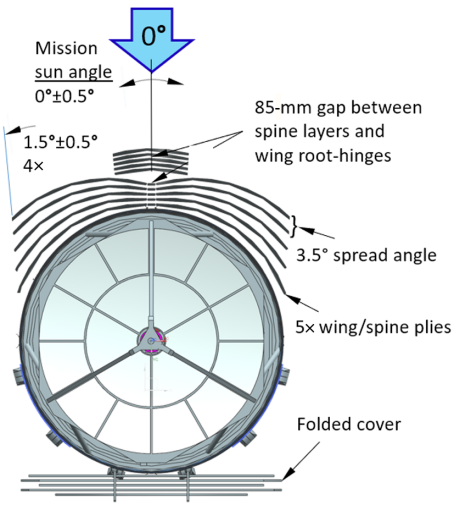

Fig. 7 (a) Sunshield design parameters and (b) view of the telescope looking down the barrel. The folded telescope cover is at the bottom. Sunlight impinges on a symmetric sunshield at the angles shown at the top. The primary mirror is segmented with six central pie-shaped pieces and twelve surrounding pieces, creating a 6-m aperture. The small secondary mirror (562-mm clear aperture) is supported by three struts and has active position control.

ATSA employs segments to achieve an aperture larger than is currently manufacturable as a single piece but (unlike LUVOIR or JWST) does not require folding the aperture to enable packaging into the launch vehicle. After launch, the mirror segments are moved into a precisely phased condition using rigid body actuators (RBAs) and their surface figures are fine-tuned using surface figure actuators (SFAs). The active PM forms a large deformable mirror (DM), with fine active control of the segments enabling observatory WFE correction at the entrance pupil. This removes the largest source of WFE at the source, providing a better-corrected and more efficient optical system over a broader wavelength band and over the entire field of view (FOV) than could be achieved by a small DM at a downstream relayed pupil, as discussed in more detail below.

ATSA extends the wavelength range covered by HabEx and LUVOIR by having a cold optical system. With a PM maintained at or below 100 K (thermal modeling showed the PM temperature of the design to be as low as 89 K), ATSA will be capable of doing astronomical-background-limited science on faint targets through M-band (3 to 5 μm).

3.1 *Cold Telescope*

The mirror temperatures of $\leq$100 K required for astronomical background limited observations out to 5 μm (Fig. 5) can be achieved passively, as demonstrated by Herschel ($\sim$90 K), JWST [42 K at the time of writing), Planck[22] (36 K), Spitzer[23] ($\sim$30 K), and WISE[24] ($\sim$75 K) in their postcryogen phases]. ATSA is designed for passive cooling, taking advantage of the stable thermal environment at Sun–Earth L2 and using a sunshield that covers one side and the bottom of the spacecraft, while allowing the rest of the structure to radiate to cold space. Extending the sunshield beyond the SM on the Sun side forms a "sugar scoop" or scarf. This provides thermal and optical protection for observing angles ranging from anti-Sun to 40 deg from the Sun. On the opposite, shaded side, the shortened barrel exposes much of the PM and barrel interior to cold space, improving thermal radiation. The thermal design challenge is to balance the thermal input from the sunshield and the need to dissipate heat from on-board electronics. Radiators take up cold-exposed area and so low-power use is desirable. The thermal design and predicted performance of ATSA are detailed in Sec. 3.4.

3.1.1 *Active primary mirror*

For telescopes, DMs enable compensation of optical fabrication errors, thermal distortion errors, assembly and misalignment errors, and optical testing errors—each of which has proven to be a problem for past space optical missions. The ATSA active optics approach provides robust control of these effects; to ensure the 30-nm overall WFE requirement can be met, even for a 100-K telescope. From a mission cost point of view, the actuated PM segments reduce or eliminate the need for cryo-null figuring of the PM segments, as segment SFAs will compensate the residual cool-down thermal deformations.

ATSA controls the large PM itself, rather than introduce a small DM at a pupil conjugate to the PM further downstream. The reason for this is that the best location for WFE correction is at source. Since the PM is generally the largest source of WFE in a space telescope, the PM itself is therefore the best location for correction. Indeed, correcting PM-induced WFE further downstream using a DM at a relayed pupil has the deleterious effect of imposing limits on the correctable FOV. The angle of the incoming rays at a smaller pupil is magnified by a factor M, the ratio of the entrance pupil (the PM diameter, usually) to the diameter of the DM.[25] This effect is described by the Lagrange invariant, which relates ray heights and angles within the optical system. For an on-axis field, a wavefront phase correction at a downstream DM requires an axial translation of the DM surface. A ray from an off-axis field point striking the same DM surface position will experience a correction reduced by $\cos(M\theta)$, where θ is the field angle, resulting in a residual phase aberration. Other, even more important effects for real telescope designs are produced by pupil shear and pupil distortion between the entrance pupil and the DM. Pupil shear is a function of field angle and optical surface position relative to a pupil—rays arriving from different field angles strike different parts of the mirrors so that they experience different aberrations across the pupil. Pupil distortion created by the optical system

(a reality for any system with more than zero field) also causes rays to sample different portions of the intervening optical surfaces as a function of field angle. Thus there can be no common position of the DM actuators that can cancel pupil aberrations for all fields.[26] In the case of correction at the PM, the $\cos(M\theta)$ term may be replaced by unity, so that all fields experience the designed ideal optical surface, optimizing the initial wavefront, or the surface may be optimized to produce the least overall aberration downstream, in which case a weak $\cos(\theta)$ effect is introduced. In this latter case, the PM is being used in the same way as an internal DM, to achieve the best correction across a wavelength band.

In ground-based, DM-controlled AO systems, atmospheric turbulence limits the correctable field, so the wide-field advantage of correcting the PM cannot be realized, but for space telescopes operating in a benign environment and with significant fields of view these effects become important. Correction of WF errors at the source rather than at a relayed pupil also avoids the possibility that useful light might be lost at intervening stops or baffles, or further confused by intervening aberrations.

3.1.2 *Telescope aperture size*

For nondeployed apertures, available fairing sizes limit the diameter of circular aperture telescope designs. The largest fairing diameters currently or soon to be available are for the SpaceX Starship System and Space Launch System (SLS).

Starship. The standard fairing has an 8-m internal envelope diameter and 8 m of length to the shoulder. With the proposed +5-m extension, this shoulder is 13 m from the adaptor. By launching to low-Earth orbit and then refueling in a parking orbit, Starship can lift 100 tonne to Mars, so it easily has capacity to bring a telescope to L2. (On energetic grounds, the direct launch of a lighter payload, such as a 20-tonne telescope, to L2 appears possible—but this launch profile has not yet been explored.)

SLS 8.4 m. The 8.4-m fairings have internal envelope diameters of 7.5 m with the "short" concept providing 9.86 m of height measured from the adaptor plane to the shoulder of the fairing. A "long" concept provides 18.18 m between the same points.

SLS 10 m. The 10-m fairings have internal envelope diameters of 9.1 m with the short concept, again providing 9.86 m of height to the shoulder of the fairing. The long concept provides 12.1 m between the same points. These fairings mounted to the Block 1B or Block 2 vehicles provide lift to Earth escape (i.e., $C3 = 0$) of up to 40.2 and 44.3 tonnes, respectively. For injection to Sun-Earth L2, an upper stage [exploration upper stage (EUS)] provides additional ΔV.

These internal fairing diameters, 7.5, 8.0, and 9.1 m, effectively, limit nondeployed aperture diameters to between 6 and 7.6 m, assuming 1.5 m is needed for the telescope barrel, sunshield, and other systems around the observatory itself. Thus a 7.6-m version of ATSA would be possible if the SLS was to be the launch vehicle, yielding 1.6× the aperture area. The telescope would necessarily have a reduced f/D, and a new set of thermal, optical, and mechanical analyses would be required. Alternatively and perhaps more importantly, an off-axis 6-m version of ATSA would fit, once again with new optical and mechanical analyses.

Both the SLS and Starship launch vehicle systems will thus be capable of lifting a 20-tonne telescope to Sun-Earth Lagrangian orbit 2 (SEL2). Details of the fairing shape then dictate the format of the telescope, with the usual cylindrical shape restricted in height by the fairing shoulder when the aperture diameter is maximized.

3.1.3 *Providing observing capability from UV to MIR*

The recent LUVOIR and HabEx designs provide a wide range of wavelengths for science. Compared to Hubble, they collect much more light while covering much the same spectrum. To extend to longer wavelengths requires a colder telescope (see Fig. 5) and to reach shorter wavelengths requires greater control over both contamination and wavefront. Currently, access to wavelengths shorter than about 100 nm is restricted by the lack of mirror coatings that are both highly efficient in the UV and also everywhere else in the desired spectral range. Challenges at UV wavelengths include control of contamination of the cold optical surfaces and the need for

very smooth optical surfaces. The key factors surrounding mitigation and control of contamination are discussed in Sec. 3.10.

Larger apertures and shorter wavelengths require better wavefront control (WFC) to reach a diffraction-limited focal spot and here active segmented mirrors are an enabling technology. Observations into the mid-IR require cool optics—Spitzer, Herschel, Planck, and WISE point the way—and technology demonstration active mirrors[27] have demonstrated function down to 28 K. These mirrors have also shown that cryogenic mirrors need not be figured (polished) at cryogenic temperatures but can be built using room-temperature processes and will have the desired optical figure when cooled.

3.2 *Mission Architecture*

ATSA comprises two spacecraft, one carrying the telescope and science instruments, the other carrying a starshade 72-m-in diameter. Stowed into a package 7.81 m in diameter by 13.63 m high [including the launch vehicle adaptor (LVA)], the 6-m ATSA telescope can be launched into orbit at Sun–Earth L2 within the shroud of the SLS Block 2, 10 m ∅ payload fairing (PLF) long[28] launch vehicle or the SpaceX Starship+5-m extension.[29,30] Depending on the launch vehicle, the telescope is then boosted to Sun–Earth L2 or carried there within the Starship bay. The starshade inner disc is folded and the petals rolled into a cylindrical package (see the HabEx report[2] for more detail on the method) that measures ∼8.0 m high by 4.6-m diameter. Here we adopt the 72-m starshade package initially developed for HabEx (that mission concept eventually adopted a 52-m shade). Deployed, the starshade has twenty eight 16-m long petals arranged around a 40-m diameter inner disc. Although adequate mass capacity exists on the Starship to co-launch the starshade with the telescope, there is inadequate space and so the starshade would launch separately on a second Starship vehicle, using the standard fairing. For an SLS option, the starshade would utilize the SLS Block 1B Cargo with the 8.4-m PLF short-concept fairing. This two-launch mission concept gives a great deal of flexibility in scheduling, both during the development and science phases. Note here also that the starshade configuration could be adjusted to fit into a shorter, squatter cylinder by increasing the number of petals. Choosing 36 rather than 28 petals and assuming the same package volume would reduce the height to around 6.2 m and increase the diameter to around 5.2 m. Then stacking the starshade and telescope could potentially allow a single launch. More analysis would be needed to verify that.

The two spacecrafts are initially placed into similar halo orbits utilizing ground-tracking facilities. Before arrival at L2, the telescope sunshield and solar panels are deployed and the scarf cover is kept in place. Scarf deployment occurs in two separate one-time events as shown in Fig. 8. The sunshield deploys first to a fixed configuration. The scarf is rotated into position and locks to the barrel. After latching, the heaters and motors will not be reused and their wiring

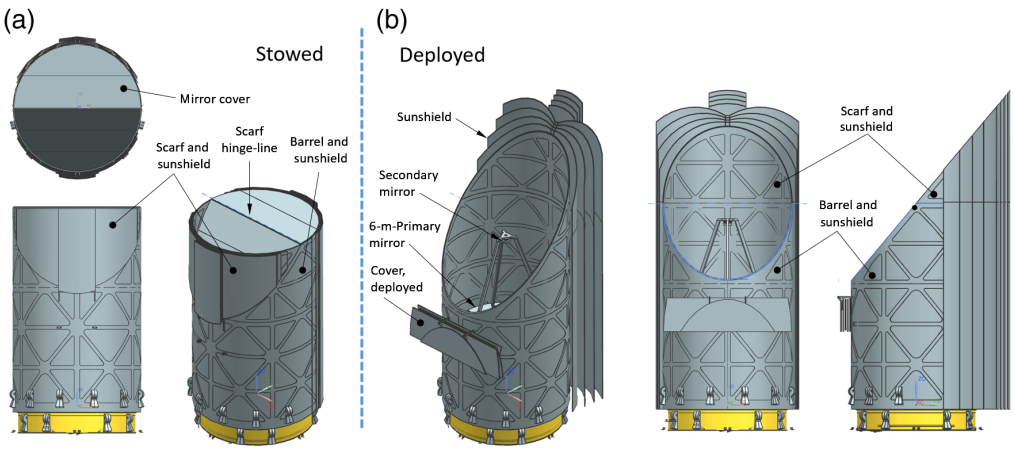

Fig. 8 (a) Telescope stowed configuration with scarf and cover in place and sunshield and solar arrays stowed. (b) Deployed configuration with scarf and cover unfolded and sunshield and solar arrays deployed.

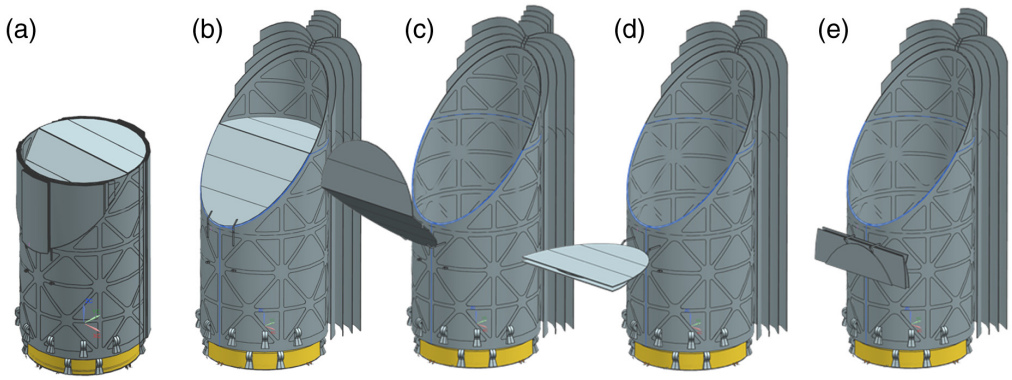

Fig. 9 (a)–(e) Telescope in the stowed configuration with scarf and cover in place and sunshield and solar arrays stowed. Scarf folds back and sunshield and solar panels are deployed. Telescope primary mirror cover opens and folds up close to the barrel. The lower sunshield closeout to the bus is not shown here.

harnesses will remain benign. The sunshield interface between the scarf and barrel is an SLI labyrinth interface, with shield plies interleaving without contact, similar to the SLI labyrinth interface used to protect the support structure of the JWST star tracker after deployment. After arrival, the telescope cover can be opened and folded away, as shown in Fig. 9. The cover is designed to deploy and restow and is folded when latched against the barrel to free as much area as possible for the radiator panels. Deployment is in a single-direction actuation, similar to common solar arrays and only slightly more complicated with a restowing requirement. The solar panel extends the length of the barrel, split at the scarf joint. Latching electrical connectors carry power between the sections.

Deployment of the starshade is described in Sec. 4. After check-out, its laser beacon is acquired by the telescope in the wide field camera.

Starshade relative position data acquired optically on the telescope are relayed to the starshade via an S-band link and the starshade then performs any required maneuvers. The basic telescope and starshade system design parameters are shown in Table 1, which shows both launch vehicle options.

Table 1 Telescope and starshade system design parameters.

	Telescope	Starshade
Diameter (m)	6	72
Design	Segmented, on-axis primary mirror	Numerically optimized
Primary mirror $f/\#$	1.09	
Operating temperature (K)	$\leq$100	$\leq$100
Cooling	Passive	Passive
Launch vehicles (SLS)	Block 2 10-m PLF-long	Block 1B 8.4-m PLF-short
Launch vehicle (Starship)	+5-m extension fairing	Standard fairing
OTA performance	Diffraction limited at 400 nm	
Optical bandwidth	110 nm to 5 μm (multiple ranges)	200 nm to 5 μm (multiple bands, 108% wide)
Pointing accuracy	2.0 mas	1 deg
Total FOV	12′×18′.6	40-deg to 85-deg Sun angle
Orbit	Sun–Earth L2	In formation

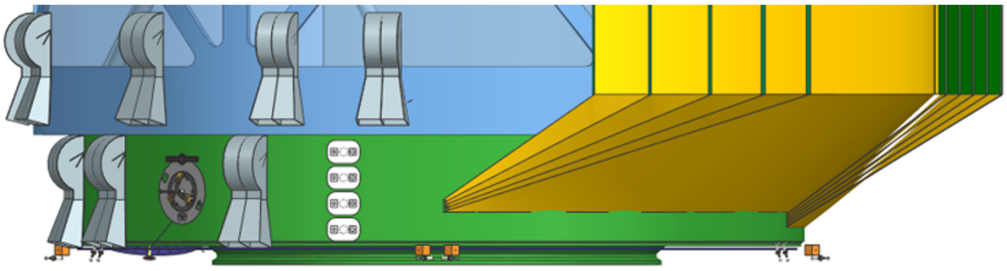

Fig. 10 The base of the telescope instrument bay and the bus section, showing the closure of the sunshield onto the bus, allowing observations with the telescope pointed directly away from the Sun. The keyhole-shaped objects are vents through which purge gasses escape before and during launch.

The telescope scarf permits observations as close as 40 deg from the Sun. The plane of the starshade can be positioned so that its normal is up to 85 deg from the Sun, so these two angles define the edges of the instantaneous FOR in starshade mode. As the Earth orbits the Sun, starshade observations can cover all of the sky except for small regions within 5 deg of the north and south poles of the ecliptic. For general science observations, the telescope can point up to 180 deg away from the Sun so that for general astronomy, most of the sky can be accessed at any time, the exception being the conical region within 40 deg of the Sun.

Since the telescope relies on passive cooling to reach its working temperature, the telescope barrel is partially wrapped by a five-layer sunshield as shown in Figs. 8–11. The sunshield is terminated on the bus as shown in Fig. 10, allowing observations with the Sun at the nadir angle. One solar array is placed along the length of the barrel on the outer spine of the sunshield (and split at the scarf joint), and the second solar array is located on the nadir side of the bus. The instruments are positioned behind the PM and arranged so that focal planes that need to be cooled are positioned near external radiators on the shaded side of the telescope and cooled passively, eliminating the power needs, thermal loading and vibration associated with cryocoolers. Figure 11 also shows the secondary mirror support struts within the barrel. The temperature at the top of the struts and therefore of the secondary mirror is about 60 K.

ATSA, like HabEx, uses microthrusters for attitude control rather than reaction wheels. Microthrusters produce extremely low vibration,[2] with noise power spectral density of 0.3 μN Hz$^{-1/2}$, as much as four orders of magnitude lower than reaction wheels. The low vibration induced in the telescope structure by the attitude control system (ACS) results in minimal dynamic distortion of the wavefront.

ATSA's science instruments include an ultraviolet spectrograph [multiobject ultraviolet spectrograph (MOUS)], a general purpose camera [multiobject visible-infrared spectrograph

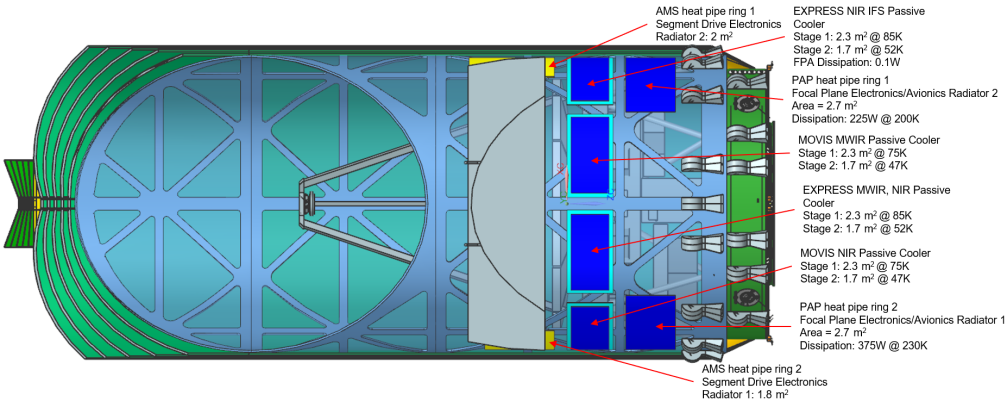

Fig. 11 ATSA thermal configuration. A five-layer sunshield protects the barrel, which is free to radiate to space on the shaded side. Arranged at the base of the barrel are radiators for cooling the electronics and the science focal planes.

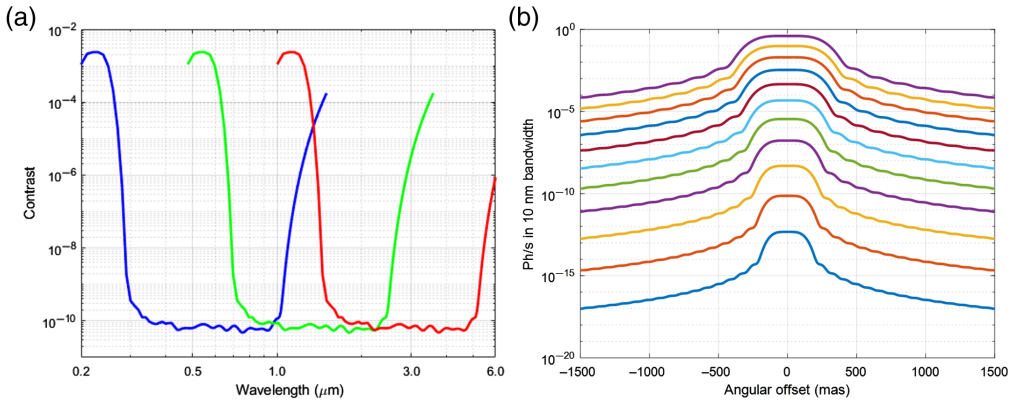

Fig. 12 (a) Contrast against wavelength for different starshade ranges. With the starshade at 120-Mm range, the blue curve shows the stellar contrast in the "visible" 300- to 1000-nm science band. To either side of that band the starshade "leaks" starlight, which can be used for starshade formation flying control. The green and red curves show the contrast for the IR1 and IR3 science bands, illustrating complete coverage of the spectrum. For clarity, the UV and IR2 bands are not shown. (b) The appearance of the starshade at the ATSA focal plane in thermal emission as the starshade range varies. The plot shows the mean profile (as the starshade rotates) of the thermal flux, taking into account the petal shape. The thermal flux increases as the maximum science wavelength increases from 2500 to 5000 nm in 250 nm steps. The starshade temperature is 100 K. ATSA resolves the starshade so that the center of the thermal PSF is flat, with the Airy rings seen extending outward.

(MOVIS)], and a starshade instrument [exoplanet range extended starshade (EXPRESS)]. In addition, the telescope carries two focal planes for attitude control during science observations. Each instrument (with the exception of MOUS) has multiple internal optical paths and detectors. We refer to these paths as "channels." The channel comprises the entire optical path from PM to detector, so that all channels share the telescope primary and secondary mirrors.

The starshade creates a shadow area within which the contrast ratio meets the 10^{-10} required for exoplanet science, accommodating the telescope aperture and the formation flying radius. The starshade is of the numerically optimized type[31] and the high-suppression region (Fig. 12) extends from 300 to 1000 nm at the nominal working distance of 120 Mm, providing a 108% working bandwidth and a 51-mas IWA (given as $IWA_{0.5}$) ($IWA_{0.5}$: the angle at which the planet signal drops by one half from the unobscured case). As shown in Table 2, this band can be moved to shorter wavelengths by increasing the starshade range from the telescope or longer by bringing the starshade closer in proportion to the desired center wavelength. Figure 12(a) shows the high suppression regions corresponding to those operating ranges.

3.3 *Optical Telescope Assembly*

Figure 13 shows the principal components of the flight system, consisting of the optical payload and its associated instruments and the standard bus parts. The optical telescope assembly (OTA) is formed by the 6-m-diameter PM and its underlying aft metering structure (AMS), three struts

Table 2 Example starshade operating bands, ranges, and dimensions.

RM12 starshade	UV	Visible	IR 1	IR 2	IR 3
Range (Mm)	180	120	50	35	24
$IWA_{0.5}$ (mas)	33	51	121	172	253
Lower edge (nm)	200	300	720	1020	1500
Upper edge (nm)	660	1000	2400	3400	5000

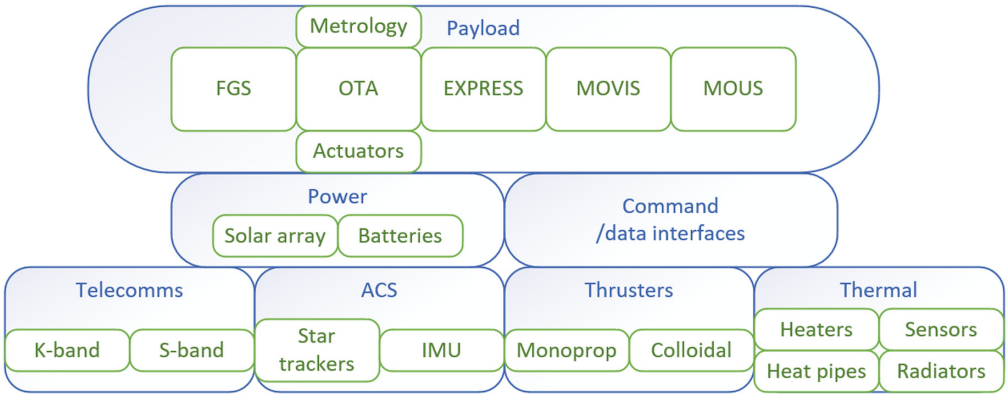

Fig. 13 The principal components of the flight system showing the payload and bus systems. K-band and S-band antennas, respectively, allow communication with the ground and the starshade spacecraft.

connecting that structure to the secondary mirror, and the secondary itself. Twelve outer segments of the PM (Fig. 7) each cover 30 deg of arc with 1285-mm radial extent, and six inner segments cover 60 deg of arc with 1390-mm radial extent. The central hole is 600-mm-in diameter. The gap between segments is 25 mm except where the surface is penetrated by the three secondary mirror struts, in these locations, the gap is 100 mm. Each PM segment, made of silicon carbide (SiC), contains an array of figure control actuators (FCAs) enabling the surface figure to be finely controlled. The segment is mounted via active bipods to the AMS, providing motion in six degrees of freedom (DoF). Segment area is $\sim 1.5\ \mathrm{m}^2$ for both inner and outer segments, a size within the current state of the art. Table 3 shows the mass breakdown of the PM and its components. The total areal density is $30.8\ \mathrm{kg\,m^{-2}}$. JWST's PM segments have an areal density of

Table 3 Mass breakdown of the primary mirror assembly.

Subassembly	Mass (kg)
SiC	410
Mount pads	130
Thermal/OS s	36
RBAs	113
SFAs	16
Potting cups	3
Beam launchers	16
Electronics	68
Cabling	39
Flexures	13
Total PMA mass (exc. AMS)	**844**
Mounted mirror assembly net area (m^2)	27.4
Density ($\mathrm{kg\,m^{-2}}$)	30.8
Optical area/segment (m^2)	1.4
Segment density ($\mathrm{kg\,m^{-2}}$)	22.8

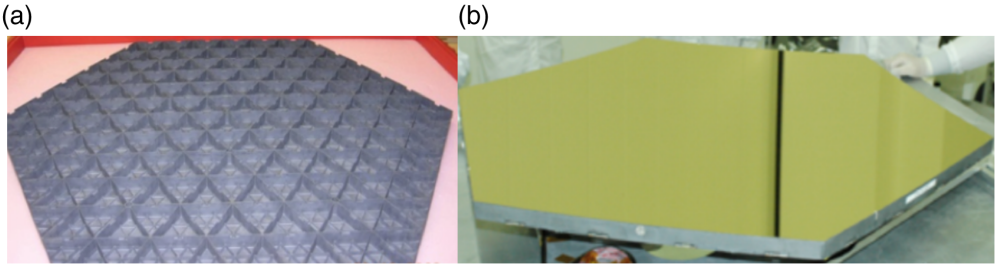

Fig. 14 SiC mirror from a technology development program showing (a) the ribbed backing structure and (b) the mirror surface. Actuators push or pull on the backing structure causing localized bending of the surface. The diameter is 1.35-m point-to-point.

$\sim$30 kg m^{-2}, greater than ATSA's segment areal density of $\sim$23 kg m^{-2}. JWST segment areal density had been increased during the design phase to meet stiffness needs under launch loads. JWST's and ATSA's total PM assembly masses cannot yet be directly compared, since ATSA's AMS mass has not been detailed, but we would expect comparable total mass.

The PM segments have solid-state electroactive ceramic actuators embedded in their isogrid open-back structure. These surface-parallel actuators can correct large figure errors with accuracy depending partly on initial figure quality and partly on actuator density. This approach borrows the SiC substrate and basic design demonstrated through the development and testing of numerous "actuated hybrid mirrors[32]" (AHMs), achieving 15-nm RMS SFE for mirrors up to 1.35-m size, as illustrated in Figs. 14 and 15. Actuators are placed within the ribs of the mirror backing structure, and as seen in Fig. 14, each segment contains a large number of possible locations. The WFE is inversely proportional to the density of actuators,[33] which also determines the upper limit of surface spatial frequency error that can be corrected. In-service SFE requirements will determine the final design of ATSA mirrors. The need to correct fabrication residuals and cool-down thermal deformations, as well as control mid-spatial frequency figure, will set the number and locations of the SFAs. The AHM mirrors demonstrated the ability to correct low-spatial-frequency figure errors by a factor of more than 100, from the $\sim$2-μm RMS incurred by facesheet bonding strain to $\sim$15-nm RMS (Fig. 15). The ATSA mirrors are expected to have lower initial SFE, as they will be polished to shape rather than bonded to a preform. Also the cool-down deformations of SiC substrates have been shown[32] to be small ($\sim$30-nm RMS). Assuming the initial figure error were specified as 100-nm RMS, a correction capability similar to that that AHM demonstrated would reach single-digit final RMS SFE, even with fewer actuators. More actuators mean greater correctability of initial errors, relaxing initial figure requirements. More actuators also mean lower amplitude residuals at higher spatial frequencies.

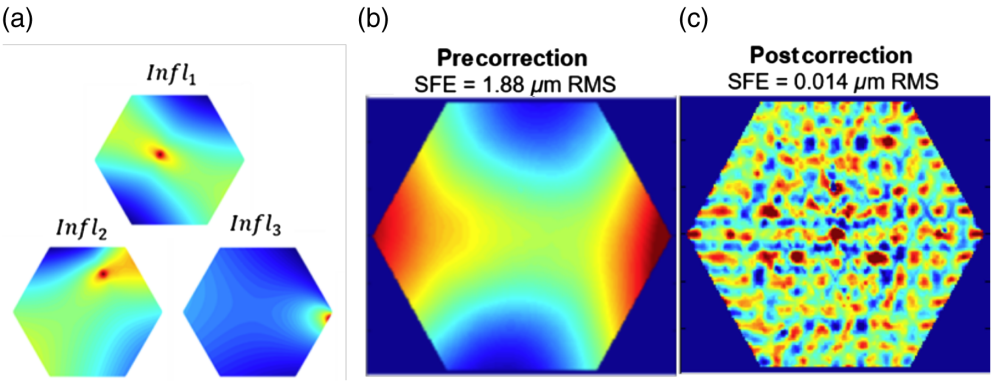

Fig. 15 The effect of actuators on the mirror figure. (a) Single actuators influence the wavefront both locally and globally. (b) The test mirror surface figure error before correction, which was dominated by release of the strain incurred by bonding the nanolaminate facesheet to the substrate. (c) The surface figure error after correction, showing two orders of magnitude improvement from 1.88 μm to 14 nm RMS figure error.

By varying the rib structure and the numbers of actuators, the required wavefront conditions can be met by design.

ATSA's mirrors depart from the AHM formula in two respects. First, using a polished layer of Si as the reflecting surface rather than a replicated nanolaminate metal foil, better thermal deformation properties are obtained. Initial figure errors will be much reduced at room temperature, compared to the AHMs (Fig. 14), which exhibited 1 to 2 μm initial figure error caused by release of nanolaminate bonding strain. The Si facesheet provides an isotropic surface layer that enables polishing to meet UV surface requirements, targeting a microroughness level of under 5 Å. Second, ATSA's mirrors will utilize cryocapable PZT actuators rather than PMN electrostrictive actuators, providing control authority both at room temperature and at the target operating temperature. Cryogenic testing of SiC substrates shows that cooling the mirror itself to 100 K or lower can be done without significantly degrading figure quality.[34] Cryocapable actuators have been characterized at temperatures as low as 25 K.[35,36]

The PZT SFAs are installed so that they impart near-zero strain in their zero-volt state at room temperature. The actuator–substrate attachments are also designed to compensate the thermally induced differential strain when the mirror is cooled to its intended operating temperature. This is achieved via a "reentrant" clip constructed from a material with CTE dissimilar to the substrate/actuator, counteracting the relative mismatch in thermal expansion. This approach minimizes thermally induced figure changes and allows the telescope to be operated both at room and cryotemperatures and meet the PM performance targets of 20-nm RMS WFE at both temperatures. The basic principle has been demonstrated[27] at the 15-cm scale using a 12-actuator cryogenic active mirror, testing at temperatures ranging from room temperature down to 28 K. The technology readiness level (TRL) of the AHM mirrors is TRL5, but the athermalization, Si-cladding, and specific actuator implementation designs for full-scale ATSA mirrors need demonstration. The current status of ATSA segments is TRL3.

The PM segments are attached to the AMS backplane via the RBAs: linear actuators arranged in a hexapod configuration to provide six DoF of motion control. The SM is also attached via RBAs to its support struts. Based on those used on JWST, the linear actuators have nanometer precision and several millimeter range.

Telescope pointing is maintained by the ACS operating together with the fine guidance system (FGS), inertial measurement unit (IMU), and star trackers (Fig. 16). The FGS and star tracker utilize different guide stars, with the FGS forming the higher-precision component. The ACS commands the microthrusters to maintain pointing during observations. For large moves, the ACS commands the reaction control system (RCS) thrusters.

A TCS ensures adequate telescope thermal stability for many hours of observations. The TCS maintains the temperatures of the mirrors, AMS, optical benches, and bus, activating heaters as required. External radiators reject heat from the instrument focal planes, instrument electronics, bus electronics, and equipment.

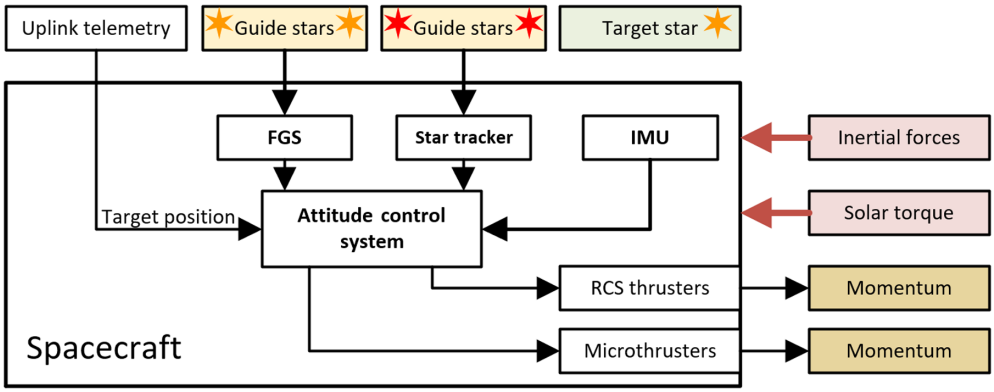

Fig. 16 Elements of the ACS: The FGS operates in conjunction with the IMU and star trackers to provide pointing and angular rate information. The ACS controls spacecraft pointing to match a target supplied from the ground using either microthrusters or RCS thrusters depending on the operating mode: science or slewing.

The PM is cooled passively by radiation to space and to the cold side of the shroud. To maintain thermal control, a low-mass thermal shield backs each segment, connected at the bipod attachment points.

Beneath the segments, the AMS provides a second thermal shield against heating from the spacecraft bus. The segment figure-control actuators are high-resistance loads with low-power consumption. Each presents a heat load of about 100 μW to the mirrors, which the thermal model (Sec. 3.4) showed to be negligible.

The AMS panel is connected via a kinematic hexapod to the payload interface panel (PIP), in which the spacecraft electronics and systems are attached. Figure 17 illustrates the layout. The barrel, which surrounds the telescope instrument bay, the mirrors, and the bus, is a stiff honeycomb structure mounted to the PIP. The design ensures that the barrel, telescope sunshield, and solar panels are disconnected from the optical metering structure except through the PIP itself. The instrument bay is located above the PIP, whereas the bus is located below. The instrument bay is enclosed by the barrel and the PIP and AMS panels, with the instruments themselves mounted to the AMS panel. The primary optical metering structure consists of the AMS panel, PM hexapods, and the SM tripod struts, stiffened by the laser metrology (MET) system and partially isolated by the active hexapod attaching the AMS to the PIP. The instruments are individual subsystems, each of which includes a separate thermal environment for the optics enclosure and for the isolated electronics that are close-coupled with minimal cable lengths. Radiator panels are close-coupled to instrument detectors and detached from the barrel, eliminating thermal strains, and dynamic coupling.

The $f/1.09$ PM's central aperture allows light reflected from the on-axis secondary through to the instrument bay behind the AMS. The secondary mirror has an optical clear aperture of 562 mm; an optical scraper that creates a clean edge around the mirror brings the obscuration up

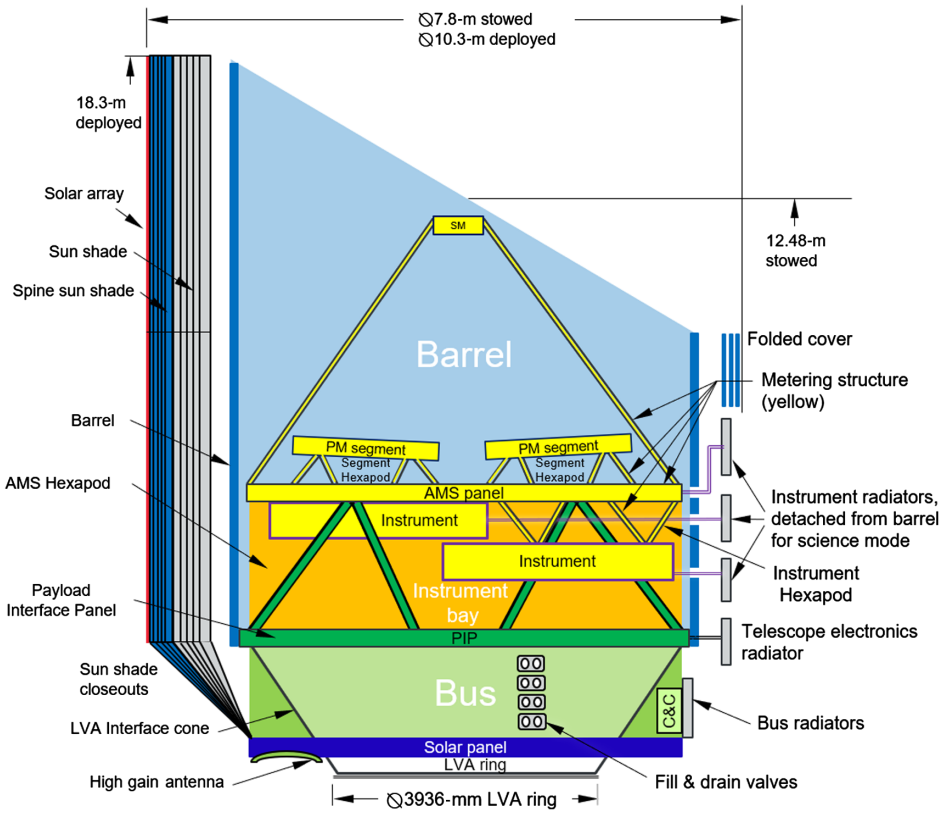

Fig. 17 Schematic view of the bus and payload. The PIP carries the spacecraft bus, the telescope barrel and, via hexapods, the telescope optical system. This arrangement partially isolates the optical system from disturbances induced on the barrel and bus by providing a limited connection between the components. The secondary mirror is also attached to the AMS via struts (not shown here) with active control of position.

to a diameter of 600 mm. All mounting structure for the secondary is behind the mirror, so as not to infringe upon the telescope aperture. In addition, three corner cube retroreflectors (part of the laser metrology truss discussed next) are face-mounted around the secondary between the clear aperture and the physical edge. Spaced 6000 mm from the primary, the secondary mirror is rigidly connected to the AMS via three struts, with actuators allowing active position control. The various instruments have either a tertiary or both a tertiary and quaternary mirror to provide the required wavefront qualities.

3.3.1 *Laser metrology and wavefront control systems*

The WFC system (Fig. 18) maintains the telescope in its design optical configuration, following postlaunch alignments. Onboard functions run continuously, operating the SFAs, RBAs, and laser truss metrology as needed. Telescope geometry is controlled by the laser truss metrology system (MET),[37,38] which consists of a number of laser distance gauges (LDGs)—compact heterodyne interferometers. Free-space laser beams from transmitter/receivers mounted to the PM segments are launched to three corner cubes mounted around the SM. (There is an ideal corner–cube–launcher geometry and additional retroreflectors at M2 might prove beneficial in a final design). MET measures the distances between each of the segments and the secondary mirror. By making six measurements per segment, the segment position and angular orientation ("pose") is determined. Figure 19 illustrates the layout. For clarity, the beams from only two segments of the PM are shown, but every segment carries six transmitter/receivers, located in three places. Similarly, a further six LDGs are mounted in a triangular configuration on the relay optics mounting structure, positioned directly below the AMS aperture and illuminating the three SM corner cubes. Thus the relative pose between the SM, the PM segments, and the relay optics can be measured to nanometer precision. The combined set of measurements enables precise monitoring of the telescope geometry. Using active relative position control of the PM and SM optics, effects such as long-term moisture desorption and short-term thermal expansion and contraction of the optical system can be eliminated.

The compact LDG beam launchers[38] (transmitter/receivers) fit in the gaps between segments. Figure 20 illustrates the transmitter/receiver concept. A single input laser beam is split into two branches and fed to modulators, creating two beams with a small difference frequency. These beams are routed as shown in the transceiver and two outputs are produced, one modulated at the

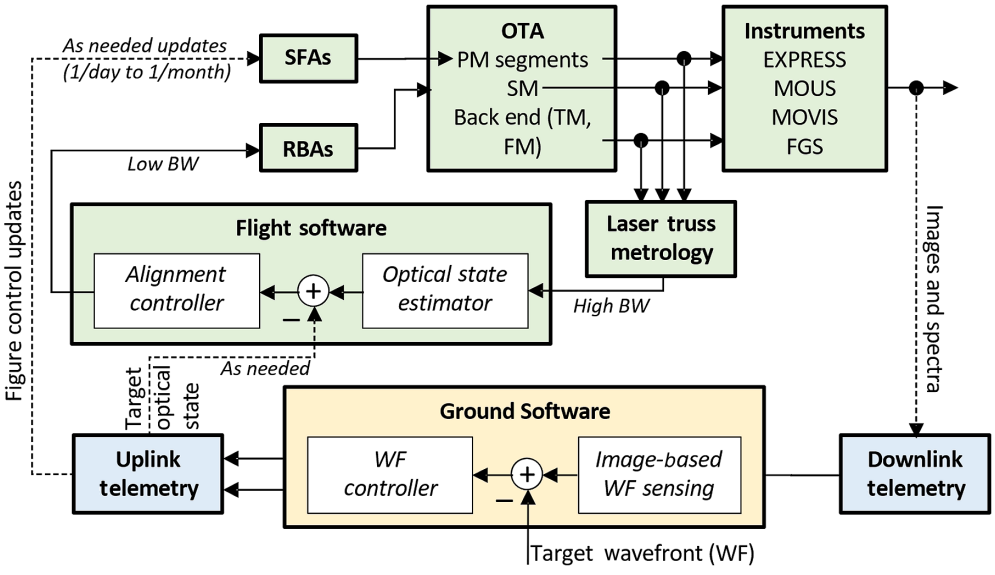

Fig. 18 Active WFC system. On-board functions (green boxes) run continuously to stabilize the optical alignments against slow, mainly thermally driven disturbances. Ground processing functions (yellow box) are carried out intensively early in the mission to initialize the telescope optics and then only very occasionally after that to compensate laser and figure drift effects.

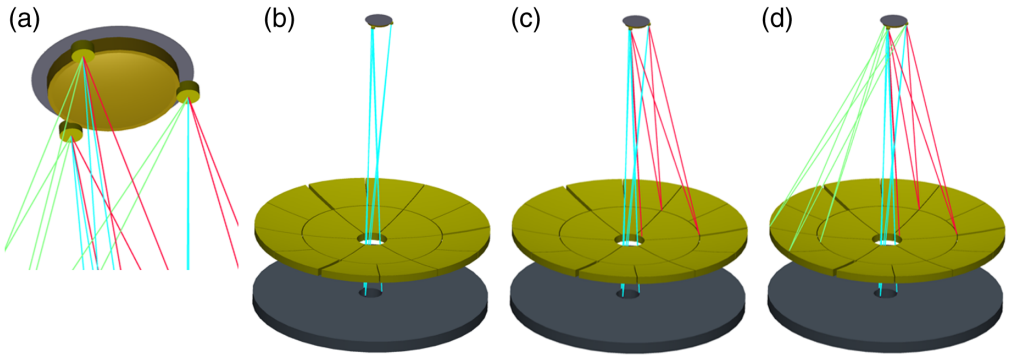

Fig. 19 Illustration of the laser metrology system. (a) Three or more (see text) retroreflectors attached to M2 reflect the metrology lasers back to their respective transmitter/receivers. (b)–(d) Six beams (cyan) are launched from the AMS (partly hidden by the primary mirror) through the central aperture of M1; six beams launch from each of the inner mirror segments (red, one segment set only shown); six beams launch from each of the outer mirror segments (green, one segment set only shown). Adding the remaining 16 segments, a total of 114 beams is launched and returned.

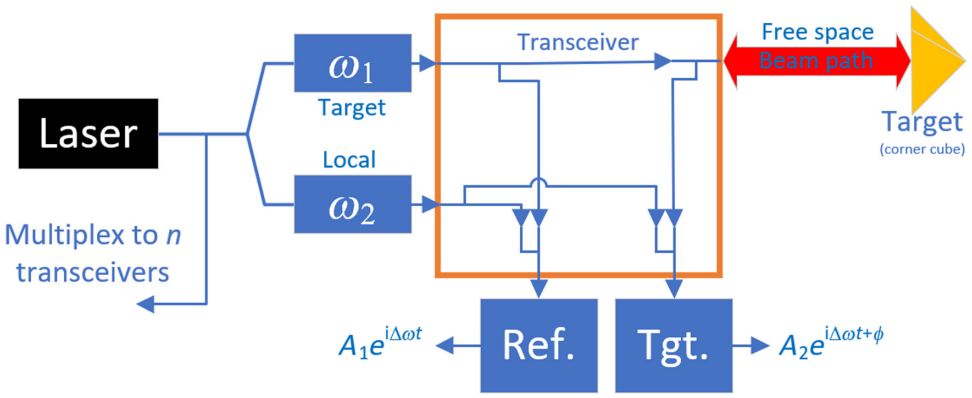

Fig. 20 Layout of the laser transceiver system. Two frequency-shifted laser beams (local and target) enter a beam-combination module that forms a transmitter/receiver. The target beam is transmitted to a corner cube retroreflector on a remote target and returns to be combined with the local beam. Internally, the local and target beams are also combined to form a phase reference. Two intensity-modulated output beams are detected and the phase shift between these outputs forms the metrology signal. The laser source is multiplexed via a series of inline fiber splitters to a number of transceivers.

difference frequency and the other at the difference frequency with a phase difference. This phase term is proportional to the distance change between the transceiver and the corner cube retroreflector placed on the target. A total of 114 transceivers is used, derived from three or more lasers using beam splitters to multiplex the laser sources. Only a few milliwatts total laser power is needed to produce all the beams. The ultrastable laser sources needed are in the development for space systems, such as GRACE-LRI.[39–41] ATSA's metrology beam launchers and adjacent fibers will operate at 100 K. This technology we assign TRL 4 (reduced from TRL 5 in the HabEx study) so that demonstration of ~1 nm performance in cold conditions is required to enable advancement to TRL 6.

MET signals, produced at 1 kHz with ~1 nm accuracy, are processed in a control system that continuously compares the pose of each optic to a commanded target pose. Pose errors are corrected by the RBAs at a 1-Hz bandwidth. This provides noise reduction by signal averaging; nanometer-level pose errors translate to picometer-level WFE performance over time scales of tens to thousands of seconds. Such performance levels are within the state of the art[37,38,42,43] with

optical sensors sometimes combined with other types. The MET-based OTA rigid body control system also provides a highly accurate servo control mode, where true optical pose commands, such as defocus, can be executed with nanometer precision in closed loop.

3.3.2 *Initial alignments*

After launch and cool-down, the segments of the primary will have random pose $(x, y, z, \theta, \phi, \omega)$ and will be $\sim$100 μm out of position and as-built initial surface-figure quality. Although AHM articles exhibited initial surface figure error of $\sim$2 μm rms, we expect the newer design to be near 100 nm rms SFE initially, thus requiring much less correction. Simple actuator models[33] indicate (and the AHM mirrors demonstrate) that the initial SFE can be reduced by a factor N at spatial scales down to $2/N$ of the aperture, using $\pi N^2/4$ total actuators, so that extremely low SFE is achievable. These pose, position, and SFE defects are corrected using image-based wavefront sensing and control (WFSC) methods, such as those developed and tested under the National Aeronautics and Space Administration (NASA) NGST program[44] and recently implemented on JWST.[45–49] These methods use star images and spectra recorded in the science cameras to initialize the telescope after launch. When pointed at a bright, isolated guide star, the initial images will appear broken up, with blurry subimages corresponding to the reflections of the star off individual segments scattered over the MOVIS camera focal plane. The first challenge for the WFSC system is to associate each subimage with the corresponding segment then to align each of them to the center of the focal plane and then to co-focus them. This process is made efficient by the MET controller in its servo mode. Then the segment figure errors can be measured individually, by taking in- and out-of-focus subimages for each segment in isolation. Ground processing of these single-segment images using phase retrieval methods[49] will determine its figure error and allow new SFA settings to be determined, to achieve excellent segment figure for each segment. Coarse phasing of the segments necessitates the use of broad-band light to assure coherent imaging across all wavelengths—sensing at longer wavelengths provides high dynamic range for this correction. Dispersed-fringe sensing[48] is employed. MOVIS' grisms create spectra on the focal plane and the piston offset between two segments (or eventually, two groups of segments), creates interference fringes revealing both the magnitude and direction of the offset. Then the RBAs are driven, using MET for fine control, to bring the segments into phase. This process brings the PM close to its final setting.

The next, fine phasing step in the WFSC initialization process uses full aperture phase retrieval. Residual segment figure errors, such as radius of curvature differences, are detected using focus diversity (small global focus shifts) and corrected to establish the final figure of each PM segment. Adjustments to the segment RBAs complete the best phasing of the PM as a whole. Finally, using phase retrieval at multiple field locations (employing MOVIS and the other cameras), the global misalignment of the PM, SM, and back-end optics is measured and then corrected by global motions of the SM and PM under MET control. The result is a fully collimated telescope with WF error of about 30 nm RMS.

3.3.3 *Telescope system stability*

Throughout the WFSC initialization process, the MET ensures that the telescope remains stable in the varying orbital environment. Once the observatory is fully phased, MET pose settings form the target pose for future operations. From that time, MET runs continuously to keep the optics in that configuration, so that science observations are always performed with optimized, known WFE performance. Occasional WFSC updates, requiring only phase retrieval WFE sensing at the center field, will be done to track and compensate drifts not visible to MET. These are primarily drifts in the MET laser frequency, slow creep that may occur in the PM segment figure, or creep within the instrument optical structures that may cause small misalignments. The interval between these WFSC maintenance updates will likely be long, weeks or months, once the telescope has settled into the orbital conditions.

Figure stability is provided by the stable thermal environment and low-net thermal sensitivity of the various optics. Much of the initial setup does not need to be executed on orbit, but rather can utilize the higher computational power and closer supervision available on the ground.

Changes in telescope attitude relative to the Sun affect the thermal loading, resulting in new internal heat distributions that are counteracted by the TCS. With tight thermal control of the segments and athermalization of the segment actuator system, changes to segment surface figures are minimized. Because the telescope metrology system and associated rigid body control system (RGB) control loop will run indefinitely, the set optical configuration is maintained despite changes to telescope structural lengths by short-term thermal variations, long-term outgassing, and creep.

Other control architectures have been proposed and may be more appropriate, for other missions. LUVOIR assumes the use of edge sensors between adjacent segments augmented by a few LDGs.[38] This can be a better solution if picometer-precision edge and gap sensors can be devised. Our approach has the advantage that its components already exist with nearly the needed level of performance.[37,44,46] NASA is funding industry studies to further develop the MET, edge sensor, and RBA technologies to go from nanometer to picometer performance for future coronagraph-equipped segmented aperture telescopes.[50,51]

3.3.4 *Fine guidance system*

The FGS views two small patches of sky offset in opposite directions across the optical axis of the telescope. A scan mirror in each optical path allows the observed patches to be placed anywhere in a 3′.1 FOR, ensuring that at least one bright star is available in each offset field no matter where the telescope is pointing. The control loop is closed using the microthrusters for precision, low-jitter adjustments. A relatively large angular distance between the two patches of sky enables precise measurement of telescope roll. Optically, the two guider systems are identical, other than having different flat fold mirrors. The optical layout consists of the telescope's primary and secondary mirrors, plus dedicated tertiary and quaternary mirrors forming a collimated beam at 133× angular magnification. The scan mirror is located at the collimated pupil and directs different sections of the FOR onto the focal plane via an off-axis paraboloid mirror. The optical design shows that RMS WFE across the FOR is <119 nm, so the FGS telescopes have diffraction-limited performance.

3.4 *Thermal Design*

The general scheme for the thermal layout is shown in Fig. 21. Solar illumination heats the structure and, since sunlight impinges directly onto the outer barrel assembly (OBA) shield hinge-line, additional shields are incorporated to minimize parasitic heating at this junction. The main OBA shield is made up of five discrete shields. Each shield is angled away from the next to operate as a V-groove radiator, causing photons to bounce between the specular surfaces, propagating to free space from the side of the shield. Internal shield layers are assumed to be 7 mil Kapton film with an IR emissivity of 0.02. The edges of the internal shield layers with a potential view to any solar heating have an additional outer layer of silver teflon co-cured to the Kapton. The outermost layer of the shield is assumed to be completely silver teflon. The OBA spine shields use the same materials (except for the final solar array layer). Figure 22 shows predicted OBA shield temperatures as a function of solar vector to OBA angle. Table 4 shows the driving temperature requirements. Where no particular requirement was levied, this table shows an ellipsis.

Both the inner parts of the barrel and the outer parts on the anti-Sun side have high emissivity to ensure excellent heat exchange with cold space. Since the barrel is short with a relatively long scarf, it provides a direct view of cold space for much of the interior of the barrel and at least a partial view for the rest. Figure 22 shows the results of thermal modeling of the barrel at a range of Sun angles. With the barrel side-on to the Sun ($\theta = 0$ deg), the superior surface of the solar array reaches 361 K and the sunshield reaches as much as 280 K, while most of the protected parts of the barrel, instrument payload volume, and bus are well below 100 K. At the nadir angle ($\theta = 90$ deg), the base solar array reaches ∼300 K and the barrel warms slightly. The temperatures of the primary and secondary mirrors and the instruments are shown in Fig. 23 and the model detail of the primary mirror is shown in Fig. 24.

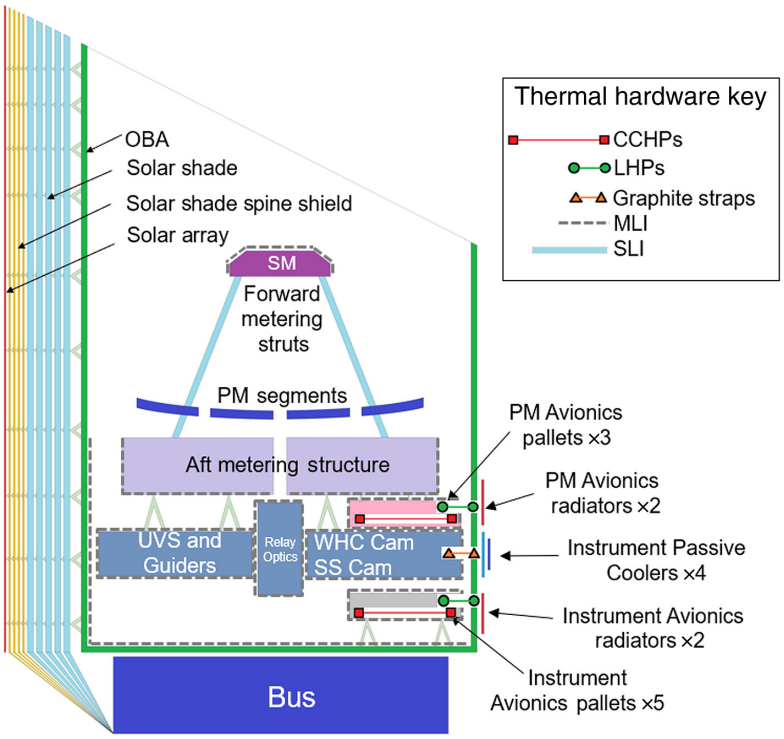

Fig. 21 The schematic layout of the thermal system. Heat pipes conduct heat from the payload adaptor plate and the AMS to radiator panels. Within the instrument bay itself, the instruments are cooled using a two-stage system (or a single stage for the warmer instruments) with a warmer panel set behind and extending beyond a colder panel. The warmer panel is connected to the instrument enclosure via heat pipes and the colder one to the detector via a thermal strap. MLI is added around the instruments and any free space optical paths as needed to maintain isolation.

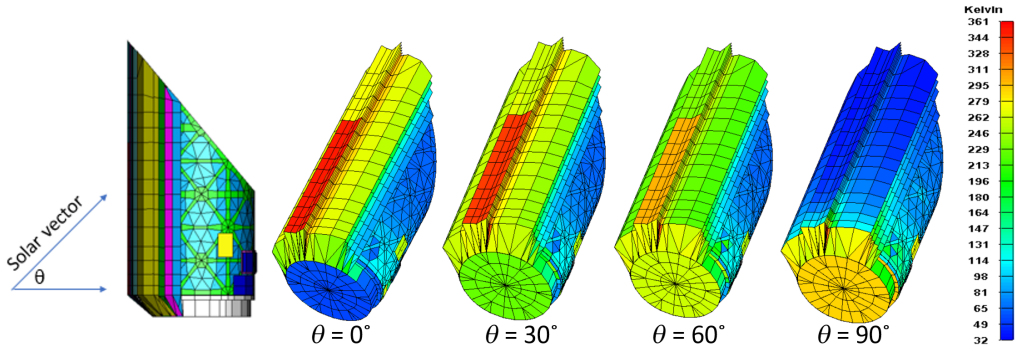

Fig. 22 Thermal model of the sunshield, solar arrays, and telescope barrel assembly. The angles represent the solar vector shown with the sun impinging at the side (0 deg) through to the base (90 deg). The five-layer solar shield provides excellent thermal shielding and much of the barrel is below 100 K at all Sun angles.

Beneath the AMS, the instrument boxes are passively cooled via heat pipes connecting to external radiators on the cold side of the barrel. The most thermally sensitive instruments are located on the cold, anti-Sun side of the telescope, with focal plane detectors positioned as near as possible to their radiator panels on the outside of the barrel. The uppermost panels cool the primary mirror surface control electronics, individual detectors, and the instrument optics and electronics in the instrument bay. The lower radiator panels dissipate heat from the power supplies and bus subsystems. The entirely passive thermal system eliminates the need for staged

Table 4 Temperature requirements.

Assembly/component	Operational temperature (K)
Telescope	
Primary mirror	≤100
Secondary mirror	≤100
AMS	100
Inner OBE (bulk average)	≤100
MOVIS	
UV FPA	—
VIS FPA	153
NIR FPA	77
MIR FPA	55
EXPRESS	
UV FPA	153
VIS FPA	153
NIR FPA	77
MIR FPA	55
MOUS	
UV FPA	—
Avionics	
PM drive electronics	≤250
Instrument electronics	≤250
Bus interface	
Payload interface plate	≤250

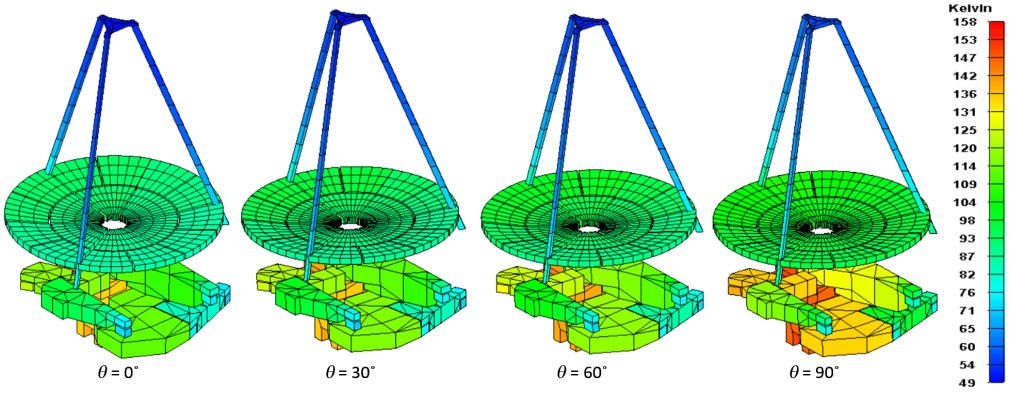

Fig. 23 Thermal model of the OTA and instruments with AMS removed for clarity. The primary mirror is at ~100 K (details shown in Fig. 24) and the instruments exhibit a range of temperatures depending on the Sun angle. Detectors are uniformly cold (cyan colors at the narrow ends of the boxes). The UV instrument, which does not have specific cooling requirements, is warmest at up to 158 K. At the nadir angle, there is some general warming of the instrument bay. Although this is currently considered acceptable, if necessary this could be addressed by adding a small sunshield at the side of the base opposite the sunshield closure.

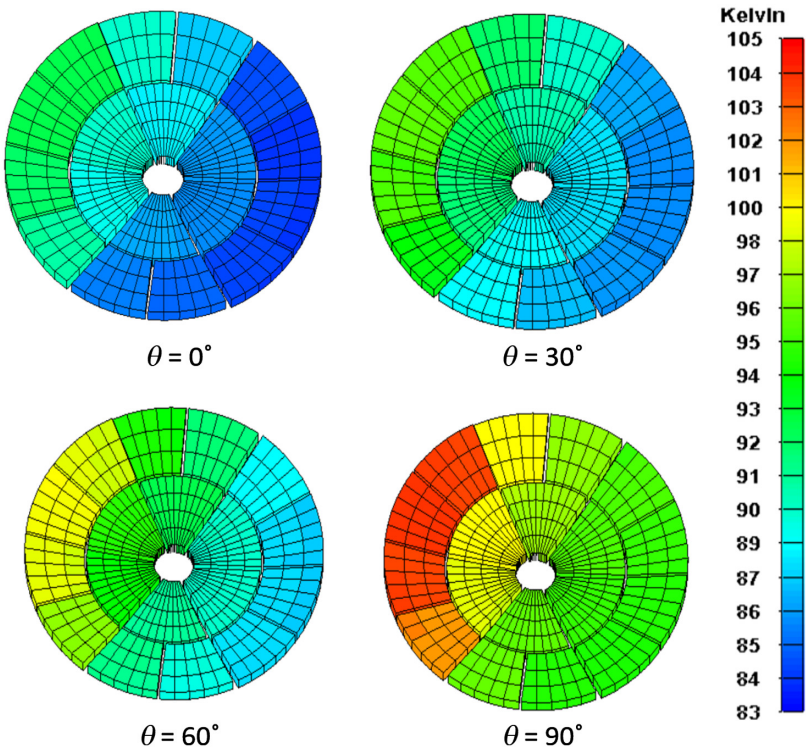

Fig. 24 Primary mirror segment temperatures as a function of solar angle. As anticipated, the nadir angle presents the worst case, with some segments warming to as much as 105 K with the target being an overall effective temperature of 100 K or below. These warmer segments do not cause requirements to be exceeded, however, since the radiation from the primary mirror as a whole is equivalent to 87% of the radiation from a uniform 100 K primary.

isolation with active cryocoolers, allowing bus mass to be reduced and vibration sources removed.

A passive radiator is included for each cold instrument (Fig. 25) and the attachments allow for differential motion between the OBA and radiators during launch. Mounting bipods protrude through apertures in the OBA allowing radiator installation after instrument installation. This configuration allows thermal testing of each instrument as an independent unit. Flexible graphite straps run directly between the focal planes and second stage of each radiator. Each of these passive coolers is sized to reject up to 1.5 W of focal plane array (FPA) dissipation at 55 K. This assumption is conservative for current focal plane selections. Inside the instrument bay, individual instruments are contained within enclosures mounted to the AMS optical bench. Each detector is close-coupled via short links to one of four 2.7-m^2 two-stage radiators. Figure 25 shows the enclosure temperatures of key instrument channels and their respective radiator panels.

The heat load from ATSA avionics is substantial. A 35-W avionics chassis is allocated to each primary mirror segment (630 W total). These chassis are attached to three separate thermal pallets (mounted via titanium flexures to the AMS) carrying embedded ammonia constant conductance heat pipes (CCHPs) (Fig. 21). The pallets are thermally linked via three compact ammonia loop heat pipes (LHPs) to two warm radiators mounted onto the OBA (Fig. 26). Both radiators have internal ammonia CCHPs to increase radiator efficiency. Survival heater circuits are placed on both the avionics pallets and radiators to prevent ammonia from freezing when avionics are not operating. The three segment drive avionics pallets and the larger wiring harnesses are fully enclosed with multilayer insulation (MLI) (effective e^* of 0.03), and the temperature of the electronics is low (250 K nominal) to prevent heat transfer to the primary mirror. A high-quality MLI enclosure is critical here (e^* of 0.03 is assumed).

Instrument avionics dissipate 550 W spread over 23 separate avionics chassis. These avionics boxes are for focal plane interface electronics, motor drive electronics, solid-state recorders,

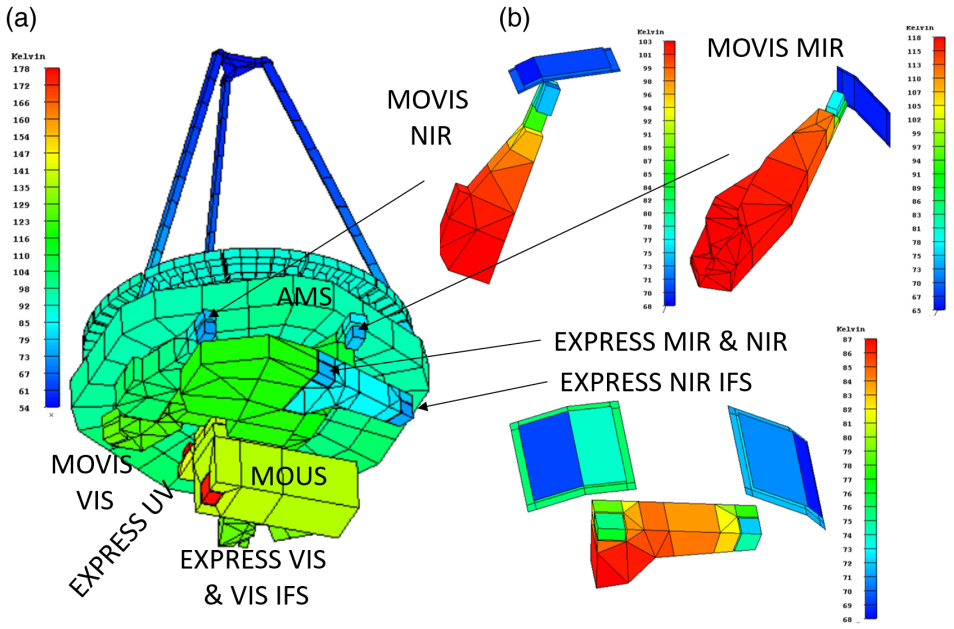

Fig. 25 (a) General thermal view of the instruments beneath the AMS. The AMS temperature is ~90 K, and the MOUS temperature is ~135 K. (b) The instrument enclosure temperatures for the cooler channels and detectors together with their detector radiator panels.

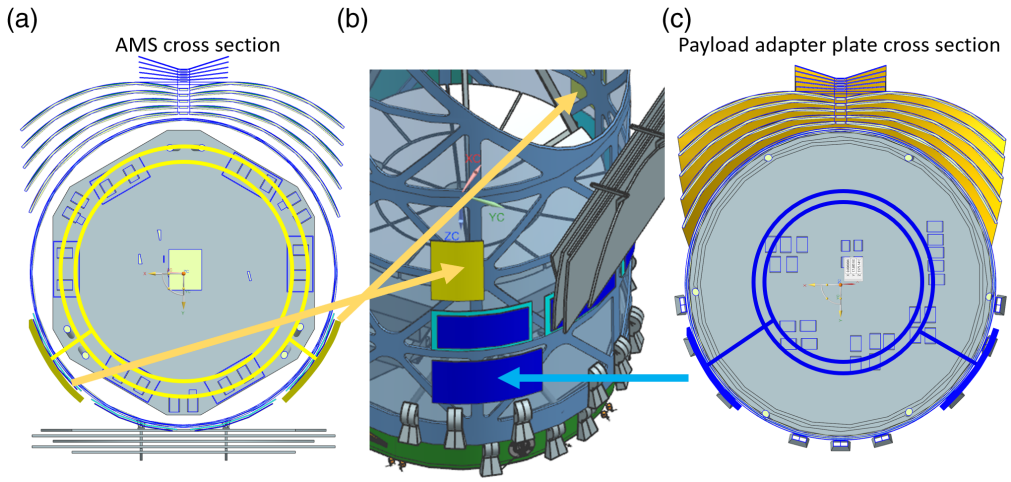

Fig. 26 (a) Circular heat pipe layout at the AMS. Two rings connected to external radiators (b) provide cooling for the AMS-mounted electronics. (c) A similar layout at the payload adaptor plate provides cooling for the bus electronics.

GNC components, etc. The boxes are arranged on five separate avionics pallets with embedded CCHPs. The pallets are either suspended from the AMS or supported from the PIP to minimize harness lengths and linked to each other by dual-bore CCHPs to the PM drive electronics pallets. Two external radiators mounted to the OBA are connected via flexible LHP assemblies. Each avionics pallet is fully enclosed with MLI and kept cool (250 K).

To isolate the internal spacecraft bus from the external environment and to minimize thermal gradients, much of the spacecraft bus will be blanketed. MLI blankets and thermal isolation washers will be utilized between the Sun-facing solar array and the sunshield, and between the nadir mounted solar array and the external radiators, thermally isolating these heat sources from the bus. Blankets and conductive isolation ensure no net heat exchange with the instrument deck. Cooling for bus subsystems mounted inside the bus will be provided by two 3.1-m^2 radiators on

the bus cold side. The radiators are connected to set of jumper heat pipes and these jumpers are connected to circular ammonia-filled, constant-conductance heat pipes embedded into the base mounting panel. The pipes ring the inside of the bus, providing easy access to cooling and are connected to heat sources, such as batteries, power conditioning units, and bus electronics. Figure 26 illustrates the concept.

Cooling for the instrument panel (the AMS) is provided in a similar fashion. Two 2.7-m^2 radiators for focal plane electronics and two 2-m^2 radiators for segment drive electronics are placed on the spacecraft's cold side and connected via jumper heat pipes to a set of circular ammonia-filled, constant-conductance heat pipes embedded into the AMS panel separating the instrument bay from the bus. Miscellaneous heat sources, such as filter selection motors, are connected to the heat pipe ring for cooling. Heat pipe and radiator sets may be combined via manifolds to offer higher margins for heat rejection area.

3.5 *Bus Architecture*

The bus equipment is placed in a tapered cylindrical volume created by the PIP and the LVA. The base of the volume is formed by the nadir solar array, located immediately above the launch vehicle interface ring that provides the interface to the launch vehicle via a payload adaptor fixture (PAF). After launch, the payload separates from the launch vehicle at the PAF interface.

Figure 27 shows the telescope stowed within both the Starship shroud (+5-m extension) and the proposed SLS 10-m long fairing. Dimensions are based on the SpaceX Starship Users Guide[30] and the SLS Mission Planner's Guide.[28]

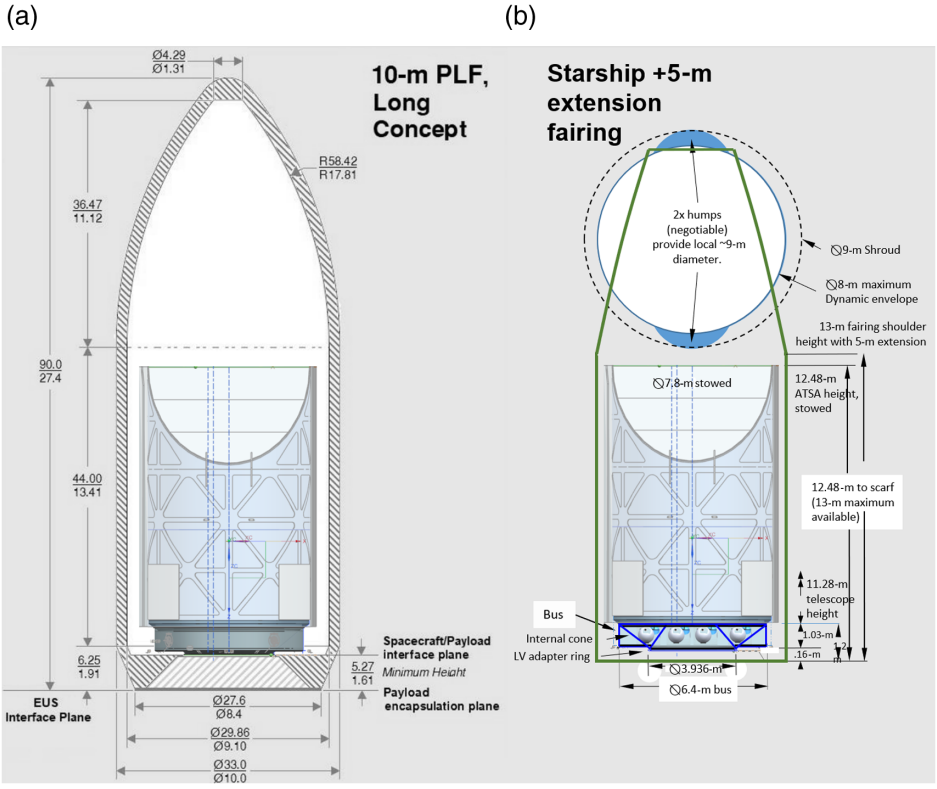

Fig. 27 Schematics showing possible launch vehicle fairing options. (a) The telescope within the envelope of the proposed SLS PLF 10-m long, leaving about 0.9 m of height to spare. (b) Within the SpaceX Starship +5-m extension shroud. In (b), the thick green lines delineate the dynamic envelope. A plan view is overlaid at top, illustrating the negotiable volumes (blue areas) within the fairing. The stowed telescope fits within the cylindrical section of the fairing with 0.52-m height to spare. More margins exist within the conical section of either fairing.

The bus includes the following.

1. Hydrazine monopropellant thrusters used for station-keeping and large-angle attitude maneuvers, and the colloidal microthrusters used to maintain precision pointing during science observations, together with their associated fuel and propellant tanks.
2. The ACS, based on a pair of externally mounted star trackers, laser gyros (for coarse control and maneuvering) and signals provided by the FGS cameras (fine control) in observation mode.
3. The power system, which conditions and directs power from the fixed solar arrays, providing power to the instruments, heaters, and other systems including the spacecraft electronics.
4. The communications systems. One system transmits and receives data, commands, and telemetry to and from the ground. The second system communicates with the starshade via an S-band link, providing modal commands and formation-flying data during observations.
5. The TCS.
6. The flight computer for command and data handling (CDH).

Figure 28 shows bus equipment mounted on the cruciform panels, the sloping walls of the LVA cone and the nadir panel. Beneath the circular panel that closes out the bottom of the bus volume at the LVA ring is the nadir solar array, which also contains the high-gain antenna (HGA). The central cone from the LVA to the PIP is a solid layup of graphite composite. The cruciform, PIP, and nadir structural panels are sandwich-structured composite face sheets and aluminum honeycomb core with thickness adequate to provide stiffness against launch loads. Metallic and composite secondary structures and bracketing support the solar panels, propellant tanks, and bus subsystems. Primary load paths pass from the primary mirror through the AMS hexapod and into the PIP, and from the telescope barrel to the PIP, down to the LVA and PAF via the stiffened cone. The stiffening shear walls, cone, and panels of the bus support the 12,745-kg vehicle dry mass with a good portion of the propellant mass being transferred directly to the LVA ring via the nadir plate.

3.6 *Propulsion*

Two independent propulsion systems provide maneuvering and attitude control. Monopropellant thrusters provide large thrust enabling rapid slewing, whereas colloidal microthrusters handle the solar torques during science observations. The monopropellant system consists of one 440 N main engine (e.g., Rocketdyne MR-104J, $I_{sp} = 220$ s), four 22-N thrust vector control engines (e.g., MR-106L) enabling three-axis control, and sixteen 4-N attitude control engines (e.g., MR-111G), enabling six-axis control. A monopropellant system is preferred over a bipropellant

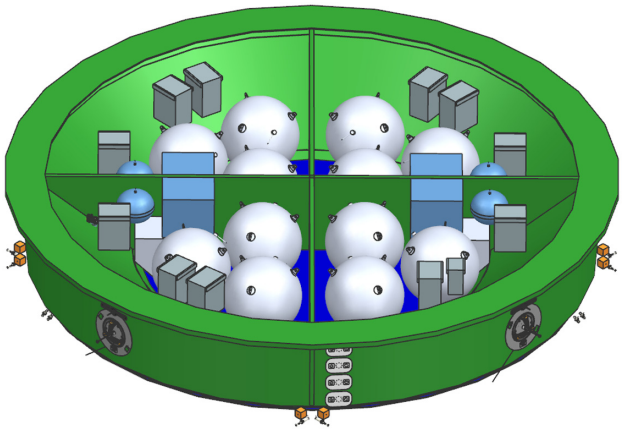

Fig. 28 Bus model showing tanks for 2660-kg hydrazine and 105-kg colloid propellant and volumes for the control valves (blue boxes) and fill and drain valves (gray boxes). Spacecraft electronics are mounted outside the cone, enabling direct cooling via external radiator panels.

Table 5 Mass summary budget assuming an SLS launch.

Subsystem	Mass (kg) CBE	Mass (kg) CBE with 43% margin
PM	844	1207
SM	10	14
MOUS	150	215
MOVIS	350	501
EXPRESS	450	644
Electronics	550	787
AMS	550	787
SM support	50	72
Barrel	1900	3575
Radiators/thermal	800	1144
Payload bay	480	686
Cabling	700	1001
Cover	60	86
OTA total	6894	9858
Bus	3500	5,005
Sunshield/solar	950	1359
Hydrazine propellant	1164	1164
Colloidal propellant	200	286
Dry mass	11,344	16,222
BOL mass	12,034	17,209
Wet mass	12,708	18,172

system because there is only a single component to refuel, but it carries a mass penalty owing to a typically 30% lower specific impulse.

By removing the reaction wheels commonly employed for attitude control on spacecraft, ATSA benefits from an extremely low vibration environment, while retaining exquisite attitude control. Microthrusters of different types have flown on both Gaia[52] (cold gas type with N_2 propellant) and Laser Interferometer Space Antenna (LISA) Pathfinder[53] (electrospray with colloidal liquid propellant) and are in continuous development for use on other missions. The colloidal type provides much higher specific impulse (quoted values ranging from typically from 180 to a few 1000 s) than the cold gas type ($I_{sp} \sim 60$ s) and is therefore specified for ATSA. Thrusts in the 10- to 100-μN range are currently available with the thruster with 18 emitter heads developed for LISA. Thrust resolution is as fine as 0.1 μN. Newer developments[54] promise 20 mN in a package measuring $\approx 180 \times 180 \times 45$ mm.

In an L2 orbit, solar torques will be $\sim$3.0 mN m, based on the solar photon flux, assuming 4.5 m between the centers of mass and pressure, 80% absorption on the solar arrays, and reflection of the remaining 20%. The ATSA telescope barrel has an area of about 18×7 m^2 with the sunshield deployed. To avoid placing electrospray thrusters (which would need to be heated and have heated supply lines) along the telescope barrel, the thrusters are placed near the base, attached to the bus. A single unit of the experimental thruster would be capable of producing as much as 86 mN m of torque at this location, so four somewhat smaller units would suffice and provide control over roll, pitch, and yaw.

ACS monoprop thrusters are mounted in pairs at eight locations, four sites at 90-deg intervals around the exterior of the bus and an additional four around the barrel about half way along, providing adequate torque control. Sizing the propellant loads for pointing control, slews, TCMs, and stationkeeping for a 5-year mission (based on scaled-up[55] HabEx 4.0 figures) results in 2660 and 105 kg mass budgets for monoprop and colloid, respectively, before margin. Refueling ports utilizing Vacco type II resupply valves on the exterior of the spacecraft bus allow replenishment of consumables via robotic servicing to extend operations.

3.7 *Mass*

The spacecraft wet mass with 43% margin applied is about 18,200 kg [see Table 5 for current best estimate (CBE) masses]. This is roughly 10% less than LUVOIR-B. More massive components of the OTA are the barrel, the primary mirror, the electronics, cabling, and AMS together with the sunshield and solar arrays. The bus mass is similar to that of LUVOIR-B. Propellant needs for insertion into and maintenance of the Sun–Earth L2 halo orbit are calculated by reference to LUVOIR-B, which assumed four mid-course correction maneuvers and subsequent orbital insertion at around 100 days and a 10-year mission. In this table, launch on the SLS Block 2 Cargo with the proposed 10-m PLF long fairing option and EUS providing lift to L2 is assumed. The amount of colloidal propellant on the telescope spacecraft is sufficient for 10 years of attitude control. After orbital insertion, the spacecraft has a beginning of life mass of 12,034 kg. In the case of launch on the Starship (capable of 150,000 kg to L2 after refueling in low-Earth orbit), payload hydrazine requirements could be reduced by as much as 674 kg, assuming the Starship vehicle is used to insert the telescope directly into its final orbit. The Starship would then return to Earth. Thus viable launch vehicle options are already at least in the concept phases.

3.8 *Power*

The power system consists of solar arrays, batteries, distribution cables, and interface hardware. Aft-mounted solar panels with area 29 m^2 and barrel-mounted solar panels with area 23 m^2 provide power. The aft-mounted panels are fixed, whereas the barrel-mounted panels are deployed after launch by extending them laterally. They provide a minimum of 3300 W when the telescope is pointed 40 deg from the Sun and 4200 W at 180 deg from the Sun. Peak power consumption of 3050 W occurs while science data are downlinked during observations (see Table 6). Lithium ion batteries with 3000 Ah capacity at 3 V provide 3 h of power after launch, maintaining capacity above 70%. The same battery system provides backup power in normal operation and in safe mode.

3.9 *Communications*

The communication system supports tracking for navigation via NASA's Deep Space Network and downlinking of science data. The Ka and X bands (6.5 $Mb\,s^{-1}$ and 100 $kbp\,s^{-1}$, respectively) are used for these communications. A single deployed, gimballed HGA mounted on the telescope bus enables science observations with simultaneous downlinking. (Alternatively, science data could be stored on board and down-linked periodically to avoid any issues with vibration from the gimbal. Another alternative would be two fixed phased array antennas enabling continuous vibration-free data transfer.) A link is provided between the telescope and starshade by an S-band patch antenna placed on the back of the secondary mirror. This low-bandwidth link (100 bps) conveys starshade formation-flying data and operation mode signals bidirectionally, as well as providing a time-of-flight measurement that enables starshade range sensing.

3.10 *Contamination Control*

Buildup of contamination on optical surfaces, both particulate and molecular,[56] degrades optical performance. Particles on optical surfaces obscure, absorb, and scatter incident light, whereas molecular contaminants reduce signal by absorption, scattering, and thin-film interference effects. These effects accumulate with each successive optical surface, so that the total loss

Table 6 PEL and summary budget.

Subsystem	Power during mission phase (W)							
	Launch	Cruise	L_2 insertion	EXPRESS	MOUS	MOVIS	Downlink	Safe
ACS	0	2	15	15	15	15	15	2
CDH	40	40	40	40	40	40	40	40
Instruments	0	0	0	630	630	630	630	0
Monoprop system	30	1	360	1	1	1	1	30
Electrospray propulsion	0	20	20	25	25	25	25	20
Telecom	75	75	75	140	75	140	170	75
Thermal	410	410	810	810	810	810	810	410
Power	60	60	80	150	150	150	150	70
Subtotal	**615**	**608**	**1400**	**1956**	**2091**	**2061**	**1841**	**647**
Contingency and margin (43%)	264	261	602	841	899	886	792	278
Distribution losses	31	30	70	98	105	103	92	32
Total	**910**	**900**	**2072**	**2895**	**3095**	**3050**	**2725**	**958**

in the optical chain can be estimated by summing the loss at each element. Contamination tests[57,58] have shown the presence of polymerized materials on mirror surfaces that degrade performance in the UV.

Sources of particles include those shed from surfaces and from cleanroom personnel, together with general fallout in the cleanroom. Particles may redistribute during launch. Molecular contamination sources include manufacturing process residues, integration and test processes, material outgassing and redeposition, and deposition of propulsion byproducts. The resulting optical effects are strongly dependent on wavelength. They are most serious at shorter wavelengths but may be important at longer wavelengths too.

Contamination controls (CCs) are required for ATSA, both to limit degradation and also to recover from degradation if it occurs, so that the observatory can maintain its required performance throughout mission life. An effective CC program will have several elements, guided by quantitative per-element contamination budgets and designed using CC modeling incorporating molecular generation, transport and deposition, particle redistribution, and effects peculiar to the space environment.[59] As the design evolves, iterations of the transport model keep track of developments. These CC models and methods are grounded in the extensive experience gained on missions including Hubble, Galex, Spitzer, Herschel, and Planck.

An effective CC program thus begins during the project design phase with these main elements.

- Materials selection for all parts of the telescope and instruments that considers outgassing and deposition behavior and rates, enabling prediction of signal impacts for all wavelengths.
- Development of viable procedures for processing materials and assemblies to remove contaminants, such as cleaning, bakeouts, and purging.
- Incorporation and modeling of internal and external venting paths into the design of the telescope and spacecraft structures, including filtered vents, while considering surface view factors and spacecraft-specific transport factors, to minimize deposition on critical surfaces.
- Design of instrument enclosures to limit exposure of optics, including the telescope outer barrel and aperture cover.

- Development and enforcement of contamination budgets by system engineering aided by continuously updated modeling.

During fabrication, assembly, and test, contamination will be controlled by materials processing, cleanroom protocols, frequent cleanliness inspection and monitoring, and surface recovery cleaning protocols. As each assembly is closed out, cleanliness will be preserved using remove-before-flight and in-process protective covers, with gaseous nitrogen purge to instrument enclosures.

During launch the entire system will be kept above the dew point. Once in space, the mirrors and other optical surfaces will be kept warm by heaters, as the rest of the system cools radiatively. As the barrel and bus surfaces reach operating temperature, they act like a cryogenic vacuum pump to condense residual outgassed materials, trapping them away from the optics. After a suitable interval, the optics are allowed to cool to working temperature. This scheme has been used successfully by Spitzer and several other cryogenic missions.

Once in operation, performance will be monitored to detect any contaminant buildup. As needed, periodic decontamination operations will be conducted, using heaters to warm affected components, displacing any accumulated volatile contaminants onto much colder, nonoptical surrounding surfaces.

ATSA spacecraft design places the hydrazine monopropellant thrusters and the colloidal microthrusters at the base of the telescope barrel and on the bus, pointed away from the aperture. Then paths to the critical optical surfaces will pass via large, cold surfaces that trap contaminants. The very high-exit velocity and the very low volume of the microthruster propulsion also limits the potential for contamination. A detailed assessment of thruster plume dynamics will be conducted for ATSA, but the risk to the sensitive surfaces is considered low.

Any UV telescope must be carefully engineered to control contamination and ATSA is no different: it must reach orbit and operate with very little particulate or molecular contamination of its optical surfaces. What is different is its cold operational temperature and this is a significant advantage. By keeping all optics warm during launch and initial orbital flight, then letting the surrounding nonoptical structures go cold, ATSA has built-in traps for outgassed volatiles. As the optics are finally allowed to go cold, the adsorbed volatiles will freeze permanently in place on the trapping surfaces.

As an example, Fig. 29 shows the result of thermogravimetric analysis of outgassed materials from a commonly used RTV adhesive (S691).[60] A quartz crystal microbalance (QCM) is cooled to 80 K under vacuum (10^{-10} to 10^{-8} Torr) and allowed to accumulate material evaporating from

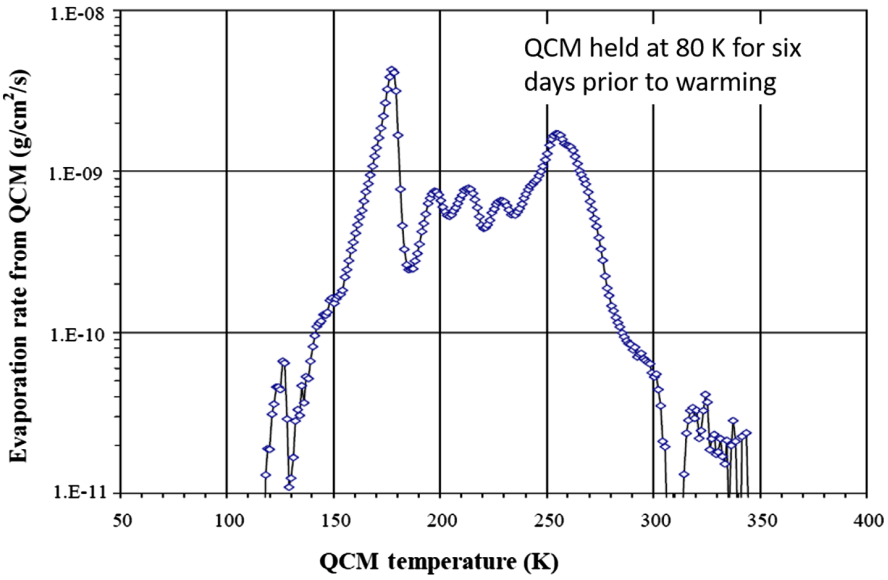

Fig. 29 The outgassing rate of accumulated materials from a cold surface as the temperature is raised from 80 K over a period of 144 h (data adopted with permission from Ref. 60).

a nearby piece of cured RTV, maintained at 333 K. After six days, the RTV sample is removed and the QCM is slowly heated over a period of 144 h, allowing the accumulated material (consisting of a wide range of chemical species, water being a major component) to evaporate or sublimate. This figure shows that below ~120 K, the evaporation rate is below 10^{-11} g cm^{-2} s^{-1}. This implies that, at these low surface temperatures, material exchange between surfaces is at extremely low rates and that clean optical surfaces will remain uncontaminated for long periods. A second implication is that local heating of contaminated surfaces can be employed to boil off material and trap it on surrounding colder surfaces. ATSA's cold temperatures thus offer the potential for truly robust on-orbit CC.

4 Starshade

4.1 *Overview*

The starshade provides exoplanet science capability from the near-UV to the MIR. Successful operation of the starshade at longer wavelengths requires the starshade to appear cool to the telescope, so that thermal radiation from the shade does not limit detection. Compounding this effect is the need to bring the starshade closer to make longer wavelength observations; the starshade is operated at constant Fresnel number given by $r^2/\lambda Z$, where r is the radius of the starshade and Z is the range. Having a reflective material on the Sun-facing side of the starshade, using multiple layers (rather than just three for HabEx) to form the optical shield (OS) and operating the shade at advantageous Sun angles to limit its illumination, all help to lower the starshade temperature. For example, with the starshade normal making an 80-deg angle to the Sun, the insolation is 4.4× less than at 40 deg, reducing the shade's absolute temperature by ~70%. Figure 33 shows the effect on the AB magnitude of the starshade, with significant decreases in starshade brightness for Sun angles larger than 40 deg. Objects in an annular field almost perpendicular to the Sun-telescope line can be observed with a cool starshade and as the year goes by, most of the sky can be observed excluding the two circular areas 14 deg in diameter centered on the ecliptic poles.

4.2 *Starshade Deployment*

After launch, the shroud is discarded and the second stage sets the trajectory toward L2. Once on track, the second stage is discarded and any required trajectory correction maneuver (TCM) takes place after an orbit determination undertaken within a couple of days. Immediately following launch the starshade bus is powered by solar panels [colored blue in Fig. 30(a)] mounted on the central hub. Starshade biprop thrusters (described below) are used for the TCM. The starshade is initially positioned into a halo orbit close (~100 km) to the telescope, utilizing ground-tracking facilities. During the transit to L2, the petal unfurling system (PLUS) deploys the 28 petals and the inner disc is extended. Upon arrival, injection into the halo orbit (a low-thrust maneuver) is accomplished using the starshade thrusters. Each petal is 16-m long (Table 7) and the inner disc has a radius of 20 m, resulting in the 72-m diameter assembly (Fig. 31). As the disc extends, the petals unfold [they are folded face to face in pairs (see Fig. 30)] and two structural ribs on each

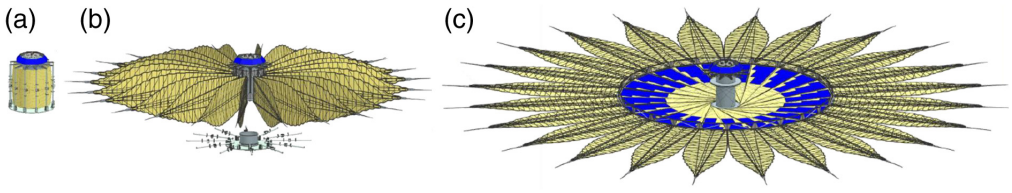

Fig. 30 Starshade deployment sequence (26-petal SRM shade shown). (a) The starshade wrapped around the hub, held captive by PLUS. (b) PLUS, having unfurled the petals, separates from the starshade spacecraft and is discarded. (c) The central disc expands completing the deployment.

Table 7 RM12 Starshade specifications.

Diameter (m)	72
Petal length (m)	16
Number of petals	28
Starshade mass (dry, kg)	9790
Propellant mass (kg)	11,480
Propulsion	Monoprop/SEP
SEP solar array area (m^2)	150

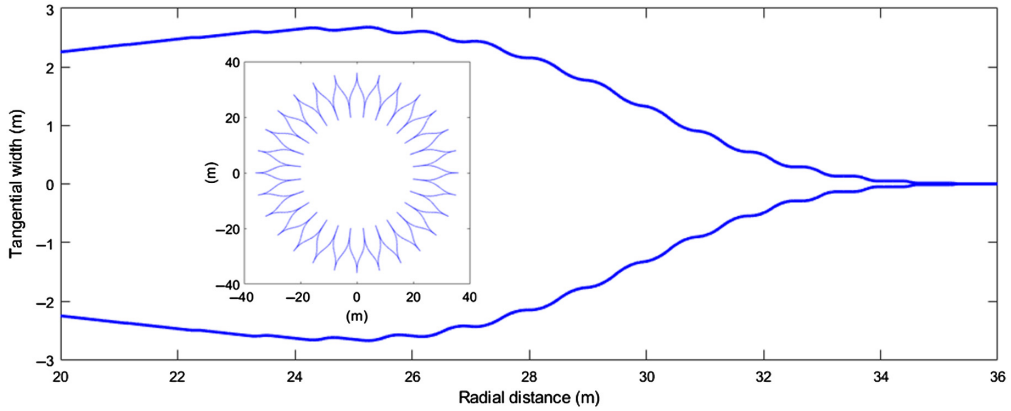

Fig. 31 One petal (the 3 o'clock petal) and inset, the proportions of the starshade. Petal base gaps and tip widths are ~4 mm.

petal fold out and lock into place. These ribs add stiffness by adding an out of plane component to the otherwise planar petal structure. The gaps between the petals at the root and the petal widths at the tip are about 4 mm. The inner disc carries additional flexible solar panels to power the spacecraft bus and its solar electric propulsion (SEP) system. Once deployed, the starshade rotates slowly at 2 deg s^{-1}.

4.3 *Starshade Design and Thermal Performance*

The superior surface (Sun side) is covered in low-emissivity-coated Kapton to reject heat, whereas the inferior surface (telescope side) is covered with high-emissivity black Kapton. These two layers form part of the starshade's OS, which has four additional layers to provide additional thermal isolation and also to protect against micrometeoroid strikes. Figure 32 shows the scheme. The OS is the main source of thermal photons from the starshade and one mechanism, thermal radiation between the layers, dominates. The OS as a whole has black Kapton layers that absorb light and heat, and other layers that reflect it. The net effect of the set of layers is to create a cold inferior surface that minimizes the thermal photon flux from the starshade, permitting observations into the MIR. At starshade angles of 40 deg to the Sun (measured from the normal), the temperature of the inferior surface is expected to be 101 K, while at 80 deg this drops to 69 K. Between these temperatures the photon fluxes at 5 μm observed from the telescope fall from 0.4 to 10^{-6} ph s^{-1} in a 10-nm bandwidth, low enough to permit science observations on exoplanet targets. Thus targets at higher celestial latitudes would be favored, but even those at 40 deg are possible. Figure 33 shows the thermal photon flux from the starshade, observed at the telescope, in terms of AB magnitude. A second, considerably weaker source of thermal radiation is discussed next.

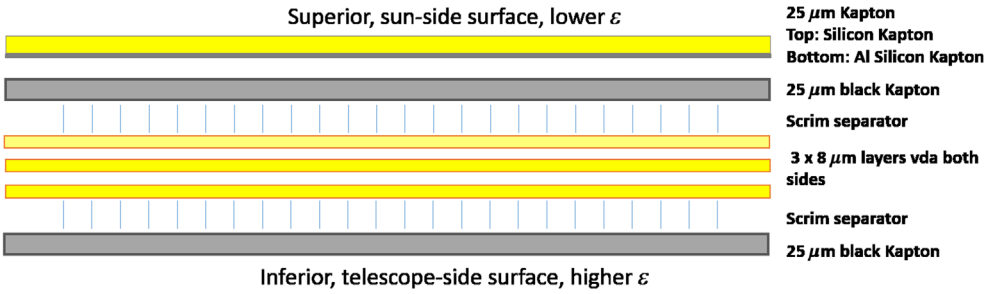

Fig. 32 Multilayer insulation and OS. Low-density scrim separators keep the main elements apart while crinkling is used to separate the thinner layers.

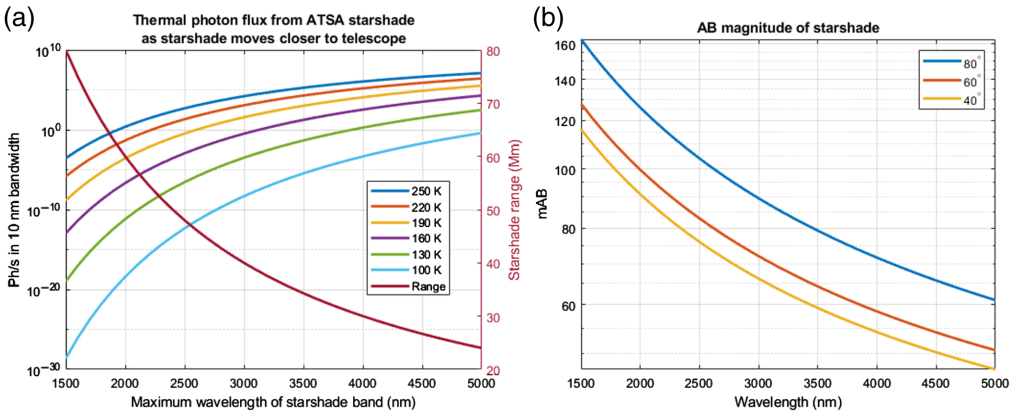

Fig. 33 (a) Thermal photon flux as a function of starshade temperature, illustrating the critical importance of reaching a low temperature for observations at the longest possible wavelengths. Also starshade range as a function of the longest wavelength in the science band. (b) AB magnitude for thermal radiation from the shade at a temperature of 101 K, as a function of observing wavelength and solar incidence angle.

The whole OS assembly forms a barrier to micrometeoroids, which can make very small holes in the exterior surfaces. The majority of micrometeoroids do not penetrate the first layer of the shield. Larger particles are vaporized upon exiting the first layer and fail to penetrate the second. Only the largest particles penetrate the entire assembly of layers. In any case, starshade science observations are tolerant to at least 1 cm^2 of direct through-holes.[61] In addition, sunlight penetrates superficial holes and scatters within the layers, with a portion eventually emerging as an incoherent field from the inferior surface. The radiated amount depends on the hole area (conservatively assumed the same in each layer) and the absorption between each pair of layers, which is high because a large number of reflections is required to find an exit hole, as illustrated in Fig. 34. For small hole areas, the leakage is proportional to the fractional hole area and this leakage decreases geometrically as the number of layers increases. Even for high-reflectivity layers, such as the third through fifth layers, the multiple reflection terms (lower rightmost in the figure) fail to counteract this effect significantly. Thus the ATSA starshade is expected to appear extremely dark (>70 AB magnitude) for transmitted sunlight at working range.

Sunlight scatters from the starshade edges and a small fraction will enter the telescope, creating a background. For this reason, the edges are made very sharp (<1-μm radius), similar to a razor blade (although the angle is obtuse rather than acute). Edge scatter, arising both from diffraction and reflection, has been analyzed and measured[62,63] using prototype edges in the laboratory. Since the edges are sharp, the dominant scatter component is diffracted light. We term as "leading edges" those on which the sunlight impinges directly; the opposite edges we term "trailing edges." The scattered light from the leading edges is strongly S-polarized, while that from the trailing edges is strongly P-polarized (as Sommerfeld[64] showed in 1895). The P-component may

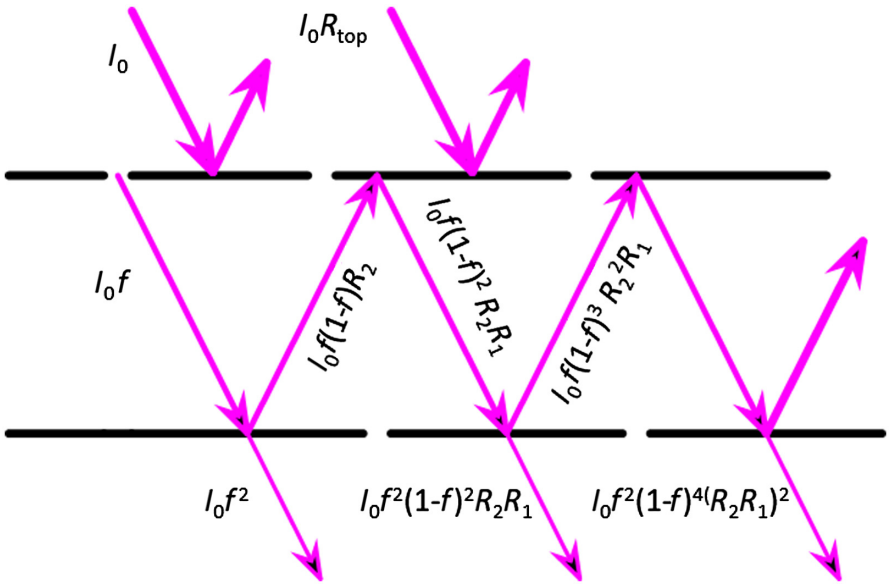

Fig. 34 Effect of holes from micrometeoroids in the starshade. Sunlight impinging on the top layer is largely reflected. Light trapped between the layers undergoes multiple reflections until it is either absorbed or transmitted through the lower layer (or back up to the layer above). Despite the high probability of multiple reflections, little light makes it through because of absorption.

therefore be substantially removed by designing the petals to shade the trailing edges. At visible wavelengths, edge scatter is the strongest contributor to the background (∼25 mag), but it may be suppressed by applying coatings to the edges, a technology that is now being developed[65] and is showing suppression ≫5 magnitudes. At longer wavelengths, the diffracted intensity will increase linearly with increasing wavelength. Additional analysis, coating development, and indeed testing will be needed to characterize starshade edge requirements for operation at these longer wavelengths.

4.4 *Starshade Bus*

The starshade utilizes a conventional spacecraft bus (see Fig. 35) with the usual functions. The starshade hub structure resembles a large cable spool and is composed of a cylinder with flanges at each end. The cylinder is a strong honeycomb composite structure 1.8-m-in diameter and contains the bus, comprising the principal spacecraft systems as well as the hydrazine and xenon propellants. The starshade bus includes the following.

1. Bipropellant thrusters for station-keeping and attitude maneuvers, the SEP microthrusters used during transition maneuvers and associated fuel and propellant tanks.

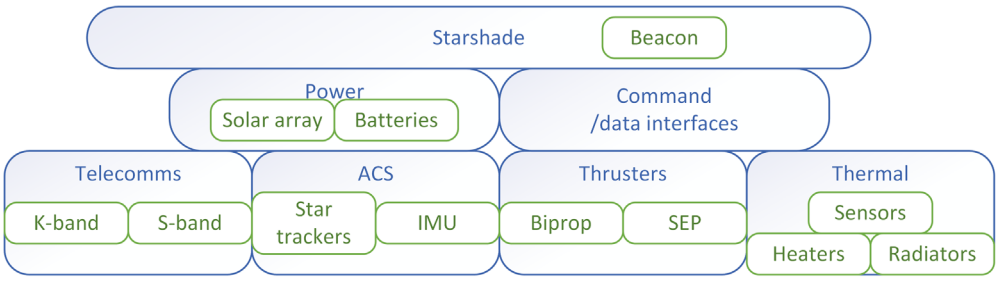

Fig. 35 The principal components of the starshade spacecraft. K-band and S-band antennas allow communication with the ground and the telescope spacecraft, respectively, while the beacon facilitates starshade acquisition after transit maneuvers.

2. The ACS, based on a pair of externally mounted star trackers, laser gyros, and accelerometers.
3. The power system that conditions and directs power from the solar arrays to the ACS, heaters, and other systems including the spacecraft electronics.
4. The power system that conditions and directs power from the high-voltage solar arrays to the SEP system.
5. *The communications systems*. One transmits and receives data, commands, and telemetry to and from the ground. The second communicates with the telescope via the S-band link to obtain modal commands and formation-flying position data.
6. The TCS with radiators mounted on the superior hub surface.
7. The flight computer for CDH.

The starshade's hub structure attaches directly to the LVA ring via a payload interface plate (PIP) mounted on the lower flange. In turn, the LVA is mounted to the launch vehicle's PAF, from which it separates after launch. Starshade launch loads are carried through the walls of the central spool-like cylinder section. The propellant tanks are positioned on the inside surface of the spool's lower flange, providing a direct load path to the LVA. Two lightweight flanges extend to and retain the starshade PLUS interface structure (a combined deployment and constraint device—see description below), which in turn retains the furled petals. Just inside the petals, the disc's rigid ring truss structure is folded concertina-fashion and within that ring, the OS forming the circular core of the starshade is folded in a spiralling origami "flasher[66]" pattern. Flexible solar panels providing power to the SEP system are mounted to the superior surface of part of this OS. For deployment, after rotation of the PLUS, which releases the petals folded face to face in pairs, only one additional mechanism—a cable drawn in by a motor—is required to unfurl the starshade, extending the truss and unfolding the petals. Cables between the truss and the hub (acting like the spokes of a bicycle wheel) become tensioned during the final stages of deployment and stiffen the entire structure.

The bus equipment is mounted within the hub on the sandwich-structured composite of aluminum face sheets and aluminum honeycomb that form the upper and lower flanges. On the upper flange, structures and brackets support fixed low-voltage solar panels and electronics equipment. Propellant tanks are mounted on the lower flange, but thermally isolated to prevent a "hot spot" underneath the starshade. Excess heat from the warm propellant tanks is radiated at the cylinder sides, i.e., above the superior surface of the starshade.

The thermal subsystem maintains the bus equipment at correct flight temperatures. Approximately 150-W of heater power is required to maintain the propellant temperatures during normal operations; 30 W is required during launch, downlink, and safe modes. Thermistors measure temperatures and strip heaters provide heat where needed. The subsystem also includes MLI blankets to isolate the lower flange and variable-conductance heat pipes to bring waste heat to the radiator. Aided by the slow rotation that distributes the solar thermal load evenly, the starshade petals and much of the inner OS are thermally stable, with only small residual fluctuations from the rotation.

4.4.1 *Starshade bus propulsion systems*

The starshade dry and wet masses are estimated to be 9790 and 20,600 kg, respectively, with margin. Two propulsion systems are used: one for transits between telescope-star sight lines (TSSLs); the SEP, and a second conventional bipropellant system for formation-flying station keeping, TCMs, and slewing. In operation, the starshade moves under the influence of gravity and solar radiation pressure (SRP), which varies according to orbital position and orientation with respect to the Sun. To provide an even distribution of heat and maintain starshade shape under thermal loading, the starshade rotates about the normal to the plane of the shade once every 3 min. The center of the starshade must be maintained within a 2-m diameter circle perpendicular to the line of sight to the telescope. A simple ballistic trajectory can be achieved within that circle by firing thrusters when the starshade reaches the edge of the control region. The process is akin to using a tennis racket to repeatedly bounce a tennis ball upward to a certain height. The time between thruster firings is ~ 10 min.

The chemical propulsion system uses twelve 62 N bipropellant thrusters (e.g., RocketDyne AJ10-220 reaction control thruster) with an $I_{sp} \geq 268$ s, providing sufficient redundant control to meet TCM and formation flight requirements. A biprop system is preferred over monoprop for the starshade because the higher I_{sp} gives a longer period between refuelings. These thrusters are flight-proven for more than 65,000 starts. Formation flying demands a short-burn time at the edge of the circle and these thrusters allow a 9-s burn. With a 1-s pause after firing for thruster plumes to leave the FOV of the EXPRESS instrument, this yields a raw observation efficiency of ≥98%.

The SEP thrusters (e.g., RocketDyne Advanced Electric Propulsion System) provide up to 600 mN of thrust each using xenon propellant with an I_{sp} of 2800 s. The SEP engines are gimbaled and arranged around the starshade bus, enabling translation of the starshade in any direction while allowing the starshade's superior surface to be illuminated by the Sun to provide power. Two SEP engines are required to achieve nominal thrust for retargeting. The mean transit angle is 22 deg and can be crossed in about 12 days. During retargeting maneuvers, the starshade can adopt an attitude normal to the Sun, providing maximum solar power to the thrusters (13 kW each). To the set of four, an additional set of SEP thrusters is included to provide redundancy.

The fuel load is scaled to meet a 5-year mission duration. Assuming a 9790-kg dry mass, some 5540 kg of bipropellant and 5270 kg of xenon will yield at least 100 targeted starshade observations. Both the xenon tanks and bipropellant tanks can be refilled robotically via NASA cooperative servicing valves, thus providing for an extended mission.

4.4.2 *Starshade bus power*

Two separate power systems are carried with their own solar arrays, one running at 600 V to power the SEP system, the other running at 28 V to power the usual bus functions. Immediately after launch, the starshade bus is powered from its battery system, sized for 3 h of operation down to 70% capacity. The superior surfaces of the central part of the starshade hub carry a fixed set of solar arrays providing power to the bus during cruise to L2 (with the top of the starshade hub turned to face the Sun) and for normal starshade operations, such as formation flight.

The deployable OS carries high-voltage, flexible solar arrays that power the SEP system. With a pair of SEP thrusters running at any given time during transition (travel of the starshade across the sky between target stars) ∼26 kW is required from this array. With conservative assumptions (29% efficiency, tilt 60 deg, 15% contingency), the minimum required flexible solar-array area is ∼150 m^2, easily accommodated within ∼12% of the area of the 1260-m^2 inner disc.

Table 8 shows the power equipment list (PEL) for the starshade flight system. For the low-voltage bus, the highest power of just more than 1 kW is required during TCMs or L2 insertion. Depending on the orientation of the starshade during the maneuver, this can be supplied by the fixed solar array, the batteries, or a combination of the two. Other operational modes require less power and there is consequently a large power margin in these cases. For example, the low-voltage array meets bus power requirements both before starshade deployment and during formation flight with Sun angles between 40 deg and 83 deg.

During retargeting operations, the electric propulsion system is employed. The flexible solar-array cells are strung together to form a 33.3-kW, high-voltage array, offering margin to degradation and Sun angle. The starshade requires an assembly of 38 lithium ion batteries with 2260 Ah capacity at 3 V to power the bus for up to 3 h postlaunch with 30% depletion.

4.5 *Formation Flying*

Under the influence of radiation pressure and gravity gradients, the starshade is continuously accelerated, but during science observations it must be maintained within a circular area of diameter 2 m, centered on the line of sight to the star. (The circle size is invariant with respect to starshade range.) This is done by periodically (∼every 10 min) and briefly (∼10 s) firing thrusters to project the starshade back up to the top of the control area and letting it fall back in a ballistic trajectory. During thruster firing, the starshade science instrument will have to be protected from the relatively bright thruster plumes, which are of apparent magnitude about 13.

Table 8 Starshade PEL and summary budget.

	Subsystem power during mission phase (W)						
Subsystem	Launch	Cruise	SEL2 insertion	Transition	Starshade science	Downlink	Safe
ACS	35	10	50	50	80	50	40
CDH	45	45	45	45	45	45	45
Propulsion: Biprop	30	3	260	30	30	3	30
Propulsion: SEP	0	0	0	26,600	0	0	0
Telecom	75	75	75	75	65	75	75
Thermal	180	210	210	180	210	210	210
Power	100	100	110	1400	110	110	110
Subtotal	**470**	**440**	**750**	**28,380**	**540**	**490**	**510**
Contingency power	200	190	320	3430	230	210	210
Distribution losses	13	13	20	410	20	14	14
Total	**680**	**640**	**1090**	**32,220**	**790**	**710**	**730**

This is achieved by [as in the starshade Rendezvous Mission (SRM) concept] briefly switching the detectors to a fast readout mode during thruster firings. This is sufficient to prevent saturation and the formation of a persistent image. The other instruments are sufficiently far off-axis from EXPRESS that they could likely continue to operate undisturbed since thruster plumes are unlikely to pass through their fields of view. Exceptions may occur in cases where the plume passes through the FOV and the integration times are long. By keeping the thruster firing times short, the observation time is maximized and typically there will be several minutes of free flight between thruster firings.

To maintain the starshade on the line of sight, the starshade shadow is observed at wavelengths either shorter than or longer than the science band. Since the starshade is of the numerically optimized type (rather than the hyperGaussian[67]), it blocks starlight very efficiently across the science band and leaks light at either end, as shown in Fig. 12. Thus when the starshade is operating in the near-IR band (750 to 2500 nm), a signal can be obtained at $\lambda \approx 600$ nm or at $\lambda > 4000$ nm). This signal consists of a shadow of the starshade, observable at the telescope entrance aperture. The principal feature is a residual spot of Arago, having a diameter approximately $d_A = r/(2F)$, with the starshade radius 36 m and the Fresnel number typically ~8 at the longest wavelength and therefore ~32 at the ≈600 nm leakage wavelength. The spot would be $\lesssim$0.6 m wide and 500 times fainter than the target star in a $\lesssim$100 nm bandwidth, quite sufficient for detection. By imaging the telescope entrance pupil onto a camera, the starshade position can be followed[68,69] and the large photon flux allows determination of position to $\ll$0.6 m. As the starshade approaches the edge of the 1-m radius control area, thruster firing instructions are sent to it via an S-band radio link. After the thruster firing, in the optimal control scheme,[70] the starshade is on a ballistic trajectory heading toward the opposite edge of the control area with sufficient momentum to just avoid exiting, after which it falls back and the process repeats.

Formation flight holds a number of challenges. First, the telescope must be kept within the high-contrast shadow region generated by the starshade, accomplished by actively restraining the starshade location so that it remains on the TSSL. Second, the telescope must remain pointed at the target star for observation times that may be as long as weeks. Third, loss of the starshade from the TSSL may occasionally occur, so that a recovery process is needed. Detailed analyses of the formation flying problem with mission-specific assumptions were made[70,71] for the now-cancelled Nancy Grace Roman Space Telescope-starshade Rendezvous Mission (NGRST/SRM) that are relevant here. The concept defined two circular limits within the 2-m diameter design

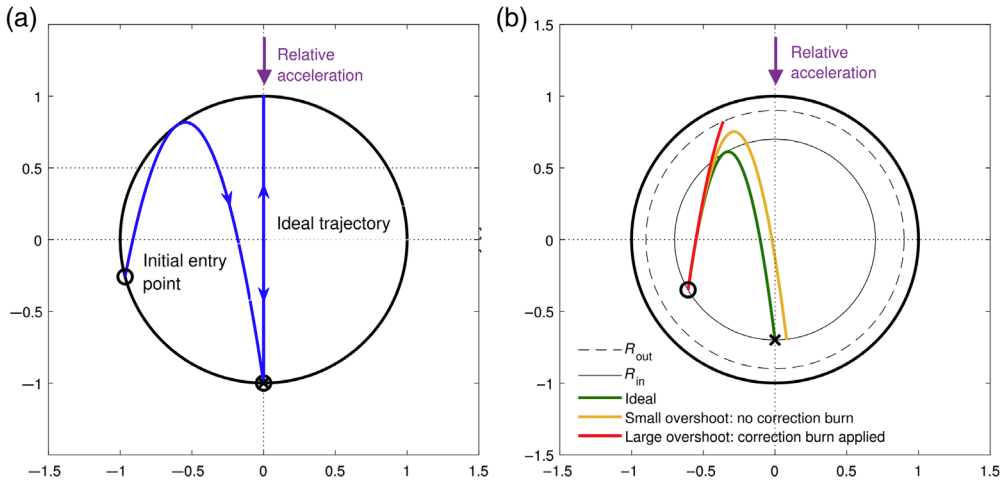

Fig. 36 (a) Initial path of the starshade in the 2-m circle and the ideal final path against the local SRP and gravitational acceleration. (b) Trigger boundaries for the control system.

starshade flight region (SFR) [see Fig. 36(b)]. The outer limit R_{out} is a "do not cross" limit that triggers a compensating thruster firing to move the starshade back toward the center of the SFR. To allow for delays, the radius of this limit is <1 m. The inner limit R_{in} has an even smaller radius that when crossed triggers a thruster firing intended to move the starshade back across SFR to the opposite inner limit. The direction of thrust is tailored to move the starshade back to a position that produces the maximum possible time between thruster firings, that is, the point on the inner limit on the radius pointing in the direction of the starshade acceleration, as shown in Fig. 36(a). The positions of these limits are set based on simulations of the space environment and a model of the formation flying sensor.[68] The control scheme developed for NGRST/SRM has been tested in a realistic model using Monte Carlo simulations and shown to result in thruster firing intervals ~30% shorter than perfect control would allow. Recent analysis[72] shows significant increases in thruster firing intervals for particular locations of target stars with respect to the Sun–Earth axis, so there are nuances that have yet to be incorporated into DRM models that may result in reductions in the mass of propellant needed for formation flying.

The formation flying sensor must provide both the starshade location within the SFR and the pointing error. This pointing error is a combination of telescope pointing error (mainly FGS error) and the pointing direction of the starshade instrument channels. The angle between these two systems will evolve over time as the telescope temperature changes. For the 6-m telescope aperture, the point spread function (PSF) full-width half-maximum (FWHM) is 20.6 mas at a wavelength of 600 nm. Constraining the rms pointing error to be 2 mas, the light within the science core (a circle at the FWHM containing 50% of the light) will be on average 90% of the maximum. Increasing the pointing error to 3 mas rms causes the light in the core to fall to 80% of maximum, so it is important to constrain the pointing error. There are two ways of doing this: internal laser metrology to detect the tilt difference between the FGS and the starshade channel, or direct detection within the starshade channel. For science observations on MOUS or MOVIS, the camera has a sufficient FOV to contain bright stars that can be used to maintain pointing on the target star, but the starshade camera has an FOV of only 8 mas (Table 9), so that field stars will be few, if any. In this case, using direct detection, pointing must be maintained using guide light from the target star. A tilt sensor could be based on the Zernike wavefront sensor concept.[73] The sensor produces an image of the residual Airy disk at the center of the starshade shadow, slightly modified by the tilt of the telescope. A new sensor and analysis method[74] developed from that proposed by Bottom et al.[69] is capable of detecting the starshade location with respect to the TSSL, together with the telescope tilt. Simulations made for NGRST/SRM show pointing measurement accuracy of ~3.1 mas and position measurement accuracy of ~40 mm on fifth magnitude stars. With the larger aperture of ATSA, even higher accuracy would be expected.

Over prolonged observation times, Monte Carlo simulations[70] for NGRST with SRM have demonstrated robust formation flying of the starshade for periods of a week or so and similar

Table 9 Key features of the instruments.

Instrument	λ (nm)	FOV[a] (arc sec)	Pixel pitch (μm)	f/D	Filters	Mechanisms
MOUS	115 to 315	180×180	15	<65	7 imaging	Insertable MSA grating wheel (see Table 10), filter wheel
MOVIS						
UV	320 to 450	180×180	12	41	2 wheels $\times$ 7	Filter wheel
Vis	450 to 950	180×180	12	41	12 wheels $\times$ 5	Insertable MSA at shared F33 focus, filter wheels in Vis and NIR
NIR	950 to 2400	180×180	10	20	3 wheels $\times$ 7	As above
MIR	2400 to 5000	180×180	10	10	1 wheel $\times$ 7	Filter wheel
Express						
UV imaging	200 to 450	7.0	13	80	None	Pupil-imaging lens and $R = 5$ prism in same mechanism
VIS imaging	450 to 1000	7.9	12	71	None	None
VIS IFS	450 to 1000	1.1×1.1	12	1230 at lenslet	None	Switch mirror
				6.0 at FPA		$R = 140$
NIR imaging	975 to 2400	7.9	12	51	None	Pupil-imaging lens
NIR IFS	975 to 2400	1.8×1.8	12	369 at lenslet	None	Switch mirror
				3.36 at FPA		$R = 40$
MIR imaging	2400 to 5000	7.9	10	15	None	None
Guiders A and B	500 to 900	0.285×0.285	13	48	None	Scan mirror
		FOR = 186				

[a]FOV values with a single number indicate circular diameter. FOR denotes FOR.

qualities are expected for ATSA. These simulations showed very few correction burns: around the 400-s mark on the horizontal axis of Fig. 37. These burns occur when the trajectory reaches the outer trigger boundary shown in Fig. 36. In the extreme case of loss of the formation, an event that did not occur in the simulation, the starshade position can be recovered by switching to detection of the beacon on the starshade science camera and following the normal starshade acquisition procedure.

4.6 *Transitions*

A starshade imposes some restrictions on observations, because switching from one target to another requires not only slewing the telescope, but also moving the starshade across the sky (a process termed "transition") to a position between the telescope and the new target, a journey that could take days or weeks. Constraints on the angle made to the starshade by the Sun create

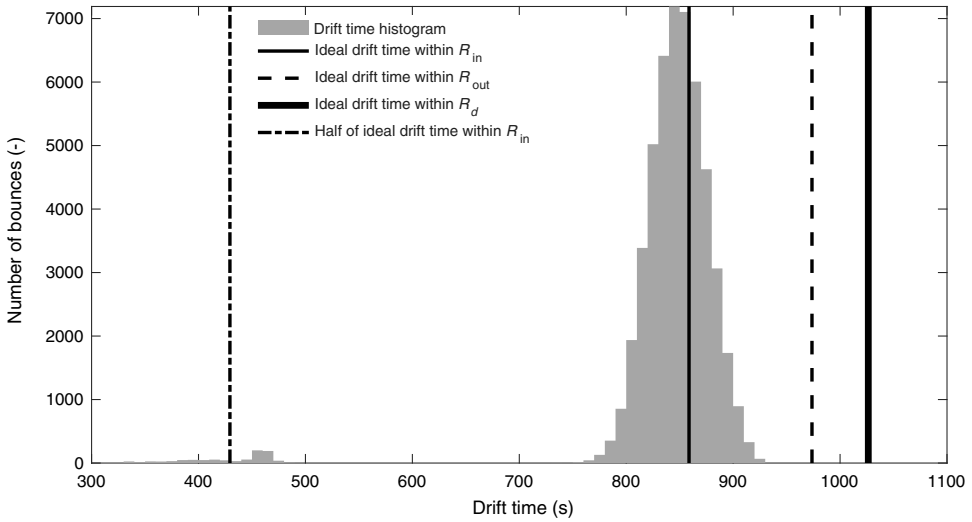

Fig. 37 Results of a Monte Carlo simulation of formation flying for NGRST/SRM with a realistic (but not yet optimized) sensor and control model. The time between thruster firings is shown on the horizontal axis and the histogram shows the number of bounces (i.e., thruster firings). The typical period between firings is 850 s. To the left correction, burns can be seen at about the 400-s mark. This figure adopted with permission from Ref. 70.

an annulus from 40 deg to 83 deg, in which stars are observable. (These angles are conventionally chosen—the smaller angle is set by tolerance for sunlight diffracted from the starshade edges and could be adjusted, whereas the larger angle could be set to 90 deg or more by allowing the starshade to tilt with respect to the starshade-telescope line of sight,[75] allowing a little more flexibility in observations.) Planning the observations requires an optimization of the traveling salesman problem (TSP) to balance fuel consumption, transit time, and target potential. The Exoplanet Open-Source Imaging Mission Simulator (EXOSIMS)[76] optimizes the TSP for starshade missions by scheduling observations that are dynamically responsive to discoveries during the simulated mission.[72,77–79] EXOSIMS draws exoplanets from probability distributions of planet properties. The planets are synthesized around stars within 30 pc, and an observing sequence is dynamically simulated. This occurs on a Monte Carlo ensemble of hundreds of synthetic universes. Figure 38 shows one example universe and its observations and starshade path more than 5 years.

Yield results are discussed in detail in Sec. 8, for several different scenarios. In this section, we focus on the operational aspects of observing with a starshade, which are more or less independent of the scenario. At the outset, it is worth pointing out that a great deal of effort has gone into the determination of yield over the last few years.[80–82] Although uncertainties are still large, for telescopes, instruments, and starshades that can be considered credible over the next decades, the number of available rocky habitable-zone planets will be in the tens and not hundreds.

In the starshade-only observing scenario, a blind-search survey is conducted in imaging mode. Once a planet is detected, the starshade remains on the target for spectral characterization. Revisit observations in imaging mode are made at later epochs to determine if the characterized exoplanets are in the HZ. The starshade target list therefore grows throughout the mission and the final yield is dependent on the efficiency and effectiveness of the blind search. The blind search and subsequent orbit determinations are made during a series of starshade maneuvers (transitions). The architecture presented in this paper took an average of 70 transitions with average duration 22 days during a 5-year mission.

Sufficient xenon propellant is carried to provide ~100 SEP thruster firings (before refueling) to reach starshade velocities up to 50 $\mathrm{m\,s^{-1}}$ in ~7 days, followed by an equally long deceleration phase. In survey mode, the starshade would typically spend only a day or so at each target, whereas in the spectroscopy mode, the observation might last weeks. Additional trade studies of observing strategies and starshade architectures would help find the lightest and most agile

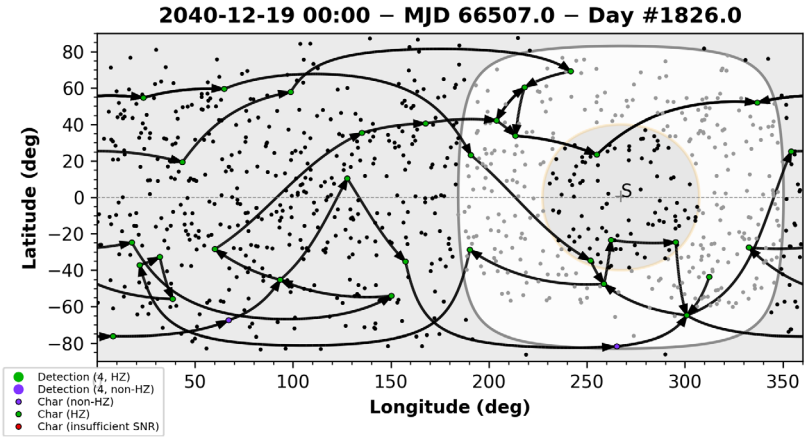

Fig. 38 Example of a 5-year observing program with perfect prior knowledge. Synthetic planets, from a broad list of ∼950 potential target stars, are "observed" and considered detected or characterized if the goal SNR is reached. Green points mark observed rocky planets in the HZ, purple other observed planets, including rocky planets, not in the HZ. Gray points mark unobserved stars. Spectral characterizations with the starshade are distinguished by a black edge around the circle marker and are at the tip of a black slew arrow. The white annulus is the region of observability possible for the starshade on day 1826. As the year progresses, the longitude of the annulus moves. The central gray circle with yellow border is the solar "keep out" zone of the telescope. The position of the Sun is labeled "S" and denoted by a gray cross.

starshade configuration that will meet mission requirements. In particular, time-consuming surveys by ATSA would not be required if precursor missions and ground surveys reveal a suitable number of targets with their orbital parameters, in which case the bulk of the mission time would be devoted to spectroscopy and the survey phase minimized. One particular such precursor case is evaluated in Sec. 8, showing that the yield rate accelerates and that prior knowledge has the most significant impact on yield for the starshade-only architecture.

Transition would be initiated after the completion of observations on a science target. Released from the formation, the telescope would switch to another science mode and slew to another target, and the starshade would initiate its transition. With the set of SEP thrusters, the starshade can move in any direction. Using the biprop thrusters, the starshade's rotation is stopped for the transition and restarted at the required orientation at the next target. Over the duration of the mission, this uses approximately half of the biprop fuel. Continuous thrusting is used throughout the transit, with the deceleration phase immediately following the acceleration phase. Navigation is by dead reckoning; that is, the starshade's location is only approximately known upon arrival at the new TSSL and the starshade would then be located by telescope observations. The final location of the starshade depends on a number of parameters[83]—the starshade mass, which varies as fuel and propellant are used, the direction of thrust during acceleration and deceleration, gravity and SRP vectors, and initial positions of the starshade and telescope. Nano-g accelerometers with 2 ng $\mathrm{Hz}^{-1/2}$ noise levels have been developed[84] and can be used to estimate the starshade trajectory under the thrusters. Starshade mass, gravity, and SRP effects can be estimated from the formation flying data at the previous target, plus a knowledge of the telescope and starshade's position in space relative to Earth, Sun, and Moon, so that accelerations and positions can be continuously estimated. Anticipating the starshade's arrival at the new target star, the telescope turns to observe the target and uses the wide field camera MOVIS to locate the starshade beacon.

Assuming typical 22 deg transitions, for the starshade to fall within the FOV of MOVIS requires trajectory direction accuracy of better than 0°.14. Assuming the starshade accelerates under the thrust of two SEP thrusters, the acceleration is ∼8 μg and with the noise from just one accelerometer, the rms trajectory error is $<0^{\circ}.02$. If this were the only error, then taking into account the same error in the measured acceleration, the starshade will arrive within an approximately spherical region with rms radius of $\sim 1'$ seen from the telescope. Various factors perturb the trajectory—for example, free fall under gravity is not detected by the accelerometers—but

these factors and the influence of radiation pressure (<1 μg) are calculable with a knowledge of the orbital positions of the telescope and starshade. Flinois et al.[83] found that the dominant contributors to final position uncertainty are the initial velocity uncertainty from the retargeting burn and the SRP, owing to the large area of the starshade and its variable presentation angle to the Sun. For shorter cruise (transition) periods of 7 days, the error in the final position is <5%, using a conservative model. Note that Flinois's analysis considered conventional thrusters rather than SEP: the error in the estimated trajectory is likely to be different for ATSA and further analysis is required. In the absence of that we assume that the starshade is likely to be found within the FOV of MOVIS ($3' \times 3'$), but if necessary a raster search in a $10'$ region using the telescope's 4 N monoprop thrusters will suffice for detection.

Once the beacon is detected, the starshade is guided toward the line of sight to the target star via data sent from the telescope on the S-band link, while pointing adjustments are made to the telescope as necessary. Ultimately, with the star centered on the focal plane of MOVIS, the starshade comes within the FOV of the chosen starshade guide camera channel ($\geq 7''$ diameter) and the telescope slews to center the starshade instrument FOV on the target star, thus capturing the starshade beacon on the starshade instrument cameras.

5 Telescope Optical Design

Various considerations bear on the telescope optical design. The optical requirements for the OTA are as follows.

1. A 6-m-diameter aperture.
2. A segmented, active primary mirror.
3. As few segments as possible consistent with current development status, i.e., of order 1 to 1.5 m in size.
4. Minimized segment gaps.
5. A moderate FOV to accommodate several instruments with independent views on-sky.
6. A primary-secondary mirror separation set by practical factors, such as launch vehicle shroud dimensions and mass capabilities.
7. Maximized optical throughput across the range 100 to 5000 nm.

The radius of curvature of the primary mirror is about 13.1 m ($f/1.09$) and it is separated by 6 m from the secondary mirror. The FOV requirement drove selection of a configuration based on Ritchey–Chrétien design principles. The total telescope FOV is about $0^{\circ}.20 \times 0^{\circ}.31$ ($12' \times 18'.6$) and is sampled by the smaller FOVs of the three instruments and the two guide channels. Some aspects of the optical configuration are dictated by the performance goals of the UV instrument. To minimize the number of mirrors needed for MOUS (reflection losses are a concern at shorter wavelengths), a trade-off was made between the aspheric shapes of the primary and secondary mirrors, and the tilt, decenter, and shape of the secondary mirror. This resulted in a best compromise between performance at the microshutter array (MSA) and at the output collimated beam, achieving the performance goals of 30 nm RMS WFE at the MSA and diffraction-limited performance at 400 nm.

6 Instruments

6.1 *Overview*

The two main aims of the optical instrument designs are to maximize optical throughput without compromising diffraction-limited performance and to bring certain detector surfaces out as near as possible to the side of the AMS structure open to space to facilitate passive detector cooling. This has the benefit of eliminating the need for heat pumps and associated vibration and reducing complexity. Two instruments provide capabilities for general astronomy and astrophysical investigations: the MOUS (covering 115 to 315 nm) and the MOVIS (covering 320 to 5000 nm).

Both instruments can also function as cameras. The other instrument, EXPRESS, is specialized for exoplanet and disc studies; the starshade instrument (EXPRESS) functions in concert with the starshade spacecraft and is particularly suited for spectroscopy. Specifically:

- MOUS has 20 diffraction-grating modes and 1 imaging mode. All modes use the same focal plane. A rotating mechanism inserts each grating into the path. For imaging studies, a filter wheel inserts one of seven available filters into the imaging mode beam. The instrument includes an MSA at the OTA's internal focus, which follows the telescope secondary.
- MOVIS has four channels: near-ultraviolet, visible, near-infrared (NIR), and MIR. Each channel has its own focal plane, so there are four MOVIS focal planes in total. The visible and NIR channels share a removable MSA.
- EXPRESS has four channels: ultraviolet, visible, NIR, and MIR. All four have imaging modes. In the visible and NIR channels, there is a flip-in mirror that diverts the light to an integral field spectrometer (IFS). Between the imaging and IFS channels, there is a total of six EXPRESS focal planes. Two additional operating modes in the EXPRESS UV imaging path are pupil imaging and coarse dispersion. In the NIR imaging path, there is an additional starshade guidance operating mode.

In addition, there is a fine guidance instrument that has two optically identical channels (though folded differently) and focal planes. Other instrument types that are or will be directly useful for exoplanet studies are in development and might be applied to the segmented telescope design. Some of the options are discussed below (Sec. 6.6).

The optical system views the sky through six separate fields, as shown in Fig. 39. The optical configuration of each channel is either a three or four-mirror afocal telescope with of order 140× angular magnification (varying by channel) followed by reimaging optics. The afocal telescope has a common primary and secondary in all channels, followed by an optical switchyard consisting of fold mirrors that divert the light to the different channels and separate subsequent reimaging optics. Figure 40 shows the optical layout of the full instrument system behind the AMS (instrument and switchyard enclosures are not shown). The optical and mechanical designs were developed together to ensure practical packaging and clearances within the available space. Table 9 summarizes key features and current modeling assumptions of all the instruments.

6.2 *Multiobject Ultraviolet Spectrograph*

MOUS is designed for high-resolution spectroscopy from 115 to 315 nm. Its capabilities include multiobject grating spectroscopy, UV imaging, and spectroscopy using bandpass filters.

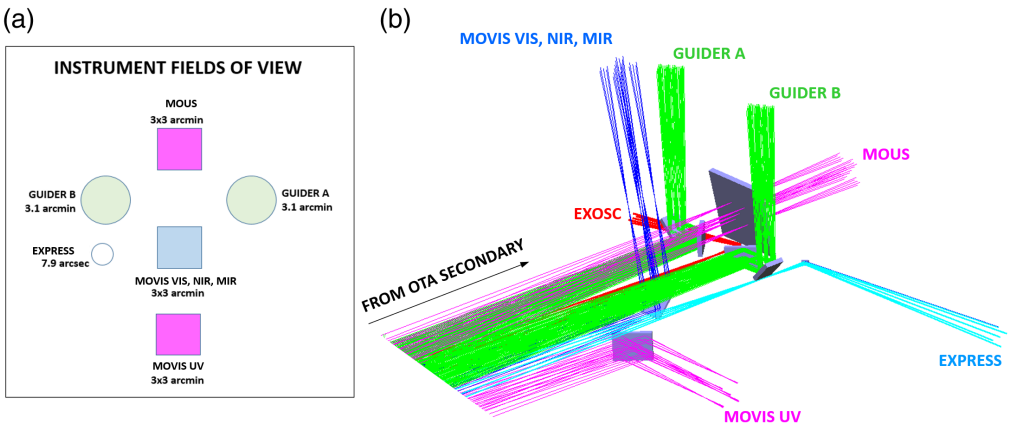

Fig. 39 (a) Arrangement of the instrument fields of view (sizes not shown to scale). The MOVIS near-UV channel views a different field than the other MOVIS channels. Otherwise, the instruments split the wavelength channels internally. (b) Optical switchyard from which light is directed to the instruments. Optical components are mounted within an enclosure attached to the AMS with bipods.

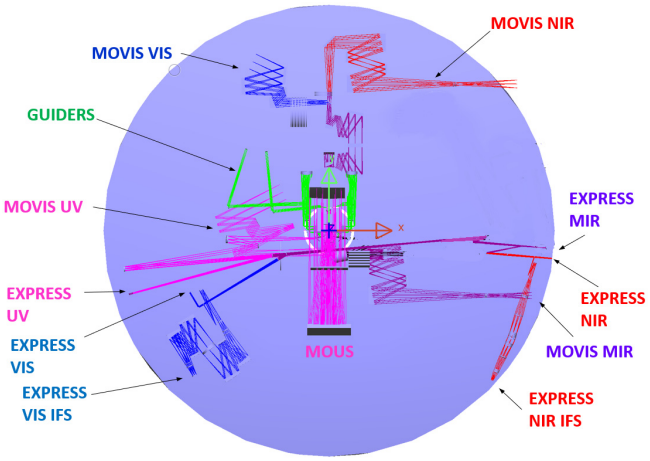

Fig. 40 View from behind the AMS showing the optical layout. To the right, NIR and MIR focal planes are brought out as close as possible to the cool side of the bus so as to maximize the heat flow to the exterior radiators. To the left, the remaining focal planes have less stringent cooling requirements and can be cooled with longer conductors. In places where optical paths appear to cross, the components are at different distances from the AMS. Instrument enclosures are not shown but can be seen in Fig. 25.

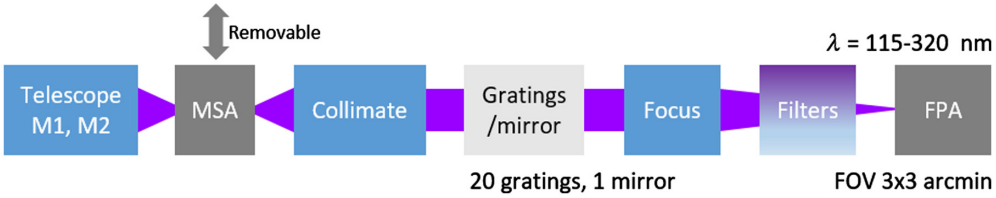

Fig. 41 Schematic of MOUS showing the principal components.

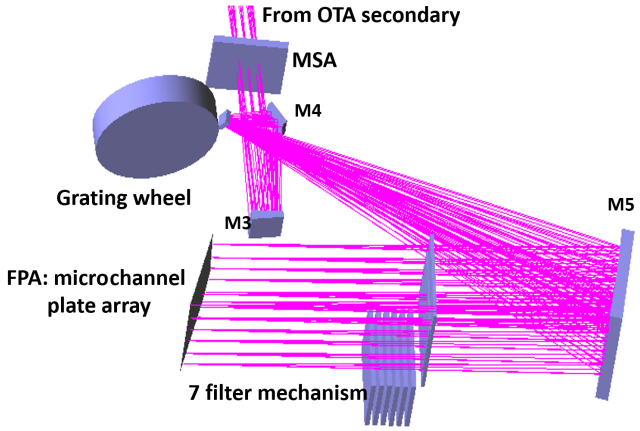

Fig. 42 Optomechanical layout of MOUS showing the beam entering from the telescope secondary, the tertiary, and quaternary mirrors and the grating wheel. Optionally, optical filters can be placed into the beam before the focal plane.

We show thin transmissive filters of base material LiF, which can operate to below 115 nm,[85] but an alternative would be plane reflective filters and a consequent fold path, depending on analyses and throughput trade-offs. A schematic diagram is shown in Fig. 41 and the corresponding optical layout is shown in Fig. 42. To maximize throughput, the primary and secondary mirrors (in fact, all the mirrors in MOUS's path) are coated with aluminum, protected by a layer of MgF_2. Detection of light across this range would be accomplished using a large

Table 10 MOUS: MSA and grating resolutions.

FOV	$3' \times 3'$	
Detector	4×5 MCP array, 8.4 mas pores	
MSA	840×420 apertures, 107×214 mas each	
Gratings	$10 \times R = 60{,}000$, 10% bandwidth	
	$4 \times R = 24{,}000$, 25%	
	$2 \times R = 12{,}000$, 49%	
	$1 \times R = 6000$, 92%	
	$1 \times R = 3000$, 92%	
	$1 \times R = 1000$, 92%	
	$1 \times R = 500$, 92%	
Imager	Plane mirror	115 to 315 nm
Filters	Seven bandpass filters	Various bands

($>36{,}000 \times 26{,}000$ pore) microchannel plate (MCP) detector, which is a sensitive low-noise electron-multiplying device. Its GaN photocathode, deposited using the atomic layer deposition technique, yields best performance with quantum efficiency near 80% at the shortest wavelengths.[86] Selection of objects within the FOV is made using an MSA—a large array of individually commanded shutters.

MOUS can be used simply as a camera and optionally, filters can be inserted for use in imaging mode. It also contains a number of gratings covering the ranges shown in Table 10, with resolution up to 60,000. MOUS accepts light from a field centered 0°.074 off the primary mirror axis, encompassing an FOV of $3' \times 3'$. A removable MSA can be positioned where the primary–secondary combination forms an $f/16$ Cassegrain focus, enabling objects in selected areas of the FOV to be included or excluded. The MSA consists of a set of four units, closely butted together, of a version of the planned next-generation (NexGen) electrostatically actuated type,[87] with 420×210 apertures each and 840×420 apertures total. Here we are assuming a custom version, slightly larger than the proposed CETUS[88] NexGen version (which is 365×171). Apertures will be 180 μm $\times$ 80 μm in size on 200 μm $\times$ 100 μm pitch; each component has about 40% more operating area than the MSAs designed for NIRSpec[89] (365×171 each of four units) but is more compact in overall form. The reason for using a set of four smaller arrays is to make a best-fit match to the curved Cassegrain focus; each quadrant of the MSA will be a separate flat array, slightly tilted to match the best-fit focal surface. The maximum diffracted PSF size (50% encircled energy diameter) at the MSA is 17 μm at 300 nm wavelength.

Table 10 shows the main features of the instrument. Following the MSA, tertiary, and quaternary mirrors create a collimated beam at 162× angular magnification from the primary mirror, with a pupil being formed at the grating (or plane mirror) carried by the grating wheel. The collimated light reflected from the grating is focused onto a curved FPA detector by a fifth mirror.

Figure 43(e) shows the Strehl ratio for the UVS imager. The imperfections of real optics are omitted. These optics would be highly polished and accurately finished to minimize additional WFE. We anticipate that performance would be further improved by additional design work.

6.3 *Multiobject Visible-Infrared Spectrograph*

MOVIS is a general-purpose spectrograph and camera providing imaging and spectroscopy modes over four bands from the near-ultraviolet (320 nm) to the MIR (5 μm). The principal components are illustrated in Fig. 44. The three channels for visible light, NIR, and MIR

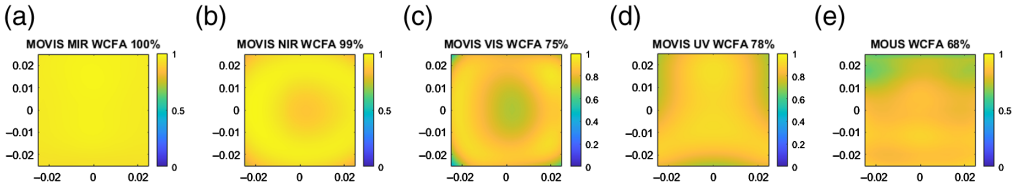

Fig. 43 Strehl ratio across the fields of view (axes scaled in deg) for MOVIS (a)–(d) four camera channels and (e) MOUS. The well-corrected field area, i.e., the fraction of the $3' \times 3'$ focal plane area which is diffraction limited, is shown for each channel, measured at wavelengths 3098, 1190, 692, 366, and 400 nm, respectively.

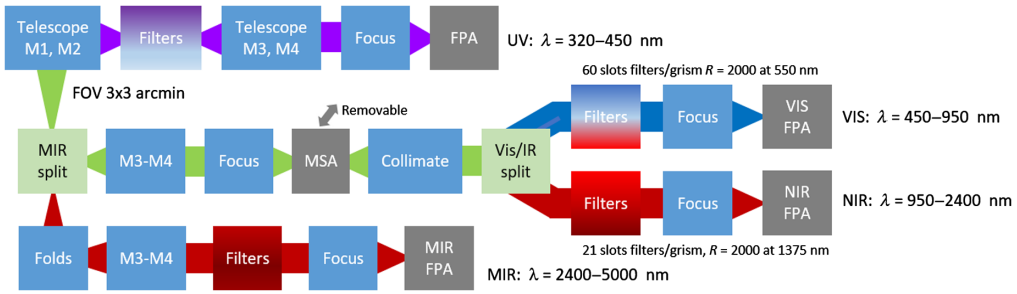

Fig. 44 Schematic of MOVIS showing the principal components. The UV channel has a separate field. The Vis/IR channels share the same beam train before a final split and share the same field as the MIR channel.

wavelengths share the same $3'$-square FOV, whereas the near-UV channel has a separate FOV, enabling a higher throughput beam path. An MSA is provided for use in spectroscopy mode or to facilitate observations of fainter objects in bright fields. Sets of filters based on the Hubble WFC3 sets[90] are provided for spectroscopic observations in the UV, Vis, and IR channels. Each filter set also includes one or more zero-deviation dispersing prisms, which can be used in series with another filter to select a spectral resolution and band of interest. Additionally, a set of filters is provided in the MIR channel. This instrument is intended for general use on objects both inside and outside the solar system and provides 2.5× better resolution than Hubble with more than 6 times as much collecting area.

MOVIS has a UV band covering 320 to 450 nm, a visible band (Vis) covering 450 to 950 nm, a NIR band covering 950 to 2400 nm, and an MIR band covering 2400 to 5000 nm. The optical layout of the instrument is shown in Fig. 45. To provide a multiobject spectroscopy facility, the Vis and NIR channels share a common MSA (not the MOUS MSA, but a separate one within MOVIS) that is removable for imaging purposes. The MSA consists of a set of four units, closely butted together, of the NexGen type with 1680×840 apertures total: again, 180 μm $\times$ 80 μm in size on 200 μm $\times$ 100 μm pitch. Each component has more than 4× the optical area of the component MSAs designed for NIRSPec. The UV channel views a separate field from the Vis/NIR/MIR channels and does not have an MSA, allowing the channel to have fewer mirrors and higher UV transmission than if it shared the optics with the Vis/NIR/MIR channels. The Vis, NIR, and MIR channels observe the same $3' \times 3'$ field simultaneously through dichroic beamsplitters. Thus extremely broad band (450 to 5000 nm) imaging and spectroscopy on a chosen field can be achieved in a single observation. The switch between imaging and spectroscopy modes in Vis and NIR is implemented using flip-in grisms located in the filter wheel assemblies, together with the insertable MSAs. The spectral resolution when in spectroscopic mode is $R = 2000$ in Vis and NIR channels. All channels are equipped with filter wheels for use when imaging. Additional low- or medium-resolution spectroscopic capabilities could readily be provided in the UV and MIR channels.

The MOVIS UV and Vis channels would utilize deep-depleted, delta-doped charge coupled device (CCDs) with 12-μm pixel size, in a 3×3 mosaic, providing a total of 12k $\times$ 12k pixels.

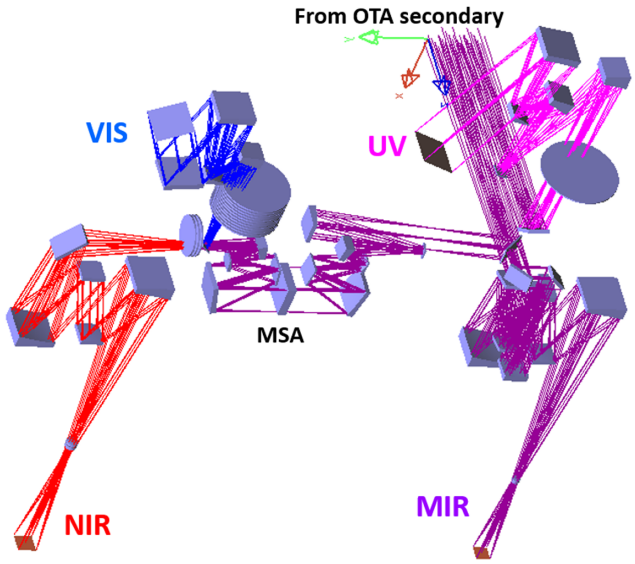

Fig. 45 Optical layout of MOVIS, showing the beam entering from the telescope secondary, the tertiary and quaternary mirrors and the grating wheel. Optionally, optical filters can be placed into the beam before the focal plane.

The FPA would be cooled to 153 K. The NIR channel would utilize a low-noise hybrid HgCdTe/CMOS detector, such as the Teledyne© H4RG, with 10 μm pixels in a 4k $\times$ 4k format.

The optical design of the MOVIS UV channel includes aspheric tertiary and quaternary mirrors that create a collimated beam, demagnified by about 144× from the primary mirror. Following the quaternary, a three-mirror imager (utilizing rotationally symmetric aspheric shapes) forms a $f/41$ final focus. The RMS WFE across the $3' \times 3'$ FOV is <39 nm.

In the Vis/IR channels of the MOVIS, as in the UV channel, tertiary and quaternary mirrors create a collimated beam at about 144× angular magnification from the primary mirror. However, the optical design of the rest of the Vis and IR channels is more complex than the UV channel, due to the need for an MSA. The Cassegrain focus after the telescope secondary could not be used for the MSA in these channels because the focus there (further off-axis than the MOUS FOV) is not well corrected. The tilt and decenter and shape of the telescope secondary were optimized for high performance specifically at the MOUS MSA FOV and therefore the performance at the Cassegrain focus of the MOVIS NIR/Vis FOV was not adequate for an MSA. Therefore, after the Vis/NIR quaternary, a four-mirror focuser creates a well-corrected telecentric $f/33$ focus where the MOVIS MSA is located. The MSA is followed by the inverse of the focuser, creating another collimated beam. A dichroic beamsplitter is placed in the collimated beam to reflect Vis and transmit NIR light. Following the beamsplitter in each channel is a filter wheel assembly that holds several wheels carrying filters or dispersing elements. After the filter assembly is the final focusing section. In the NIR channel, this is an $f/20$ refractive group consisting of five rotationally symmetric elements of common near-IR materials (zinc sulfide, zinc selenide, and fused silica). This refractive solution is compact and is adequate to correct chromatic aberration. In the Vis channel, the $f/41$ focusing group consists of three mirrors (one of which is a rotationally symmetric aspheric and two of which are Zernike aspherics). Figure 43(a)–(d) shows the Strehl ratios and well-corrected field fractions for the four MOVIS imaging channels.

6.4 *EXoPlanet Range Extended StarShade Instrument*

EXPRESS provides separate UV, visible, near-IR, and mid-IR channels sharing the same 8″-class diameter FOV, as shown in Fig. 46. Table 11 shows the operating regions for EXPRESS. In each case, two of the instrument channels are used for science (since the starshade bandwidth is wider than the bandwidth of the individual channels) and one channel is used for guiding,

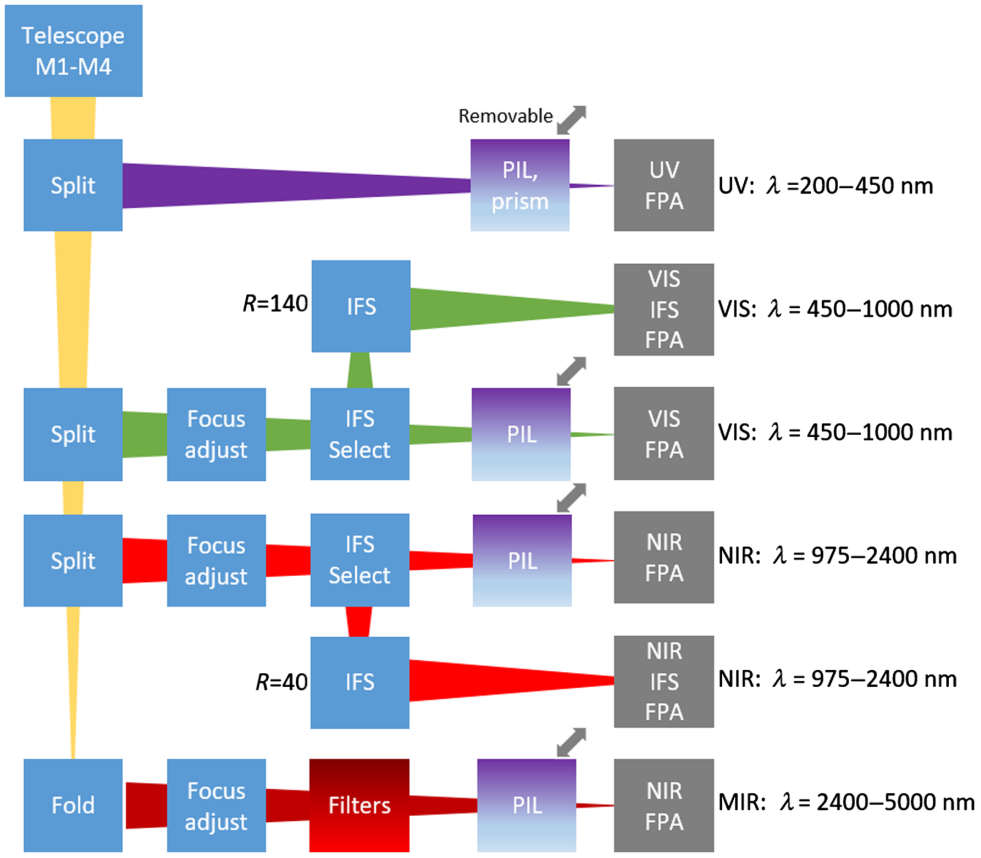

Fig. 46 Schematic of EXPRESS. Light from the telescope is split into four channels using dichroic beamsplitters. All channels share the same FOV and can be operated as imagers or as starshade guide channels via insertable PILs. For spectroscopy, the Vis and NIR channels each carry an IFS and the MIR channel carries filters.

Table 11 Starshade operating bands.

Science band (nm)	Express channels			
	UV	Vis	NIR	MIR
200 ≤ 1000	Science	Science	Guide	—
600 ≤ 2000	Guide	Science	Science	Guide
1000 ≤ 5000	—	Guide	Science	Science

with an optional channel choice shown in brackets. All channels can be used in an imaging guider mode and the Vis and NIR channels can be used in imaging or narrower 1.1 to 1.8 arc sec field spectroscopic modes. A typical operational configuration might be to utilize the UV channel in guider mode, with the pupil imaging lens (PIL) inserted in the beam to create a pupil image on the UV detector, whereas the NIR and Vis channels perform imaging or spectroscopy. As an alternative in this particular mode, the guide signal can also be picked up in the MIR channel, which may be helpful when observing cooler stars. Selection of modes within each channel is done using insertable devices: selector mirrors for the Vis and NIR channels to send the light to the imaging FPA or through the respective IFS optics; PILs in the IR and UV channels and an insertable prism in the UV channel.

The optics common to the EXPRESS channels consist of the telescope primary and secondary mirrors, and the aspheric tertiary and quaternary mirrors that create a collimated beam,

magnified by 116× (angular) from the primary mirror. In small-beam space, the field angular diameter is only 0°.28 total, so a simple off-axis paraboloid is sufficient to form a high-quality $f/80$ converging beam, with rms WFE of up to 27 nm across the field. This $f/80$ beam propagates directly to the FPA in the UV path and is the input beam to the Vis, NIR, and MIR paths in which the final f number is smaller.

The four EXPRESS channels share the same far-field FOV and are separated by dichroic beamsplitters. The first beamsplitter reflects the UV to its $f/80$ focus and transmits the Vis, NIR, and MIR. The second beamsplitter reflects the Vis and transmits the NIR and MIR. Following the Vis/IR beamsplitter, in reflection, is a weak doublet of radiation-resistant glasses that converts the $f/80$ beam emerging from the paraboloid to the $f/70$ focus required for the Vis channel. The RMS WFE in the Vis channel is <30 nm across the 450- to 1000-nm band. Following the Vis/IR beamsplitter in transmission, the beam crosses to the opposite side of the spacecraft bus, which is the cold side. A conic mirror collimates the beam and another dichroic beamsplitter in collimated space separates the beam into NIR and MIR paths. In both IR paths, a refractive doublet makes the final focus onto the imaging FPAs. The RMS WFE at the imaging FPAs is a maximum of 66 nm in NIR and 80 nm in MIR, yielding excellent image quality across both bands. In the NIR path, a switch-in mirror diverts the light to an IFS.

In the EXPRESS paths described, flip-in elements have been designed for other modes besides far-field undispersed imaging. In the UV path, a PIL may be inserted that forms an image of the primary mirror on the FPA, allowing starshade guiding. Also in the UV path, a prism (carried by the same mechanism as the PIL) may be inserted to perform $R = 5$ dispersion. In the NIR path, a PIL may be inserted to create an image of the primary mirror when using this channel for starshade guiding.

The Vis and NIR channels also have IFS modes with separate FPAs, accessed by flipping in a flat mirror in the image spaces ($f/71$ for Vis and $f/51$ for NIR) to access two-mirror relays that magnify the images onto lenslet planes. Following each lenslet plane is a collimator, prism and focuser to create dispersed images at the FPAs. The NIR IFS relay optics between lenslet and FPA consist of back-to-back six- or seven-element objectives, with a zinc sulfide prism ($R = 40$) between them in collimated space. The overall magnification is 0.7. RMS WFE in the NIR IFS varies with wavelength but has a worst case value of 98 nm. The Vis IFS relay optics between lenslet and FPA consist of back-to-back three-mirror objectives, with an NBK7 prism ($R = 140$) between them in collimated space. The overall magnification is 1. RMS WFE in the Vis IFS varies with wavelength but has a worst case value of 97 nm. DoF exist to improve the performance in the final design.

The present design features filter-based imaging spectroscopy in the MIR as a low-resolution, high signal-to-noise ratio (SNR) option but there is space in the instrument bay for a specific spectroscopic EXPRESS MIR channel. Recent work[91] has reaffirmed that a Fourier transform spectrograph (FTS) can compare favorably against an IFS in the noise conditions likely to be encountered at longer wavelengths. An FTS also offers dynamic flexibility in the choice of spectral resolution R. A broad trade study between filter sets, FTSs, and IFSs, which considers source and background SNRs, candidate detector characteristics, and in-depth analysis of the ideal values of R for target species detection, could lead to the inclusion of an EXPRESS MIR spectrograph channel.

6.5 *Fine Guidance Instrument*

The FGS enables accurate pointing on the target star using field stars in two regions of the sky when the starshade covers the target. The 1σ raw angular detection accuracy[68] in each of the two channels is approximately $\lambda(\pi d\sqrt{N})^{-1}$, where N is the photon count, d is the 6-m aperture diameter, and λ is the wavelength (visible band). Dark current, read noise, and thermal drifts will affect this figure, but with an electron-multiplying CCD (EMCCD) detector and a stable thermal environment (the case here), submilliarcsecond accuracy can be assumed even on relatively faint guide stars of 15 mag. The two FGS channels can be seen in Fig. 40, labeled "Guiders" and the schematic layout is shown in Fig. 47. A scan mirror in each channel allows selection of field stars and the FOR is sufficiently large to find guide stars over more than 95% of the sky.

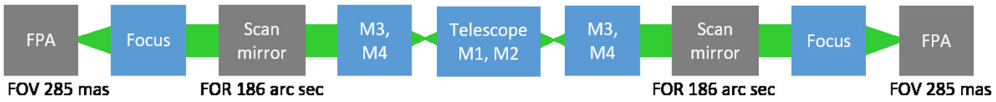

Fig. 47 Schematic of topologically identical guide channels, which take widely separated views of the sky. Scan mirrors enable selection of guide stars within a 186″ FOR.

6.6 *Potential Additional Exoplanet Instrumentation*

The ATSA telescope platform could potentially be augmented by other exoplanet science instruments. Unlike starshades, for which the mission DRM must be carefully prescribed, coronagraphs provide a flexible and agile exoplanet observing capability, most useful for exoplanet discovery but also capable of spectral characterization. This is provided that both broadband starlight suppression and high exoplanet throughput can be simultaneously achieved with coronagraphs on the ATSA telescope. At the current state of the art, high-contrast ($\simeq 10^{-10}$) coronagraphs are not well-suited for use with apertures having central obscurations[92,93] and spiders, such as are found on NGRST. Segmented apertures, however, which also pose difficulties for many coronagraph designs, can work satisfactorily with apodized coronagraph schemes, especially when combined with a vortex mask. Apertures having low f numbers are undesirable, owing to the problem of polarization crosstalk[94] caused by differential phases induced between the polarizations upon reflection from mirrors. HabEx 4.0H employed an $f/2.5$ off-axis design with a monolithic primary mirror, thus avoiding these issues, but it is clear that to provide the largest possible apertures in space, segmented apertures will need to be employed, just as on the ground. Also shorter telescopes and hence smaller f numbers are desirable from an engineering standpoint.

Can other types of instrument be deployed with the ATSA aperture? For example, high-precision astrometry using diffracting pupils applied to the primary mirror[95] is a technique not yet applied to space, but with projected astrometric accuracy well below 0.1 μarc sec, a 6-m aperture would be capable of detecting Earth-size exoplanets at 12 pc (producing ~0.25 μarc sec stellar motion).[96] A recent study[97] is showing potential for this technique with HabEx 4.0, where the diffracting pupil is a removable surface downstream of the OTA. For a metrology-stabilized segmented aperture, such as ATSA's, the technique would be worth studying.

Another recent development is the pupil-plane vortex fiber nuller,[98] which can be considered the smooth limit of the multiaperture nulling configurations proposed for Terrestrial Planet Finder Interferometer (TPF-I)[99] and Darwin.[100] This technique[101–103] is soon to be tested on the segmented Keck aperture, providing a useful data point for ATSA. Note that when used for nulling, the telescope aperture is capable of detection well within the usual coronagraph limit.[104] A cross-aperture single-baseline nuller has an IWA equal to $\lambda/4b$ (where b is the interferometric baseline) and this is equal to between 1/4 and 1/3 λ/d, approximately an order of magnitude closer to stars than a full-aperture coronagraph (IWA ~$2.5\lambda/d$). Thus nulling configurations, which had fallen out of favor post-TPF, may yet make valuable contributions to exoplanet science by combining smaller IWAs, as demonstrated by the Palomar fiber nuller,[105] with all the agility of coronagraph-based techniques. Another addition to the nulling stable is the grating nuller, which combines naturally achromatic beam combination with ease of fringe rotation.[106] Opportunities to develop and test these new techniques may eventually result in the development of alternatives to conventional coronagraphs and starshades.

In addition to these alternatives, one challenge in coronagraph technology development is to develop high-contrast instruments capable of 10^{-10} diffracted starlight suppression over broadbands while maintaining high throughput. For example, coronagraph core throughput (defined as the fraction of planet light captured in a region $0.7\lambda/D$ in radius) in the NGRST-CGI instrument (when using the Hybrid Lyot masks) falls below 5%—compared to the 34% core throughput of the telescope itself—owing partly to the negative effects of the obscured aperture.[107,108] While discussion of the potential for coronagraphy on segmented telescopes is outside our scope, the addition of a high-performance coronagraph to ATSA would (potentially) enhance its capabilities for exoplanet studies. Concepts for an apodized vector vortex designed for the ATSA aperture geometry are being developed.[109] Without minimizing the difficulties of incorporating a

coronagraph, an active PM, as part of a system of two downstream DMs, would considerably reduce the initial WFE and hence the energy subsequently spread into higher spatial frequencies as part of WFC. Mid-spatial frequencies are particularly challenging because the scattered light appears close in.[93]

An ideal coronagraph solution for segmented telescopes has not yet been identified. Among the types being studied are binary and gray scale apodizer masks that would be inherently achromatic and provide broadband starlight suppression with reasonably high exoplanet light throughput. Furthermore, the vortex coronagraph mask offers significant advantages compared to the Hybrid Lyot design (one of two coronagraph types employed in NGRST-CGI) with its much greater tolerance to low-order aberrations, such as tilt.[93] These low-order aberrations dominate coronagraph performance when telescope motion, thermal effects on the optical train, and vibration are considered. Detailed sensitivity analyses of apodized vortex coronagraphs for unobstructed hexagonal segment apertures are made in Ref. 93. The same approach to coronagraph design could be applied to the centrally obstructed, segmented ATSA aperture. We note, however, that high-contrast coronagraphic observations will prove particularly challenging in the UV whatever the entrance aperture geometry, where polarization-induced aberrations and throughput limitations are amplified, whereas wavefront stability and stray light requirements get more stringent. Where high-contrast spectral observations of exoEarths are required in the UV, starshades may be the only solution.

In terms of science, the provision of complementary techniques has been shown on HabEx 4.0H[2] with its starshade and its coronagraph, to roughly double the exoplanet yield. With segmented telescopes likely to become the norm in space in the future, further study of these possible techniques should be rewarding.

7 What Technology Developments Are Needed to Complete ATSA?

With the segmented apertures that are commonplace on the ground now being adapted for use in space, coronagraph designs that accommodate segmented primaries are being developed. Although these designs are very much in their infancy, the progress that has been made both in modeling and in hardware is considerable and should not be dismissed. Developments in ground instrumentation applied to exoplanet science will find their way on to space platforms; a few of these concepts were briefly discussed in Sec. 6.6. Finally, we note here that smaller segment gaps are both desirable (to reduce diffraction artifacts) and feasible. The absolute minimum gaps would require a lightweight inner barrel extending from the PIP, supporting the secondary mirror via a thin spider. In this case, 25-mm gaps can be assumed throughout. The outer barrel would not then need to be so rigid a structure, promising little change in total mass.

To reach the shortest wavelengths, high-efficiency mirror coatings are required. Aluminum-based coatings were used on Hubble, enabling its UV capability and have proved durable. Nevertheless, although protected aluminum coatings have good reflectivity at short wavelengths, they do not reach the theoretical best performance of bare aluminum at the shortest wavelengths, which could push down well below 100 nm. Furthermore, the protected, high-efficiency coatings developed so far introduce degraded performance in the 200- to 300-nm region, so a solution has yet to be developed that would improve on the simple Hubble formula of aluminum with a magnesium fluoride overcoat. As things stand, aluminum coatings provide science to the 100-nm region while placing limits on the optical design. To go to shorter wavelengths with improved coatings would place additional requirements on the optics (e.g., better SFE). Thus improved coatings are highly desirable but not critical technology.

Many of the developments needed to enable ATSA are shared with the smaller concept of HabEx 3.2S. That system has 12 technologies that are currently at TRL 4 or 5 and are in need of further development. To those, the cryospecific requirements can be added. Summarizing and condensing that list, all the following are expected to be at TRL 5 or higher by 2023.

1. Starshade petal position and shape accuracy and stability, both currently TRL 4.
2. Starshade scattered sunlight for petal edges, now at TRL 4. Further progress has been made recently.

3. Starshade contrast performance modeling and validation is currently at TRL 4.
4. Starshade lateral formation sensing is at TRL 5.
5. Laser metrology is now at TRL 5 and expected to be at TRL 6. We assign TRL4 for operation at cryogenic temperatures.
6. Various detector technologies including MCPs (for UV), EMCCDs (for visible), and LMAPDs (for NIR) are at TRL 4.
7. Microthrusters are now at TRL 4.
8. MSAs with higher shutter count, currently TRL 3, are expected to be TRL 5 by 2023.

The development of cold mirror segments is an enabling technology, with the current state-of-the art represented by the technology demonstration mirrors referenced in Sec. 3.3. AHM mirrors are at TRL5 and full-scale, athermalized ATSA mirrors are at TRL3. The required developments would involve fabrication and test of a complete segment with its actuators and testing at both room and cryotemperatures. The modeling and ultimate demonstration of a low starshade OS temperature is another required development. Many of these needs are already in work and at least partially funded[110] and with continued funding and additions where needed, provide a strong basis for an ATSA telescope mission to be started in the mid-2020s.

8 Exoplanet Instruments: Yield Modeling

In this section, we calculate the exoplanet yields for a wide population of exoplanets assuming spectroscopic observations over the full visible wavelength range, covering 300 to 1000 nm. For true exo-Earth analogs, this range gives access to the O_3 cut-off short of 330 nm, O_2 A band around 760 nm and multiple water bands centered at 720, 820, and 940 nm. A methane rich atmosphere would also show spectral features at 730, 790, and 890 nm. In order to estimate the number of exoplanets that can be characterized up to longer infrared wavelengths than 1 μm, we consider different infrared bands. The starshade IWA is constant over each band and set by the longest wavelength in each band. We considered three infrared bands.

- *IR1 band: from 720 to 2400 nm*. Observing at wavelengths redder than 2 μm (Fig. 1) gives access to N_2O, which is considered as a biosignature when detected in conjunction with O_2 (or O_3) and which is undetectable at shorter wavelengths. The IR1 spectral range also provides access to broader and stronger absorption features than accessible short of 1 μm for H_2O (at 1.13, 1.41, and 1.88 μm), CH_4 (at 2.32 μm), as well as CO_2 (at 2.03 and 2.29 μm), which has no absorption features short of 1 μm. Starshade distance = 49,906 km, IWA = 149 mas.
- *IR2 band: from 1020 to 3400 nm*. Giving access to one more (deeper and broader) CH_4 feature at 3.3 μm and one more CO_2 feature at 2.7 μm. Starshade distance = 35,228 km, IWA = 211 mas.
- *IR3 band: from 1500 to 5000 nm*. Giving access to the strongest CO_2 absorption around 4.3 μm. Starshade distance = 23,953 km, IWA = 310 mas.

8.1 *Yield Modeling Approach*

EXOSIMS[76] performs full, end-to-end mission simulations of exoplanet direct-imaging missions. Every aspect of the mission, from the orbital position of the spacecraft, to the characteristics of its optical system, to the target stars and their planet populations, and their time-varying positions, is described parametrically. Full missions are scheduled using specific descriptions of observing rules, and each individual observation is evaluated on a specific sample of simulated exoplanets drawn from the governing population. Monte Carlo ensembles of mission simulations are generated with different samples of planets and orbits, and these are then analyzed to calculate distributions of mission performance metrics. Full mission simulations allow for the exact inclusion of dynamical constraints and allow for simultaneous calculation of a wide range of scientific and engineering metrics of interest (e.g., spectral characterizations and fuel use).

8.2 *Astrophysical Inputs*

The astrophysical assumptions and inputs are summarized here and discussed in greater detail in the Exoplanet Exploration Program Office's Standard Definitions and Evaluation Team (ExSDET) Final Report.[81] Uncertainties in yield are dominated by uncertain knowledge of astrophysics inputs, particularly for exoplanet occurrence rates and the brightness of exozodiacal light.

Exoplanet occurrence rates were based on the EXOPAG SAG-13 power-law model of Kepler data,[111] as modified by Dulz et al.[112] for planets with larger masses and orbital radii. In particular, the occurrence rate for Earth-like planets is taken to be 0.24. Exo-Earth candidates (EECs) were assumed to be on circular orbits and to reside within the conservative HZ, spanning 0.95 to 1.67 AU for a solar twin.[113] EECs span radii ranging from $0.8a^{-0.5}R_{\oplus}$ to $1.4R_{\oplus}$, where a is the semimajor axis for a solar twin, and $R_{\oplus}$ is the Earth radius.

The stray light from binary stars in the final image plane was estimated[114] and included as an astrophysical noise source in exposure time calculations. The solar zodiacal cloud brightness was estimated as a function of wavelength and ecliptic latitude and longitude by adapting and interpolating data from published tables. [115] EXOSIMS specifically schedules each observation, enabling it to compute the zodiacal brightness based on the target's ecliptic coordinates on the date of the observation. The exozodiacal light levels were drawn from the recent results of the Large Binocular Telescope Interferometer survey of exozodiacal dust, represented as a probability distribution with a median brightness level three times higher than in the Solar system case.[116]

EXOSIMS uses the ExoCat-1 catalog of nearby main sequence stars.[117,118] Any necessary but missing photometric information for targets is optionally synthesized by interpolating over Eric Mamajek's Mean Dwarf Stellar Color and Effective Temperature Sequence.[119] ExoCat-1 is further modified to include the physical characteristics of any multiple systems (delta magnitude and separation) from the Washington Double-Star catalog, maintained at the U.S. Naval Observatory, allowing modeling of the amount of starlight contributed by any known nearby stellar companions.

The telescope–instrument combinations are modeled parametrically using the values presented in this paper.

8.3 *Observing Scenario*

The starshade-only observing scenario begins with the starshade performing a blind search survey. When a planet is discovered, the starshade remains on that target to perform a spectral characterization. The starshade returns at later times ("epochs") for follow-up imaging for orbit determination. The integration time is set to reach an SNR of 7 for broadband imaging and an SNR of 10 per resolution element for spectroscopy, using the brightness of the planet determined by initial imaging and assuming a Lambertian phase function.

Follow-up imaging-mode detections contribute to orbit determination. For the cases studied, not all targets that are spectrally characterized received all the requisite orbit determination observations, due to practical timing constraints for observing with the starshade. The TSP optimization cost function includes terms for the EEC search completeness around each target, transition distance, revisits for orbit determination and the number of potentially missed targets during the blind search survey. The spectral characterizations take highest priority. The cost function coefficients used here were achieved with a preliminary tuning and could be further refined. The cost function coefficients should be retuned for changes in observing scenario and architecture, particularly starshade-telescope separation, mass, propulsion type, and fuel mass.

8.4 *Precursor Knowledge*

In the absence of a coronagraph or a second smaller, more agile starshade focused on rapid broadband exo-Earth detection, precursor knowledge of HZ rocky planets would rely on prior surveys using precision RV measurements, astrometry, or ground-based direct imaging. Ground-based ELTs equipped with extreme adaptive optics and high-contrast starlight cancellation

systems may have the capability to detect Earth-like planets around a dozen M stars,[120] but likely not around the solar-type stars targeted by ATSA. Astrometry would need to reach microarcsecond level precision, which is only accessible from space (and at least 20× better than Gaia[52] will provide). The Space Interferometry Mission[121,122] had the potential to reach as many as 65 exo-Earths with ∼1 μas precision but was canceled. Other ideas, e.g., diffractive pupil astrometry,[123] are only just beyond the concept phase. For the foreseeable future then, the leading technology for detecting and measuring the orbits of exo-Earths around Sun-like stars is ground-based extreme precision radial velocity (EPRV) measurements.[124] The required precision is ∼10 cm/s (with a few cm/s stability over many years), which is significantly better than the 1-m/s routinely achieved by current ground-based RV instruments. Recognizing this gap and the high impact of precursor knowledge on the design and science yield of any future exo-Earth direct characterization mission, the 2018 National Academy of Sciences (NAS) Exoplanet Science Strategy report [125] recommended the development of EPRV measurements as a critical step toward the detection and characterization of exo-Earths. In response to that recommendation, NASA and NSF commissioned an EPRV group to recommend a ground-based program architecture and implementation plan to achieve the EPRV goal intended by the NAS. Only the next 5 to 10 years of EPRV work will tell if such measurements are achievable.

In the baseline observing scenario described above, no prior knowledge of EECs—nor of any other planet types—is assumed around the targets and the burden of a blind search survey falls on the mission. For the opposite extreme, we consider a case in which perfect knowledge of the location and orbits of the exo-Earths exists around all target stars. In that extreme case, no blind search is necessary and only spectral characterizations are performed. This perfect prior knowledge case investigates the upper bound set by the scheduling of the starshade for spectral characterizations and defines the capability of the instrument to exhaust targets within the maximum integration time criterion of 60 days per spectral observation. Having any precursor knowledge of EECs, either from ground- or space-based surveys, would produce EEC characterization yields within these two bounds. We evaluate one particular precursor case: detection of EECs with EPRV with sensitivity 3 $\mathrm{cm\,s^{-1}}$. EPRV sensitivity degrades with increasing stellar temperature. We incorporated EPRV precursor knowledge into EXOSIMS: each synthesized planet around a given star is tested against a heuristic of the EPRV sensitivity for that particular star and planet mass.[126] If the planet is detectable by EPRV, it is designated for spectral characterization at mission start. The null results of EPRV are not used; the blind search survey is conducted on all targets without EPRV precursor planets.

8.5 *Yield Results*

The yield was calculated for the no-prior knowledge, perfect-prior knowledge, and EPRV-prior knowledge cases. The yield simulations were performed with synthetic planets of all the Koppurapu planet types[127] drawn from the Dulz occurrence rates,[112] using an ensemble of 100 randomly drawn universes for each of the three prior knowledge cases. The mission rules prioritized exo-Earths when scheduling observations, and the yield of non-exo-Earths is incidental during the exo-Earth-centric observations. Greater yield of non-exo-Earths could be achieved with different mission rules. The yield is defined as the average number of exoplanets that were spectrally characterized to SNR = 10 with spectral resolution of 140 over a 108% bandwidth ranging from 300 to 1000 nm.

Figure 4 shows the cumulative number of exo-Earths spectrally characterized by the starshade over mission elapsed time. The upper bound set by the perfect-prior-knowledge case is 33 spectrally characterized EECs. The targets are exhausted in an average of 4.5 year. Extending the mission an additional year produces an average of 0.3 more characterized EECs. The conclusion is that the ATSA starshade architecture is target-limited and a corollary is that a slightly larger telescope aperture would provide access to more targets to leverage use of the starshade for the full five years of the mission.

At the other extreme, a blind search with the starshade uses about 65 transitions to yield an average of three characterized EECs. With EPRV precursor knowledge, the starshade benefits dramatically, raising the yield to 10 EECs and accelerating the time to half the yield from 641 to 214 days. Based on these yield results obtained for visible wavelength observations,

Table 12 Number of exo-Earths characterized and time to achieve 50% yield for different scenarios.

Observing scenario	No prior knowledge	Time (day)	Prior EPRV	Time (day)	Prior perfect	Time (day)
Starshade only, separation 120 Mm	3	641	10	214	33	580
Starshade only, separation 50 Mm	0.6		1.6		6.4	
Starshade only, separation 35 Mm	0.3		0.4		2.6	
Starshade only, separation 24 Mm	0.1		0.1		0.8	

the separation angle of the observed exo-Earths at quadrature was calculated and used to assess how many of these exo-Earths would still be observable given the IWA of the three infrared bands. These results are summarized in Table 12 and annotated in Fig. 4.

The yield of the exoplanets by Koppurapu type is shown in Fig. 48 for the perfect-prior case, in Fig. 49 for the EPRV-prior case, and in Fig. 50 for the no-prior case, observed in the visible. The perfect-prior case observed an average of 31 stars, each one having at least one exo-Earth. The no-prior case, utilizing a blind-search survey, observed an average of 53 stars, thereby having higher yields for sub-Neptunes and gas giants. The EPRV-prior case observed an average of 22 stars, fewer stars than the blind search. It resulted in higher exo-Earth and rocky planet yields but lower sub-Neptune and gas giant yields than for the no-prior case.

The planet yields and average number of stars observed are summarized in Table 13. As expected from previous analysis,[80] the number of exo-Earths that can be spectrally characterized by the ATSA starshade is a strong function of prior knowledge. In this table, the temperatures and Kopparapu planet types are aggregated into rocky planets ($0.5R_\oplus < R < 1.75R_\oplus$), sub-Neptunes ($1.75R_\oplus < R < 3.5R_\oplus$), and gas giants ($3.5R_\oplus < R < 14.3R_\oplus$). Within each set of planet types, the topmost row indicates the total number of planets seen in that set. Subsequent rows show the number of those same planets that can be observed in the longer

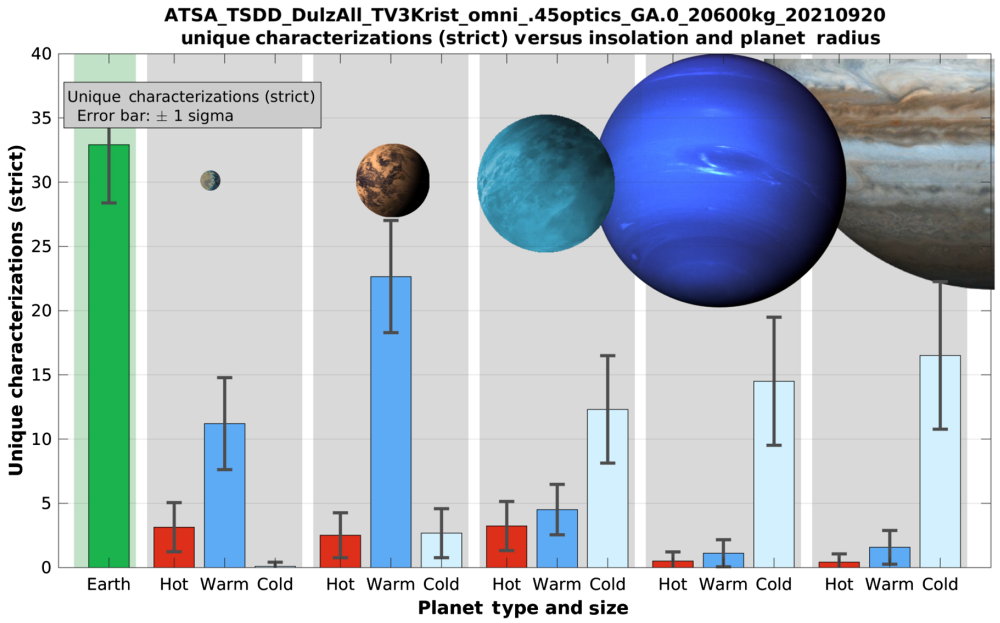

Fig. 48 In the perfect prior case, the starshade performs spectral characterizations on all exoplanet systems with exo-Earths and only those systems. The yield of other planet types characterized concurrently with the exo-Earths is shown for five planet types and their respective thermal zones[127]: small rocky, large rocky, sub-Neptune, Neptune, and Jupiter-like types. Exo-Earths are a subset of warm, rocky-type planets.

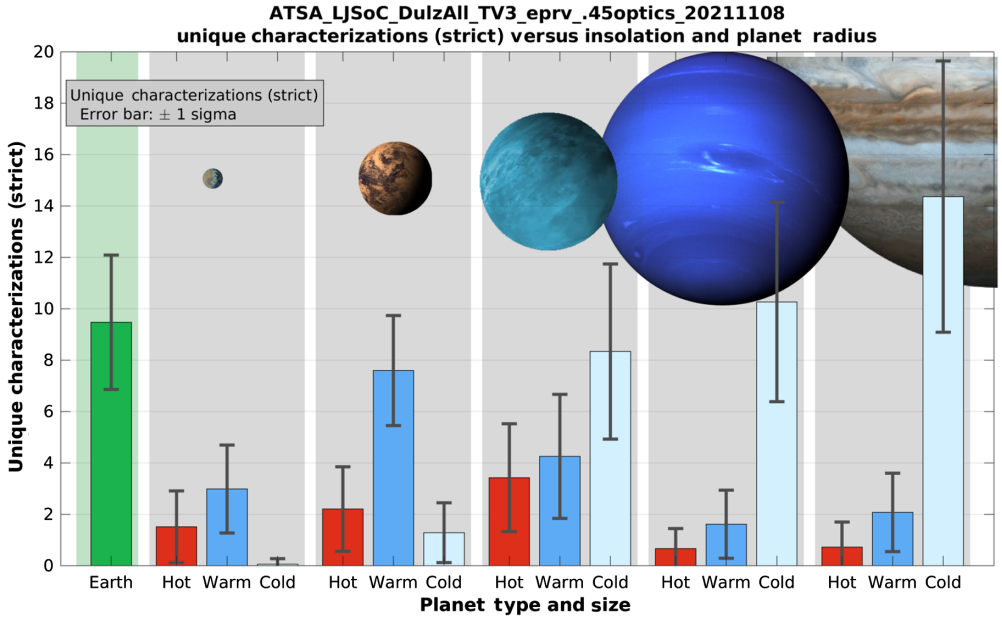

Fig. 49 In the case of prior knowledge from an EPRV instrument with 3 cm s^{-1} precision, the starshade performs spectral characterizations on all exoplanet systems with known exo-Earths and conducts a blind-search survey on the rest of the target stars.

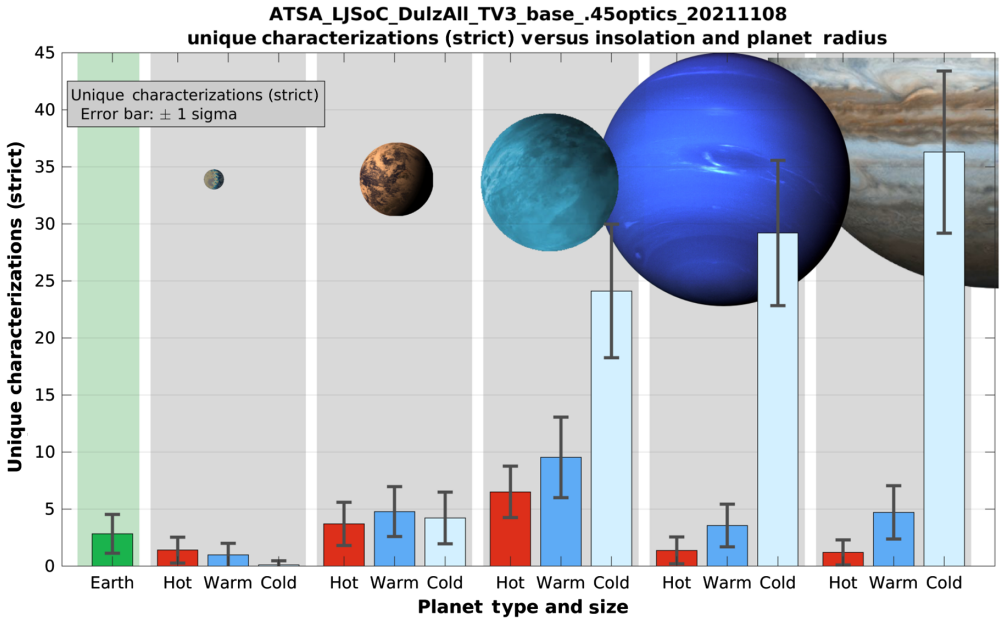

Fig. 50 In the no-prior case, the starshade performs a blind-search survey in broadband imaging mode to SNR = 7. When a planet is discovered, the starshade remains on the target and performs spectral characterization. The starshade revisits systems with discovered planets at multiple later epochs to image the systems and determine the planet orbits to discern which, if any, reside in the HZ.

wavelength bands. Thus while ∼1/3 of the total observable rocky planets are observable in band IR1, large, gaseous planets can be observed in all bands.

Utilization of recent work[72,79] on higher fidelity starshade transition and formation flying dynamics models in EXOSIMS could reduce the required fuel mass, which are anticipated to increase the yields by 15% or more. Additional optimization of the blind search, tuning

Table 13 Expected yield by planet type and wavelength range for different scenarios.

	Observing scenario		
Planet type	No prior	EPRV prior	Perfect prior
Earth-like	2.82	9.47	32.92
Earth-like IR1	0.59	1.64	6.36
Earth-like IR2	0.26	0.37	2.63
Earth-like IR3	0.10	0.05	0.79
Rocky	15.18	15.61	42.29
Rocky IR1	4.94	3.52	12.94
Rocky IR2	2.87	1.42	6.15
Rocky IR3	1.28	0.54	2.38
Sub-Neptune	40.14	16.01	20.07
Sub-Neptune IR1	26.42	8.24	14.02
Sub-Neptune IR2	18.12	5.33	10.37
Sub-Neptune IR3	10.30	3.03	6.64
Gas giant	78.38	30.21	35.63
Gas giant IR1	70.42	24.67	32.08
Gas giant IR2	59.94	20.91	28.81
Gas giant IR3	46.10	15.80	23.58
Stars observed	52.94	21.85	30.75

of the TSP cost function coefficients and refinement of the architecture could further increase exo-Earth yields by 10% or more.

9 Discussion

In common with the Decadal Survey study telescopes LUVOIR and HabEx, ATSA carries three instruments, two for GA and one for exoplanet studies. This instrument complement is not exclusive but instead illustrates the adaptability of the ATSA telescope concept, especially when the benefits of the active primary mirror and the passively cooled, 100 K telescope are considered. Though ATSA carries general purpose science instruments, such as cameras and spectrographs with large fields of view, it also carries a specialized starshade instrument for which only a narrow field is required. This general design could be adapted to create large-aperture, wide-field telescopes, with considerable agility when compared with for example, JWST with its ungainly sunshield. Different instrument types can certainly be included and, using the concept of robotic serviceability, one would consider an adaptable, modular instrument bay along the lines of Hubble's, so that new instruments with the latest technology could be introduced to the basic mission.

Coronagraphs are attractive—essentially a single device added within the telescope. Compared to a starshade, a coronagraph-based system is supremely nimble and thus ideal for surveys. On the other hand, the overhead is large. Witness the heroic, system-wide engineering efforts to stabilize HabEx 4.0H[2] for coronagraphy. Currently, dreamed-of coronagraphs provide only one fifth (or as little as one tenth, if polarization is taken into account) of the instantaneous

bandwidth of starshades: if spectroscopy is important (and it is) coronagraphs take much longer to acquire a broad spectrum. As a result, a coronagraph-only mission has no advantage over a starshade-only mission in terms of spectral yield.[2] Against this equivalence, one must set the huge spectral range and accompanying science yield that can be achieved by a starshade. Where a coronagraph to be added to ATSA, current coronagraph mask designs would provide only modest contrast and poor throughput. Further developments in coronagraphic techniques and polarization control are needed to allow high-contrast coronagraphy to function on this type of platform. The most straightforward route would be to lengthen the telescope to ∼15 m primary–secondary separation to improve the polarization response and to move the secondary mirror off-axis to reduce diffraction and thus improve the coronagraph performance. Other exoplanet-finding and characterization techniques[101] applicable to this aperture should also be developed. Note in particular, that cross-aperture nulling[105,106] and variations on pupil-plane vortex nulling,[98,102,104] allied with single-mode fibers, offer much smaller IWAs than coronagraphs ($\sim\lambda/2$ versus $\sim 2.5\lambda$). Those smaller IWAs will increase the yields of inner rocky planets (potentially as much as 2×). Unlike coronagraphs, these systems are potentially resilient to segmented apertures. One such system will be tested at the Keck Telescopes shortly.[128]

The large launch vehicles now in the development will provide alternative options. For example, scaling up would yield a greater number of Earth-like planet characterizations from the increased light gathering capability. Larger fairings may also support co-launching the 6-m baseline telescope with the starshade (depending on mass distributions) to save the expense of a second launch vehicle. The three launch configurations discussed earlier also provide the following options.

1. The SLS Block-2, 10 m ∅ PLF long (×27.4 m tall) is in the development for planned 2029 operation and has an estimated 9.1 m∅ × 25.2 m tall interior with sufficient volume to co-launch the ATSA 6-m baseline with the (furled) 72-m ∅ Starshade. Much more analysis would be needed to verify this option.
2. The second option also uses the SLS 10 m ∅ PLF long. Notably, this fairing has sufficient volume for ATSA to be scaled up to an 8-m ∅ aperture with $\sim 2.25f/D$.
3. The third option is the SpaceX Starship+5-m extension which has a dynamic interior volume of 8 m∅ × 23.24 m tall, supporting launch of the ATSA baseline aperture with $\sim 2.33f/D$. The shroud interior also optionally supports two volumes locally extending the diameter to 9 m, providing additional margin. The starshade would launch separately on a second Starship with the standard fairing.

Improvements have been made in the production of medium size (∼1 m^2) SiC mirrors.[129] When clad with amorphous Si or chemical vapor deposition SiC facesheets,[130] rms surface roughness of <2 Å has been achieved after polishing,[131] promising low-scatter performance, which is most important in the UV. This cladding process is widely used in industry and should be capable of further development and application for cold optics. With an array of FCAs allowing fine control of the surface figure errors introduced from manufacturing, gravity release, or cooling, such lightweight, stiff mirrors are an enabling technology for future space telescope missions in the UV-optical-IR range. In an athermalized design, such mirrors will enable ∼10 nm rms surface figure error at room temperature and at the 100-K operating temperature.

Finally, we note that the starshade model used here is not the only one that will work with ATSA. Smaller, more nimble designs may also fit the mission, especially when a complete noise budget that considers starshade stray light and background sources (exozodiacal light) near the IWA is created.

10 Conclusion

A single observatory can provide background-limited observing capability from UV to MIR. Background-limited wavelength coverage from ∼100 nm to 5 μm is enabled by passive cooling of the telescope to ≤100 K. The cold optics enable observations out to 5 μm without interference from strong thermal emission from the telescope, opening up a spectral region in exoplanets rich in features from water, methane, carbon dioxide, ammonia, and other indicators of composition, physical conditions, habitability, and perhaps biology. The scientific advantages of being able to

observe this part of the spectrum in exoplanets are so great that it makes little sense to throw them away by keeping telescopes in space at room temperature.

One interesting consequence of the cold telescope design is the positive effect on contamination during operation. At the low temperatures of the ATSA telescope, production of vapor from spacecraft materials will be minimized and optical performance longevity can be anticipated. The principal concern will be limiting the production of vapor before launch, when the telescope will be near room temperature.

A 100-K telescope and a 100-K starshade can be achieved by passive cooling. Passive systems eliminate the need for staged isolation with active cryocoolers, allowing a smaller bus mass, commensurate reductions in complexity and cost and, critically for a high-resolution telescope, elimination of vibration sources. The telescope's five-layer sunshield is sufficient to reflect and reradiate much of the insolation and the short, wide, steeply scarfed telescope barrel provides excellent exposure to cold space of the primary mirror and barrel interior. ATSA's segmented, cold, active, primary mirror allows predictable ground to space optical performance together with room temperature test capability. In-space control of the surface figure errors of the primary, together with optical configuration control using laser metrology, will provide diffraction-limited performance from 400 nm upward from a lightweight mirror.

EXOSIMS, the advanced observing simulation package, was used to provide the expected exoplanet yield for the starshade. With prior target knowledge from EPRV the starshade is likely to yield ~9 to 10 exo-Earths detected and spectrally characterized up to 1 μm and without prior knowledge, ~2 to 3. Perfect prior knowledge would yield ~33, ~6 of which could be observed all the way to 2.4 μm, ~3 out to 3.4 μm, and ~1 out to 5 μm. In the no-prior knowledge case, a greater number of stars are observed, leading to a preponderance of ~78 larger planets with a few exo-Earths out to 1 μm and ~46 large planets out to 5 μm. In this no-prior case, as many as ~16 rocky types would be observed.

Given that we expect to refine our target knowledge over time, one might argue that the engineering difficulties accompanying the incorporation of a coronagraph on ATSA would not be justified. On the other hand, with progress in coronagraph technology and the provision of longer launch vehicle fairings, these difficulties might not arise, leading to the conclusion that both starshade + coronagraph and coronagraph-only mission architectures will become viable. Projections of progress on coronagraphy are of course speculative.

DRMs run for HabEx showed that combined, "hybrid" missions produced greater yield, so mission-specific DRMs will be an essential component of any architecture trade. Newer concepts that straddle the boundary between coronagraphs and nullers need to be further developed and may yet produce the ideal agile survey modes and in-depth spectroscopy that currently, only combination mission architectures would provide.

Finally, for sheer adaptability, a starshade cannot be beaten. A single starshade can cover the entire near UV to infrared spectrum, simply by repositioning. It is limited only by the thermal radiation at the long end and by the telescope's capability at the short end. No current coronagraph concept can match that. A starshade will always provide smaller IWA, wider field of view, broader instantaneous optical bandwidth, and higher optical efficiency, and will work with both segmented and monolithic apertures.

Acknowledgments

The information given here is provided for planning and discussion purposes only. This work was conducted at the Jet Propulsion Laboratory, California Institute of Technology, under contract with the National Aeronautics and Space Administration. Government sponsorship acknowledged.

References

1. IPAC, "The NASA exoplanet archive," 2020, https://exoplanetarchive.ipac.caltech.edu/.
2. B. S. Gaudi et al., "The Habitable Exoplanet Observatory (HabEx) mission concept study final report," arXiv: 2001.06683 (2020).

3. The LUVOIR Team, "The LUVOIR mission concept study final report," arXiv:1912.06219 (2019).
4. National Academies of Sciences, *Engineering, and Medicine, Pathways to Discovery in Astronomy and Astrophysics for the 2020s*, The National Academies Press, Washington, DC (2021).
5. E. L. Wright, "The infrared sky [review article]," *New Astron. Rev.* **49**, 407–412 (2005).
6. M. Meixner et al., "Origins space telescope mission concept study report," arXiv:1912.06213 (2019).
7. E. W. Schwieterman et al., "Exoplanet biosignatures: a review of remotely detectable signs of life," *Astrobiology* **18**(6), 663–708 (2018).
8. S. D. Domagal-Goldman et al., "The thermodynamics of life on a planetary scale," in *AGU Fall Meeting Abstr., B11F–0099* (2014).
9. R. Hu, L. Peterson, and E. T. Wolf, "O_2- and CO-rich atmospheres for potentially habitable environments on TRAPPIST-1 planets," *Astrophys. J.* **888**, 122 (2020).
10. G. Arney et al., "The pale orange dot: the spectrum and habitability of hazy Archean Earth," *Astrobiology* **16**(11), 873–899 (2016).
11. J. Krissansen-Totton et al., "Is the pale blue dot unique? Optimized photometric bands for identifying Earth-like exoplanets," *Astrophys. J.* **817**, 31 (2016).
12. R. Hu, "Information in the reflected-light spectra of widely separated giant exoplanets," *Astrophys. J.* **887**, 166 (2019).
13. M. C. Turnbull et al., "Spectrum of a habitable world: earthshine in the near-infrared," *Astrophys. J.* **644**, 551–559 (2006).
14. A. Segura et al., "Biosignatures from Earth-like planets around m dwarfs," *Astrobiology* **5**, 706–725 (2006).
15. S. D. Domagal-Goldman et al., "Using biogenic sulfur gases as remotely detectable biosignatures on anoxic planets," *Astrobiology* **11**(5), 419–441 (2011).
16. S. Seager, W. Bains, and R. Hu, "Biosignature gases in H_2-dominated atmospheres on rocky exoplanets," *Astrophys. J.* **777**, 95 (2013).
17. C. Sousa-Silva et al., "Phosphine as a biosignature gas in exoplanet atmospheres," *Astrobiology* **20**(2), 235–268 (2020).
18. M. W. Werner et al., "Extension of ATLAST/LUVOIR's capabilities to 5 μm or beyond," *J. Astron. Telesc. Instrum. Syst.* **2**(4), 041205 (2016).
19. L. M. Bowman et al., "In-space assembly application and technology for NASA's future science observatory and platform missions," *Proc. SPIE* **10698**, 1069826 (2018).
20. R. S. Polidan et al., "Innovative telescope architectures for future large space observatories," *J. Astron. Telesc. Instrum. Syst.* **2**(4), 041211 (2016).
21. S. Martin et al., "ATSA: a cold, active telescope for Space Astronomy," *Proc. SPIE* **11443**, 114432A (2020).
22. Planck Collaborationet al., "Planck early results. II. The thermal performance of Planck," *Astron. Astrophys.* **536**, A2 (2011).
23. W. Calvin and J. D. Harrington, "Spitzer, studying the universe in infrared," (2009).
24. A. Mainzer et al., "Initial performance of the NEOWISE reactivation mission," *Astrophys. J.* **792**, 30 (2014).
25. D. Redding, "Active optics and large mirror technologies," in *ESA Space Optics Instrument Technology Course Notes*, Poltu Quatu, Sardinia (2016).
26. B. K. McComas and E. J. Friedman, "Field-balanced adaptive optics error function for wide field-of-view space-based systems," *Opt. Eng.* **41**, 567–574 (2002).
27. J. Steeves et al., "Active mirrors for future space telescopes," *Proc. SPIE* **10706**, 1070615 (2018).
28. NASA Exploration Systems Development (ESD) Division, "SLS mission planner's guide," 2018, https://explorers.larc.nasa.gov.
29. K. Hurd, Private communication 7/23/2020 (2020).
30. SpaceX, "Starship users guide," 2020, https://www.spacex.com/media/starship_users_guide_v1.pdf
31. E. Cady, "Boundary diffraction wave integrals for diffraction modeling of external occulters," *Opt. Express* **20**, 15196–15208 (2012).

32. G. Hickey et al., "Actuated hybrid mirrors for space telescopes," *Proc. SPIE* **7731**, 773120 (2010).
33. S. Seager, *Exoplanets*, The University of Arizona Space Science Series (2010).
34. J. B. Hadaway et al., "Cryogenic performance of lightweight SiC and C/SiC mirrors," *Proc. SPIE* **5487**, 1018–1029 (2004).
35. P. G. Halverson, T. J. Parker, and M. Levine, "Cryogenic performance of piezo-electric actuators for opto-mechanical applications," *Proc. SPIE* **6666**, 666613 (2007).
36. J. Steeves, F. Golinveaux, and C. Lynch, "Using the ferroelectric/ferroelastic effect at cryogenic temperatures for set-and-hold actuation," *Smart Mater. Struct.* **27**(6), 065024 (2018).
37. J. A. Nissen et al., "Laser metrology for ultra-stable space-based coronagraphs," *Proc. SPIE* **10398**, 103980I (2017).
38. J. Z. Lou et al., "LUVOIR primary mirror segment alignment control with joint laser metrology and segment edge sensing," *Proc. SPIE* **10698**, 1069840 (2018).
39. R. Thompson et al., "A flight-like optical reference cavity for grace follow-on laser frequency stabilization," in *Joint Conf. IEEE Int. Freq. Control and the Eur. Freq. and Time Forum (FCS) Proc.*, pp. 1–3 (2011).
40. K. Abich et al., "In-orbit performance of the grace follow-on laser ranging interferometer," *Phys. Rev. Lett.* **123**, 031101 (2019).
41. J. Sanjuan et al., "Long-term stable optical cavity for special relativity tests in space," *Opt. Express* **27**, 36206–36220 (2019).
42. M. Armano et al., "The LISA pathfinder mission," *J. Phys.: Conf. Ser.* **610**, 012005 (2015).
43. F. Zhao, "Picometer laser metrology for the space interferometry mission (SIM)," in *Conf. Lasers and Electro-Opt.*, Optical Society of America, p. CTuO5 (2004).
44. D. Redding et al., "Wavefront sensing and control for large space optics," *IEEE Aerosp. Conf. Proc.* **4**, 1729–1744 (2003).
45. P. A. Lightsey et al., "James Webb Space Telescope: large deployable cryogenic telescope in space," *Opt. Eng.* **51**(1), 011003 (2012).
46. A. R. Contos et al., "Verification of the James Webb Space Telescope (JWST) wavefront sensing and control system," *Proc. SPIE* **7010**, 70100S (2008).
47. D. S. Acton and J. S. Knight, "Multi-field alignment of the James Webb Space Telescope," *Proc. SPIE* **8442**, 84423C (2012).
48. F. Shi et al., "Experimental verification of dispersed fringe sensing as a segment phasing technique using the Keck telescope," *Appl. Opt.* **43**, 4474–4481 (2004).
49. S. Bikkannavar et al., "Phase retrieval methods for wavefront sensing," *Proc. SPIE* **7739**, 77392X (2010).
50. L. Dewell et al., "System level segmented telescope design (SLSTD) final report," http://www.astrostrategictech.us
51. L. Coyle et al., "Ultra-stable telescope research and analysis (ULTRA) program," http://www.astrostrategictech.us.
52. Gaia Collaboration et al., "The Gaia mission," *Astron. Astrophys.* **595**, A1 (2016).
53. M. Armano et al., "LISA pathfinder micronewton cold gas thrusters: in-flight characterization," *Phys. Rev. D* **99**, 122003 (2019).
54. Busek Company Inc., "20-mN variable specific impulse (ISP) colloid thruster," 2016, https://ntrs.nasa.gov/citations/20160005350.
55. H. P. Stahl, T. Henrichs, and C. Dollinger, "Parametric cost models for space telescopes," *Proc. SPIE* **10565**, 1056507 (2017).
56. A. C. Tribble et al., "Contamination control engineering design guidelines for the aerospace community," *Proc. SPIE* **2864**, 4–15 (1996).
57. J. L. Tveekrem et al., "Contamination-induced degradation of optics exposed to the Hubble Space Telescope interior," *Proc. SPIE* **2864**, 246–257 (1996).
58. M. A. Quijada et al., "Post-flight reflectance of COSTAR and WF/PC 2 pickoff mirrors upon their return from space," *Proc. SPIE* **7739**, 77392J (2010).
59. M. G. Martin et al., "Novel contamination control model development and application to the psyche asteroid mission," in *IEEE Aerosp. Conf.*, pp. 1–9 (2020).
60. J. Garrett, "Outgassing measurements on RTV S691 silicone adhesive," Test report prepared for JAMSS America by OSI (2006).

61. S. B. Shaklan et al., "Error budgets for the Exoplanet Starshade (Exo-S) probe-class mission study," *Proc. SPIE* **9605**, 96050Z (2015).
62. S. R. Martin et al., "Starshade optical edge modeling, requirements, and laboratory tests," *Proc. SPIE* **8864**, 88641A (2013).
63. D. McKeithen et al., "Modeling the scatter of sunlight from starshade edges," *Proc. SPIE* **11117**, 111171L (2019).
64. G. D. Durgin, "The practical behavior of various edge-diffraction formulas," *IEEE Antennas Propag. Mag.* **51**, 24–35 (2009).
65. D. McKeithen et al., "Antireflection coatings on starshade optical edges for solar glint suppression," *J. Astron. Telesc. Instrum. Syst.* **7**(2), 021208 (2021).
66. M. E. Hossain Bhuiyan, D. Semer, and B. P. Trease, "Parametric studies of geometric design factors on static and dynamic loading of an origami flasher," in *Proc. ASME 2017 Conf. Smart Mater., Adapt. Struct. and Intell. Syst.*, Vol. 1 (2017).
67. W. Cash, "Detection of Earth-like planets around nearby stars using a petal-shaped occulter," *Nature* **442**, 51–53 (2006).
68. M. Bottom et al., "Starshade formation flying I: optical sensing," *J. Astron. Telesc. Instrum. Syst.* **6**(1), 015003 (2020).
69. M. Bottom et al., "Precise starshade stationkeeping and pointing with a Zernike wavefront sensor," *Proc. SPIE* **10400**, 104001B (2017).
70. T. L. B. Flinois et al., "Starshade formation flying II: formation control," *J. Astron. Telesc. Instrum. Syst.* **6**(2), 029001 (2020).
71. D. P. Scharf et al., "Precision formation flying at megameter separations for exoplanet characterization," *Acta Astronaut.* **123**, 420–434 (2016).
72. G. J. Soto, D. Savransky, and R. Morgan, "Analytical model for starshade formation flying with applications to exoplanet direct imaging observation scheduling," *J. Astron. Telesc. Instrum. Syst.* **7**(2), 021209 (2021).
73. F. Shi et al., "WFIRST low order wavefront sensing and control (LOWFS/C) performance on line-of-sight disturbances from multiple reaction wheels," *Proc. SPIE* **11117**, 111170I (2019).
74. S. R. Martin and T. L. B. Flinois, "Simultaneous sensing of telescope pointing and starshade position," *J. Astron. Telesc. Instrum. Syst.* **8**(1), 014010 (2022).
75. J. Mather et al., "Orbiting starshade: observing exoplanets at visible wavelengths with GMT, TMT, and ELT," *Bull. Am. Astron. Soc.* **51**, 48 (2019).
76. D. Savransky and EXOSIMS Team, "Exoplanet open-source imaging mission simulator," (2020).
77. D. Savransky, N. J. Kasdin, and E. Cady, "Analyzing the designs of planet finding missions," *Publ. Astron. Soc. Pac.* **122**, 401–419 (2010).
78. D. Savransky and D. Garrett, "WFIRST-AFTA coronagraph science yield modeling with EXOSIMS," *J. Astron. Telesc. Instrum. Syst.* **2**(1), 011006 (2015).
79. G. Soto et al., "Parameterizing the search space of starshade fuel costs for optimal observation schedules," *J. Guidance Control Dyn.* **42**, 1–6 (2019).
80. R. M. Morgan et al., "Faster exo-Earth yield for HabEx and LUVOIR via extreme precision radial velocity prior knowledge," *J. Astron. Telesc. Instrum. Syst.* **7**(2), 021220 (2021).
81. R. Morgan et al., "The standard definitions and evaluation team final report: a common comparison of exoplanet yield," 2019, https://exoplanets.nasa.gov/system/internal_resources/details/original/1434_Standards_Team_Final_Report_20191007.pdf.
82. C. C. Stark et al., "ExoEarth yield landscape for future direct imaging space telescopes," *J. Astron. Telesc. Instrum. Syst.* **5**, 024009 (2019).
83. T. L. B. Flinois et al., "Efficient starshade retargeting architecture using chemical propulsion," *J. Astron. Telesc. Instrum. Syst.* **7**(2), 011206 (2021).
84. B. A. Boom et al., "Nano-G accelerometer using geometric anti-springs," in *IEEE 30th Int. Conf. Micro Electro Mech. Syst. (MEMS)*, pp. 33–36 (2017).
85. C. Krystalle, "Lithium fluoride," 2020, https://www.crystran.co.uk/optical-materials/lithium-fluoride-lif.
86. O. H. W. Siegmund et al., "Microchannel plate detector technology potential for LUVOIR and HabEx," *Proc. SPIE* **10397**, 1039711 (2017).

87. M. J. Li et al., "Successful demonstration of an electrostatically actuated microshutter system for space telescope flight missions," *J. Microelectromech. Syst.* **29**, 1079–1082 (2020).
88. S. E. Kendrick et al., "Multiplexing in astrophysics with a UV multi-object spectrometer on CETUS, a probe-class mission study," *Proc. SPIE* **10401**, 1040111 (2017).
89. M. J. Li et al., "James Webb Space Telescope microshutter arrays and beyond," *J. Micro/Nanolithogr. MEMS MOEMS* **16**(2), 025501 (2017).
90. STSCI, *WFC3 Instrument Handbook*, 2019, https://hst-docs.stsci.edu/display/WFC3IHB.
91. J. Zhang and M. Bottom, "Direct detection and characterization of exoplanets using imaging Fourier transform spectroscopy," in preparation (2021).
92. J. Jewell et al., "Optimization of coronagraph design for segmented aperture telescopes," *Proc. SPIE* **10400**, 104000H (2017).
93. G. Ruane et al., "Vortex coronagraphs for the Habitable Exoplanet Imaging Mission concept: theoretical performance and telescope requirements," *J. Astron. Telesc. Instrum. Syst.* **4**(1), 015004 (2018).
94. J. Krist et al., "Numerical modeling of the Habex coronagraph," *Proc. SPIE* **11117**, 1111705 (2019).
95. O. Guyon et al., "High-precision astrometry with a diffractive pupil telescope," *Astrophys. J. Suppl. Ser.* **200**, 11 (2012).
96. O. Guyon et al., "Single aperture imaging astrometry with a diffracting pupil: application to exoplanet mass measurement with a small coronagraphic space telescope," *Proc. SPIE* **7731**, 77312C (2010).
97. E. A. Bendek, S. Martin, and O. Guyon, "Astrometry exoplanet detection using the Habex Workhorse camera," *Proc. SPIE* **11823**, 1182317 (2021).
98. D. Echeverri et al., "Detecting and characterizing close-in exoplanets with vortex fiber nulling," *Proc. SPIE* **11446**, 1144619 (2020).
99. P. R. Lawson et al., "Terrestrial planet finder interferometer science working group report," 2007, https://exoplanets.nasa.gov/files/exep/TPFIswgReport2007.pdf.
100. C. Cockell et al., "Darwin—an experimental astronomy mission to search for extrasolar planets," *Exp. Astron.* **23**, 435–461 (2009).
101. D. Echeverri et al., "The vortex fiber nulling mode of the Keck Planet Imager and Characterizer (KPIC)," *Proc. SPIE* **11117**, 111170V (2019).
102. G. Ruane et al., "Vortex fiber nulling for exoplanet observations: conceptual design, theoretical performance, and initial scientific yield predictions," *Proc. SPIE* **11117**, 1111716 (2019).
103. G. Ruane et al., "Efficient spectroscopy of exoplanets at small angular separations with vortex fiber nulling," *Astrophys. J.* **867**, 143 (2018).
104. E. Serabyn, B. Mennesson, and S. Martin, "Observing inside the coronagraphic regime with nulling interferometry," *Proc. SPIE* **11446**, 114461K (2020).
105. E. Serabyn et al., "Nulling at short wavelengths: theoretical performance constraints and a demonstration of faint companion detection inside the diffraction limit with a rotating-baseline interferometer," *Mon. Not. R. Astron. Soc.* **489**, 1291–1303 (2019).
106. S. Martin et al., "Achromatic broadband nulling using a phase grating," *Optica* **4**, 110–113 (2017).
107. J. E. Krist, B. Nemati, and B. P. Mennesson, "Numerical modeling of the proposed WFIRST-AFTA coronagraphs and their predicted performances," *J. Astron. Telesc. Instrum. Syst.* **2**(1), 011003 (2015).
108. J. Krist, "Evaluating coronagraph performance with end-to-end numerical modeling: WFIRST and beyond," 2016, https://exoplanets.nasa.gov/exep/files/exep/krist_end2end_modeling.pdf.
109. J. B. Jewell, Jet Propulsion Laboratory, private communication (2020).
110. R. Morgan et al., "Technology maturity update for the Habitable-zone Exoplanet Imaging Observatory (HabEx) concept," *Proc. SPIE* **11115**, 111150N (2019).
111. R. Belikov et al., "Exoplanet occurence rates and distributions—closeout," 2016, https://exoplanets.nasa.gov/system/presentations/files/67_Belikov_SAG13_ExoPAG16_draft_v4.pdf.

112. S. D. Dulz et al., "Joint radial velocity and direct imaging planet yield calculations. I. self-consistent planet populations," *Astrophys. J.* **893**, 122 (2020).
113. R. K. Kopparapu et al., "Habitable zones around main-sequence stars: new estimates," *Astrophys. J.* **765**, 131 (2013).
114. D. Sirbu et al., "Demonstration of multi-star wavefront control for WFIRST, Habex, and LUVOIR," *Proc. SPIE* **11117**, 1111719 (2019).
115. C. Leinert et al., "The 1997 reference of diffuse night sky brightness," *Astron. Astrophys. Suppl. Ser.* **127**(1), 1–99 (1998).
116. S. Ertel et al., "The HOSTS survey—exozodiacal dust measurements for 30 stars," *Astron. J.* **155**, 194 (2018).
117. M. C. Turnbull, "Exocat-1: the nearby stellar systems catalog for exoplanet imaging missions," arXiv:1510.01731 (2015).
118. NASA Exoplanet Science Institute, "Mission + stars table of the NASA exoplanet archive," 2020, https://exoplanetarchive.ipac.caltech.edu/docs/data.html.
119. E. Mamajek, "A modern mean dwarf stellar color and effective temperature sequence," 2019, http://www.pas.rochester.edu/~emamajek/EEM_dwarf_UBVIJHK_colors_Teff.txt.
120. O. Guyon et al., "How ELTs will acquire the first spectra of rocky habitable planets," *Proc. SPIE* **8447**, 84471X (2012).
121. R. Goullioud et al., "The SIM Lite Astrometric Observatory: engineering risk reduction activity," *Proc. SPIE* **7734**, 77341M (2010).
122. J. C. Marr, IV, M. Shao, and R. Goullioud, "SIM Lite Astrometric Observatory progress report," *Proc. SPIE* **7734**, 77340H (2010).
123. E. Bendek et al., "Status of NASA's stellar astrometry testbeds for exoplanet detection: science and technology overview," *Proc. SPIE* **11443**, 114433V (2021).
124. J. Crass et al., "Extreme precision radial velocity working group final report," (2021).
125. National Academies of Sciences, *Engineering, and Medicine, Exoplanet Science Strategy*, The National Academies Press, Washington, DC (2018).
126. P. Plavchan et al., "Earthfinder probe mission concept study: characterizing nearby stellar exoplanet systems with earth-mass analogs for future direct imaging," arXiv:2006.13428v1 (2020).
127. R. K. Kopparapu et al., "Exoplanet classification and yield estimates for direct imaging missions," *Astrophys. J.* **856**(2), 122 (2018).
128. D. Mawet, private communication (2021).
129. D. Redding, "Advances in telescope technology: mirror alternatives for the far IR," 2015, http://conference.ipac.caltech.edu/firsurveyor/page/agenda.
130. D. A. Sheikh, "Low-stress silicon cladding made by pulsed-ion-assisted evaporation," *Proc. SPIE* **9574**, 95740C (2015).
131. Northrop-Grumman, "Ceraform silicon carbide," 2016, https://www.northropgrumman.com/wpcontent/uploads/CERAFORM_SiC_DataSheet.pdf.

Stefan Martin received his BSc degree in physics from the University of Bristol, UK, and his PhD in engineering from the University of Wales. He is formerly a senior optical engineer at the Jet Propulsion Laboratory (JPL), California Institute of Technology, Pasadena, California, USA. At the JPL, he was a leader of the TPF-I Flight Instrument Engineering Team, testbed lead for the TPF-I Planet Detection Testbed, and optical engineer for the Exo-S Starshade study. In addition to stray light and formation flying systems studies for starshades, he developed methods for implementing starshades on space telescopes, such as NGRST. Most recently, he was payload lead for the HabEx telescope design study and then lead optical engineer for ATSA and for the Gomap study.

Charles Lawrence received his PhD in physics from MIT in 1983. He is a research fellow and senior research scientist at the JPL and the directorate scientist for the Astronomy and Physics Directorate. His scientific work has focused on the cosmic microwave background. He was the US project scientist for the ESA Planck Mission and the deputy project scientist for the Spitzer Space Telescope. He is the co-author of more than 250 refereed publications and has NASA

medals for exceptional achievement (2), outstanding leadership (2), and distinguished public service.

David Redding is a research fellow at the JPL and is engaged in active optics technology development. A controls engineer by training, he developed optical modeling tools and practices that have been applied on many space and ground-based projects. He has a special interest in wavefront sensing and control for large telescopes.

Bertrand Mennesson received his PhD in astrophysics and space techniques from Paris Diderot University in 1999, before joining JPL in 2001. His expertise is in the design, assembly, and scientific exploitation of high-contrast high-resolution optical systems—coronagraphs, interferometers, and starshades—used for astronomical imaging. His main scientific focus is on the direct detection and spectroscopy of exoplanetary systems, ultimately leading to the search for life on Earth-like exoplanets, through the use of new instruments and data reduction techniques. He is the author or co-author of 300 publications in specialized journals and at professional conferences.

Michael Rodgers received his PhD in optical sciences from the University of Arizona in 1984 under the direction of Prof. Robert Shannon. He has been an optical designer at Synopsys Inc., and previously Optical Research Associates, for more than 37 years. His optical design and tolerancing work has led to numerous fabricated designs for applications ranging from high-volume consumer and medical products, to single units for specialized research and development applications.

Kevin Hurd is an aerospace design engineer, formerly at JPL, now at Virgin Galactic, with experience in system designs, composite structures, mechanisms, propulsion, thermal solution, on-orbit servicing, and optics.

Rhonda Morgan received her BS degree in electrical engineering from Caltech and her MS and PhD degrees in optical sciences from the University of Arizona. He is the associate technologist for astronomy and physics at the JPL. Her interests include exoplanets, high-contrast imaging, and advanced technologies for space telescopes. She is the lead of the Exoplanet Program Office Standard Science Evaluation Team.

Renyu Hu received his PhD in planetary science from Massachusetts Institute of Technology in 2013. He is a scientist at the JPL and his research strives to identify and characterize habitable environments in the solar system and beyond. He is the starshade scientist of the NASA Exoplanet Exploration Program, providing science leadership to the S5 Starshade Technology Development Activity.

John Steeves received his PhD in aerospace engineering from Caltech and is currently an optomechanical engineer at Amazon's Project Kuiper. Previously, he was an optical engineer in the Advanced Deployable Structures Group at the JPL. His research interests include active mirrors, wavefront sensing techniques, and optical system modeling for space-based instrumentation.

Jeffrey Jewell is a researcher at the JPL, with research interests including cosmology, algorithm development for Bayesian analysis, exoplanets, and technology development for future space-based segmented-aperture telescopes. His current research is focused on the development of advanced wavefront sensing and closed loop control for segmented aperture telescopes, metasurface optics, and the application of photonics to astrophysics instrument concepts.

Charles Phillips received his BS degree in mechanical engineering from Rensselaer Polytechnic Institute and his MS degree in astronautics from the University of Southern California. He is the technical group supervisor of the Advanced Thermal Concepts and Analysis Group at the NASA JPL. He was involved in the thermal design of the Mars Exploration Rovers and has managed thermal teams for the Orbiting Carbon Observatory-2 as well as the Gravity Recovery and Interior Laboratory missions.

Thibault Flinois received his bachelor's and master's degrees in aerospace engineering from the University of Cambridge and his PhD in aeronautics from the Imperial College London. He is the guidance, navigation, and control (GNC) lead at E-Space. Previously, he worked on both technology and flight projects as a GNC engineer at NASA's JPL and at ESA's ESTEC, with a focus on formation flying, telescope pointing, Mars entry, descent, and landing.

Biographies of the other authors are not available.